University of Alberta

Triggering on Single Top Events at the DØ Experiment

by

Kevin Chan 

A thesis submitted to the Faculty of Graduate Studies and Research in partial fulfillment of the requirements for the degree of **Master of Science**.

Department of Physics

Edmonton, Alberta
Fall 2007

Your file Votre référence
ISBN: 978-0-494-33212-2
Our file Notre référence
ISBN: 978-0-494-33212-2

To everyone who had to put up with me directly:
My parents, Elaine and Gary. My sister, Michelle.
Dr. Roger Moore for, well everything.
Andie Bardeck, and Tanya Whyte for managing to put up with me more than most.
Jeff de Jong, and Logan Sibley for putting up with me at work.
All of my friends, especially Gruvis.
I love you all.

Abstract

Data collected by the DØ detector using the online trigger list from version 8 to version 14, was used to calculate a combination of triggers useful in top-quark searches. The single electron and electron + jets triggers were then folded into Monte-Carlo created single-top signal events to create a logical OR of the triggers. These were then compared to the original pre-combination triggers to determine the increase in efficiency.

Contents

Introduction

The top quark was discovered by two collaborations at the Fermi National Accelerator Laboratory in 1995 at a high energy $p\bar{p}$ collider known as the Tevatron by two experiments: CDF and DØ. This discovery involved searching for a top quark pair that was produced in the collisions. The top quark can be produced singly, as well as in pairs. The production of a single top-quark is essential to understanding the properties of the quark since it is the only quark known to decay without undergoing a process known as hadronization. Through the decay of the top quark, properties such as the helicity of the top quark can be studied. Towards an understanding of the top quark, an overview of the Standard Model of particle physics will be given, concentrating on the characteristics of the top quark and its decay properties (Chapter 1).

The Tevatron, where the two experiments reside, had been operational for a number of years before the discovery of the top quark. This $p\bar{p}$ accelerator was completed in 1983 with a centre of mass energy of 1.8 TeV (terra electron volt) and with a typical luminosity of 2.0×10^{30} $\mathrm{cm}^{-2}\mathrm{s}^{-1}$. An upgrade to the accelerator was completed in 1998 with an increase in the centre of mass energy to 1.96 TeV and a significant increase to the typical luminosity of 5×10^{32} $\mathrm{cm}^{-2}\mathrm{s}^{-1}$. Two particle detectors were commissioned at the Tevatron, the CDF detector and the DØ detector, which began to collect analysis quality data in 1988. Both detectors were upgraded to account for the increased rate of collisions supplied by the Tevatron [1]. The DØ detector is the focus of this thesis and so it will be discussed in depth (Chapter 2), concentrating on the trigger systems.

The DØ detector is composed of tracking systems, calorimetry systems and a

muon detection system. The response of the detector to particles in a collision is first passed through a filter known as the trigger system. Since keeping the data from every collision event would be technologically prohibitive, a three tiered trigger system was developed, which keeps only the interesting events as defined by the physics being studied by the DØ experiment. An example of a simple trigger would be one that required an electron in an event to have energy above 20 GeV. An event is only kept if it passes all three trigger levels. An efficiency is associated with every trigger, which indicates how well the trigger is accepting the events of interest. Understanding this efficiency is necessary to understanding the uncertainties in the results obtained from the data. The *caf_trigger* package is a trigger efficiency tool created for the purpose of studying the efficiency of triggers used in the detector (Chapter 3). *caf_trigger* allows for the study of these triggers by using data events that have passed or failed an online trigger, which have been derived from unbiased data. It then folds these efficiencies into offline simulated events (Monte-Carlo) to give a final trigger weight, which is the probability that an event has or has not passed a given trigger.

Since the single top event occurs at a very low frequency when compared to the background events, determining the significance of this event signature requires a very thorough understanding of the triggers used in the selection of events. There is also an ever present need to increase the efficiency of the triggers in use by the single top group, which are the single electron triggers and the electron + jets triggers. The logical ORs of the single electron triggers and the logical ORs of the electron + jets triggers were produced. The *caf_trigger* package was then used to study the combination, through logical ORs of these triggers as a possible improvement of the triggers that have been used to collect the data (Chapter 4). The goal of this study was to judge whether there was a significant gain in the efficiency of the trigger combination (single electron triggers, OR'd) OR'd with (electron + jets triggers, OR'd).

Chapter 1

Theory

1.1 The Standard Model

Our current theory of particle physics began its developement in Einstein's theory of the photoelectric effect in 1905, which gave the first insights into wave-particle duality. This was further developed by de Broglie in 1923 [2] to extend the wave-particle duality from photons and electrons to all particles. During the 1930s, H. Yukawa proposed the meson as the mediator of the strong force, W. Pauli proposed the existence of the neutrino leading to the theory of the weak force and Carl Anderson found evidence of the anti-electron (positron). During this time, many physicists were laying the foundation of the mechanics of these quantum particles, named for the quantized nature of their states. Many particles were found over the course of the years with the strangest being the aptly named "strange" particle, discovered by G. D. Rochester and C. C. Butler with its "strange" quantum number. These particles could be grouped together, in terms of conserved charge and strangeness, and had properties which bewildered the scientists of the day. The bewildering properties, such as charged particle tracks having a kink in them, could not be explained at the time since the foundations of quark theory had not been set. The baryons and mesons, with their charge and strange quantum numbers, were then organized into geometric groupings called the Eightfold Way by Murray Gell-Mann in 1961 [3]. This lead to the idea of quarks by Gell-Mann in 1964 as the elementary constituents of the baryons (particles with a half-integer spin) and mesons (particles with an integer spin). This grouped the elementary particles into

leptons (like the electron and the neutrino), and quarks (which made up the baryons and mesons). Over the years, more particles were found like the mediators of the weak force (the intermediate vector bosons), and a few more quantum numbers were added such as quark colour. These would lead up to what is now known as the Standard Model (SM).

The Standard Model is the current theory, which describes 3 of the 4 fundamental forces of nature. It describes the strong, electromagnetic and weak forces but does not currently provide a description of gravity. In the Standard Model, the elementary particles can be divided into two groups: fermions and bosons. Fermions and bosons are delineated by their intrinsic angular momentum known as their spin. The fermions have half-integer spin while the bosons have integer spin, and composites of these fundamental particles may also be delineated by their total spin state as fermions or bosons. Quarks and leptons are both fermions, while the mediators of the strong, weak and electromagnetic force are spin 1 vector bosons. These fundamental forces are carried by the gluon (strong), the W and Z bosons (weak) and the photon (electromagnetic). In the Standard Model, there is also another fundamental boson, which is not a mediator of a force, and that is the Higgs boson [4]. The Higgs has not been observed in experiments but it is thought to be key in explaining the origin of masses and the differences in the masses of the mediator bosons, quarks, and leptons. Fermions themselves are divided into three generations (Table 1.1), where ordinary matter consists of the stable first generation fermions. As the generation increases, so does the mass, although it is unknown at this time whether the neutrinos follow the same ordering of mass. The first generation particles are stable whereas the second and third generation particles will decay to second or first generation particles. The stability of the first generation particles is assumed to be true since they are the lightest particles of their type and cannot decay into anything lighter. As can be seen in the table, the leptons and quarks have integral and fractional charge, respectively.

The quarks are also associated with a colour quantum number which denotes 3

Table 1.1: The Elementary Fermions and their categories. Charge conjugate states are not included in the table.

	Generations			
	I	II	III	Charge
Leptons	ν_e	ν_μ	ν_τ	0
	e^-	μ^-	τ^-	-1
Quarks	d	s	b	-1/3
	u	c	t	2/3

general charges: red, green and blue. The colour charge is only carried by quarks and gluons, the strong force mediator. Quarks can carry 1 of the 3 colour charges, while anti-quarks carry 1 of the 3 anti-colour charges. Gluons carry the colour force between quarks and are made of a colour charge and an anti-colour charge. The "physical" gluons are a linear combination of these 9 possible gluon states, which lead to an octet of gluons, excluding the colour neutral combinations of red/anti-red, green/anti-green and blue/anti-blue. This is what makes quarks and the strong force different from the electromagnetic force. Whereas two oppositely charged particles will see a field of virtual dipoles, which screen the charges at larger distances, two colour charges will see a field of colour dipoles. Some of these virtual colour dipoles will screen the colour charges from each other. The advent of 3 colour charges, with their respective anti-colour charges, means that the majority of the virtual colour charges will not screen the overall charge but make it stronger. This means that the force that is felt between two colour charges does not diminish with distance as with the electromagnetic force. When the colour charges are moved close enough, they feel negligible amounts of force and this reversal of the force characteristic from the electromagnetic force is called asymptotic freedom. It is more energetically favourable for a pair of colour charges to be produced from the vacuum energy than it is to separate the two charges. This is part of a theory known as colour confinement, which states that the colour carrying quarks must form pair (mesons) or triplet (baryons) states which are colour neutral. The gluons, unlike photons of the electromagnetic force, can also interact with each other through their colour

charges.

The forces are associated with a coupling constant, which denotes the strength of the force in coupling particles. The coupling constants are not actually constant with energy and "run" as energies change. The differences between the electromagnetic force and the strong force is shown in the running of the coupling constants; the electromagnetic coupling will increase with energy, while the strong coupling will decrease with energy.

The neutrinos, ν_e, ν_μ, and ν_τ, have no electric or colour charge and were thought to be massless until recently. The electron neutrino was seen to change its flavour as it propagates from the core of the sun to the Sudbury Neutrino Observatory, which can be explained by neutrino oscillations [5]. This requires a mass difference between the different neutrino generations, which indicates that the neutrinos are not massless as defined in the Standard Model. These oscillations occur because the mass eigenstates of the neutrinos are not the same as their flavour eigenstates. Other experiments, such as Super-Kamiokande, for atmospheric neutrinos, showed that neutrino oscillations occured from many other sources.

Since the neutrinos lack electric or colour charge, they are able to pass through most matter without interacting. This poses a challenge for reconstruction of an event with neutrinos since their path can neither be tracked, nor their energy determined. In top quark events, with the decay of a W-boson from the decay of the top, the neutrino can carry away a significant amount of the energy in the event. In practice, the vector sum of the neutrinos momentum, represented by an imbalance in the total transverse energy in the event, is known as the missing transverse energy ($\not\!\!E_T$). The transverse component of the energy is used due to physical restrictions on where detection equipment can be placed because no detector can be put into the beam pipe. The massive leptons and quarks both have anti-particle counterparts, which can be viewed as the negative energy solutions to the Dirac equation [6]. These particles with negative energy can be interpreted as anti-particles travelling backwards in time. The anti-quarks exist in anti-baryons and mesons. As an

example, the anti-proton is a baryon formed from the combination of $(\bar{u}\bar{u}\bar{d})$ valence quarks while the J/ψ is a combination of $(c\bar{c})$.

The forces in the SM are mediated by an exchange of a virtual particle: vector bosons. In Quantum Electro-Dynamics (QED), the mediator for the electromagnetic force is the photon, which couples to charged particles. Most particle interaction processes can be reduced to an elementary primitive vertex, which represents the lowest order perturbation approximation. A primitive vertex is simply the interaction between the fewest possible particles, and the mediator of the interaction. This forms a vertex that can be glued together with other primitive vertices to form more complex interactions. This does not include 4 particle vertices such as 4 Higgs particle interactions. These can be represented pictorially by a Feynman diagram, which is a visual tool used in perturbative calculations in Quantum Field Theory (QFT). The leading order diagram consists of the fewest number of vertices required for the interaction. As an example, an electron and a positron colliding, creating a photon, would be represented by a single vertex with three "legs". An example higher order correction to the perturbative calculation can be represented by including an electron positron loop in the leg of the photon, adding 2 more vertices to the diagram.

The electromagnetic primitive vertex is shown in Figure 1.1a, where l is a chaged lepton and γ is the photon. In Quantum Chromodynamics (QCD), the mediator for the strong force is the gluon, which couples to coloured particles, much as the photon couples to charged particles. In this case, since only quarks and gluons carry colour, the primitive vertex is shown in Figure 1.1b, where q is a quark and g is a gluon. Gluons can also couple to other gluons in a vertex with 3 or more legs. In weak interactions, the mediators for the weak force are the charged W's and the neutral Z's, which participate in charged and neutral current weak interactions respectively. The fundamental weak, charged, primitive vertex is shown in Figure 1.2a, where l is a charged lepton, ν_l is a neutrino and W is our charged boson. Similarly, the neutral primitive vertex uses the Z as a mediator and is shown in

Figure 1.2b, where the particles ν_l can also be leptons or quarks as the Z couples to both.

The weak force also interacts with quarks but does not conserve the flavour of the quarks in Table 1.1. Instead, it couples the known quarks in what is know as the Cabibbo-Kobayashi-Maskawa matrix [7] shown in Figure 1.1. This is a 3×3 matrix, which says that the weak force does not simply couple u-d (up-down), c-s (charm-strange), and t-b (top-bottom quarks). Instead, it couples u-d', c-s', and t-b', where the d', s', and b' quarks are linear combinations of the d, s, and b flavour eigenstates, describing the weak eigenstates as a mixture of strong eigenstates. This mixing of the eigenstates means that the CKM matrix is not equivalent to the identity matrix (Figure 1.2), which would not show d' as a mixture of d, s and b quarks. The values in the CKM matrix account for the cross-generation transitions such as a strange quark decaying to an up quark in the reaction $\Lambda \rightarrow p + \pi^-$. The values of the matrix has an irreducible complex phase, which is used as an indication of the amount of CP violation. CP symmetry is the symmetry of charge conjugation, which converts a particle into its anti-particle, and parity, which mirrors the physical world transforming $x \rightarrow -x$, $y \rightarrow -y$, and $z \rightarrow -z$. A violation of CP is incorporated in the SM through the CKM matrix by the introduction of a complex phase. If there was no complex phase in the quark mixing CKM matrix, then decays incorporating the matrix would be CP invariant. This is because a CP transformation includes taking the complex conjugate of the decay amplitude, which would have the same amplitude if there was no complex phase. The 3×3 unitary matrix is the smallest matrix that incorporates an irreducible complex phase. A unitary matrix is a complex matrix that when multiplied by its complex conjugate is equal to the identity matrix. A 2×2 unitary matrix can be parametrized by 1 angle and 3 complex phases. These complex phases can be removed to give a single overall phase. Since there are no complex phases, a 2×2 unitary matrix cannot incorporate CP violation. This type of CP violation is one of the factors that attribute to the matter/anti-matter imbalance in the universe, although it is not enough to account for it. More CP violation than is shown in the CKM matrix

is required to fully explain the imbalance.

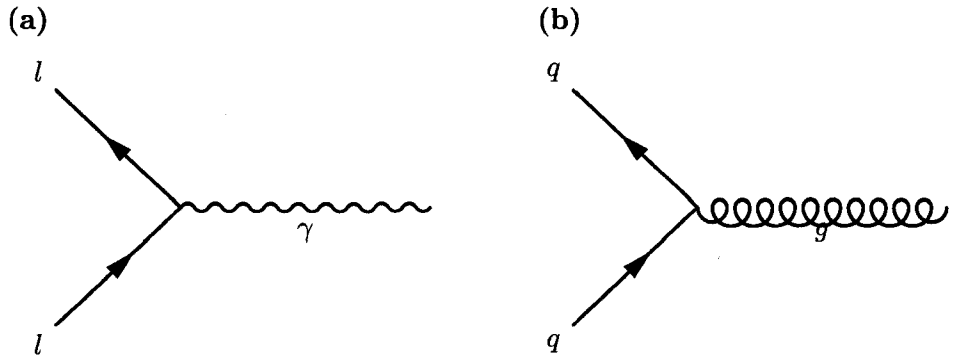

Figure 1.1: Feynman diagrams for the primitive vertex of: (a) the electromagnetic force with propagator γ, and (b) the strong nuclear force with propagator g.

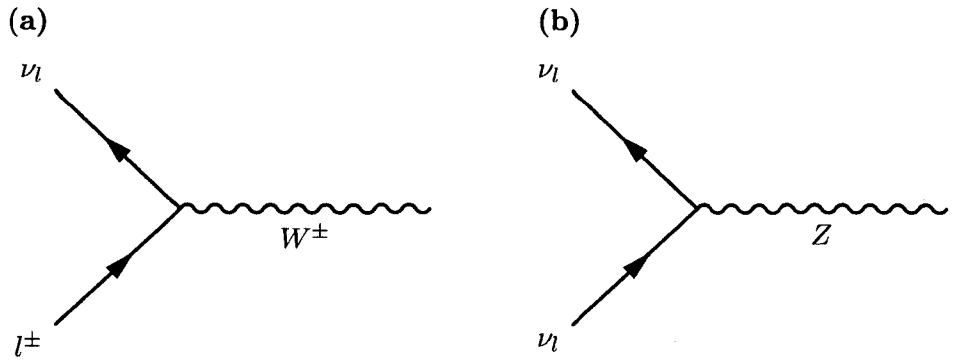

Figure 1.2: Feynman diagrams for the lepton primitive vertex of the weak force with propagator: (a) W boson, and (b) Z boson.

$$\begin{pmatrix} d' \\ s' \\ b' \end{pmatrix} = \begin{pmatrix} V_{ud} & V_{us} & V_{ub} \\ V_{cd} & V_{cs} & V_{cb} \\ V_{td} & V_{ts} & V_{tb} \end{pmatrix} \begin{pmatrix} d \\ s \\ b \end{pmatrix} \tag{1.1}$$

$$\begin{pmatrix} |V_{ud}| & |V_{us}| & |V_{ub}| \\ |V_{cd}| & |V_{cs}| & |V_{cb}| \\ |V_{td}| & |V_{ts}| & |V_{tb}| \end{pmatrix} = \begin{pmatrix} 0.97377 \pm 0.00027 & 0.2257 \pm 0.0021 & 0.00431 \pm 0.00030 \\ 0.230 \pm 0.011 & 0.957 \pm 0.017 & 0.0416 \pm 0.0006 \\ 0.0074 \pm 0.0008 & 0.0406 \pm 0.0027 & > 0.78 \end{pmatrix} \tag{1.2}$$

So far, the Standard Model has successfully agreed with every experimental test put forth, but it needed to be expanded in the form of massive neutrinos. The

neutrino oscillations, however, can be fitted into the Standard Model in the form of a mixing matrix much like the quarks. There is, however, still one predicted particle left unobserved and that is the Higgs boson. The SM Higgs field is a scalar field which has a non-zero expectation value within the vacuum. This vacuum expectation value is thought to be the mechanism through which all elementary particles acquire mass and is important in understanding the breaking of the electroweak gauge symmetry imposed by the Lagrangian (SU(2)×U(1), where SU(2) is the special unitary group of degree 2, U(1) is the unitary group of degree 1, and SU(2)×U(1) is the direct product of these two groups). The force mediators are expected, in the electroweak force, to be massless. A gauge symmetry is a requirement that the Lagrangian be invariant under global transformations and local transformations. This means that the Lagrangian is invariant under a phase transformation performed anywhere in space-time, and that symmetry transformations can be performed in a region of space-time without affecting other regions. This gauge symmetry is thought to be spontaneously broken by the Higgs mechanism at some energy above which the electromagnetic and weak forces are unified. The spontaneity of the symmetry breaking comes from the form of the potential used in the Lagrangian. The potential is equivalent to a 4th power equation (x^4), with a quadratic energy term determining the minima. Such an equation can have a symmetric global minima which distorts into an asymmetric local minima at a certain value of the energy.

The broken gauge symmetry leads to massive weak gauge bosons (W^+, W^-, and Z) and a massless electromagnetic gauge boson (γ, the photon). The electromagnetic gauge boson corresponds to the generator of the gauge group (a group associated with a gauge symmetry) $U(1)_{em}$ which comes from the gauge transformation of the quantum-electrodynamic (QED) Lagrangian that is a phase invariance. This phase invariance defines a rotation group which is defined by U(1), where the *em* label identifies this as the group associated with the QED Lagrangian. The weak gauge bosons are defined by the gauge group $SU(2)_L \times U(1)_Y$. $SU(2)_L$ comes from the weak force favouring left handed interactions defined with a weak iso-spin doublet for the neutrinos and leptons. $U(1)_Y$ comes from the weak hyper-charge Y,

defined as twice the difference of the electric charge and the weak isospin to bring in the electric charge. The weak iso-spin is associated with the spin group SU(2), and $SU(2)_L \times U(1)_Y$ with gauge transformations between the weak gauge bosons W^+ (+1), W_- (-1), Z (0), and the photon γ through linear combinations of the group generators. The Z and γ are formed by mixing of the $U(1)_Y$ group with the two W bosons from the $SU(2)_L$ group. While U(1) is a commutative group, $SU(2) \times U(1)$ is not. This non-commutative property comes from the mixing of quarks and leptons, defined by matrices that do not generally commute.

The measured masses of the W and Z bosons are approximately 80 GeV/c^2 and 91 GeV/c^2 respectively. Although the Higgs itself has not been found, indirect bounds for the mass of the Higgs boson may be found from fits of the theory to electroweak observables such as the masses of the t-quark (top-quark) and the W boson. The measured mass for the top quark was found to be $m_t = 178 \pm 8_{stat} \pm 10_{syst}$ GeV/c^2 for CDF [8] and $m_t = 199 \pm 20_{stat} \pm 22_{syst}$ GeV/c^2 for D0 [9], where the first uncertainty is the statistical uncertainty (from the finite sample size) and the second uncertainty is the systematic uncertainty (from uncertainties in the theory or calculations and the experimental setup such as the acceptance of the detector). The fit for the bounds on the Higgs mass with all the global data is given by the Particle Data Group [16] as $m_H = 89^{+38}_{-28}$ GeV/c^2 with a top mass of $m_t = 172.7 \pm 2.8$ GeV/c^2. The top quark, with the most recent mass measurement of $m_t = 171.4 \pm 1.2_{stat} \pm 1.8_{syst}$ GeV/c^2 [10] from up to 1 fb^{-1} of data, is the most massive quark by far and is theorized to be important in the Higgs mechanism since the Higgs couples to masses. This, along with confirming another cornerstone of the SM, is one of the reasons why the discovery of the top quark has been so important. Further study of the top quark through the production of a single top quark will provide better bounds for the CKM matrix.

1.2 Production of a Single Top Quark

In hadron colliders, such as the Tevatron, the top quark is produced predominantly in pairs through the QCD processes of $q\bar{q} \rightarrow t\bar{t}$ and $gg \rightarrow t\bar{t}$. At the Tevatron energies of 1.96 TeV, and with a mass of $m_t = 175$ GeV/c^2, the pair production cross section is expected to be $6.7 \pm^{0.71}_{0.88}$ pb combined for the s-channel and t-channel [11]. s-channel processes are those that have a time-like mediating particle between the vertices, while t-channel processes have a space-like mediator. Pair production of top quarks acts as an excellent probe into the QCD properties of the top quark such as its cross section (σ) and its mass, but production of a single top quark will allow for a study of its electroweak properties. The single top has 3 production modes of which 2 are dominant at the Tevatron. These can be viewed as 3 different processes with 3 different cross sections at the Tevatron for a mass of $m_t = 175$ GeV: the t-channel Figure 1.3 (2.4 pb), the s-channel 1.4a (0.86 pb) and the tW^- mode of production Figure 1.4b (0.088 pb) [17]. The tW^- mode of production is suppressed at the Tevatron, but has a higher cross section than the s-channel at the LHC, approximately 56 pb and 11 pb respectively. This is far less than the $t\bar{t}$ cross-sections, and with both involving the creation of t-quarks, the $t\bar{t}$ process provides a significant background for single top identification.

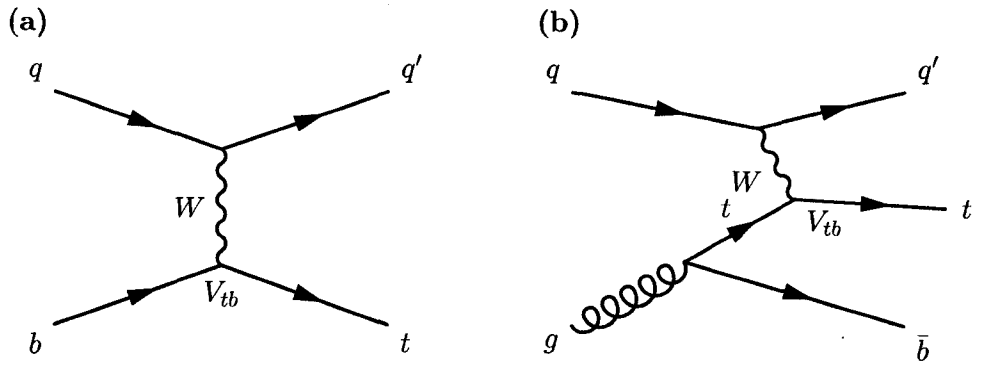

Figure 1.3: Feynman diagrams for the t-channel: (a) leading order diagram with a t and a q' quark produced and (b) an next to leading order (NLO) diagram with a t, a q', and a $\bar{b}$ quark produced.

As can be seen in Figure 1.3 and 1.4, the production of the single top depends

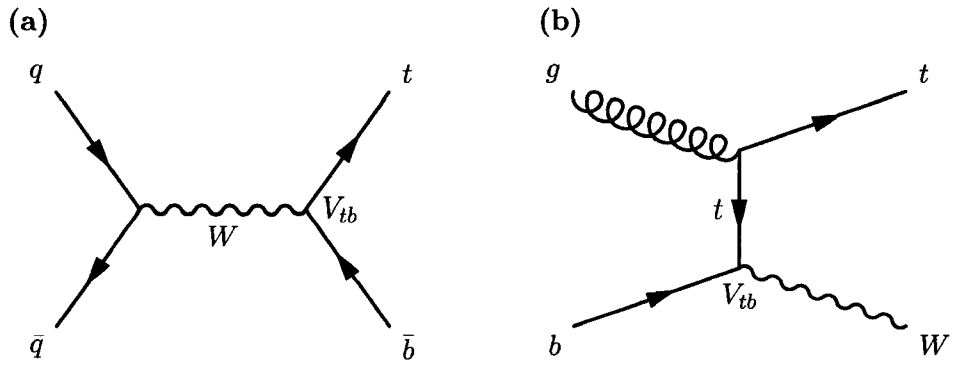

Figure 1.4: Leading order Feynman diagrams for the (a) s-channel and (b) tW^- process for the production of a single top quark.

strongly on the CKM matrix element V_{tb}. The value of $|V_{tb}|^2$ from the CKM matrix can be extracted directly from a measurement of the cross section, neglecting higher order terms, which is also one part of the complex number $V_{tb} \times V_{tb}^*/V_{cb} \times V_{cb}^*$. Since the CKM matrix is unitary, these values constrain a unitary triangle, formed by the values of the matrix. This provides a constraint for the CKM matrix and can hint at new physics which depends on the difference between the measured CKM matrix and how far it is from a unitary matrix. The decays of the B^0 meson also depend on the CKM matrix element V_{tb} [12], and so can provide another measurement of this matrix element.

Due to the lower predicted cross sections for the tW^- mode at the Tevatron, the production is far less likely to be detected when compared with the relatively abundant t-channel and s-channel production. The identification of the single top production is difficult due to the abundant background events that share a similar signature to the signal events; pair production of top quarks is one such background. To understand the background events that make this difficult, we need to discuss the signal signature of the single top.

Quarks are coupled to other quarks at low energies through a process known as confinement. As one quark moves away from another quark, the energy of their binding increases. At high energies, it is energetically favorable for the escaping quark to produce a pair. These quark pairs can further decay in a repeated process,

known as hadronization, until what remains is a cluster of colour-neutral mesons and baryons known as a *jet*. The momentum of the original quark carries the jet into the detector and it is seen in the calorimeters as a cone shaped deposit of energy. The t-quark, however, does not undergo hadronization due to its short decay lifetime of $< 10^{-24}$ s [13]. The dominant decay ($\approx 100\%$) of the t-quark is given by $t \rightarrow Wb$, which is the primary weak vertex for the W boson, and the b and t quarks. The other decays involve a change in the quark generation by converting the t-quark into an s-quark ($t \rightarrow Ws$) or a d-quark ($t \rightarrow Wd$), which have not been observed. The b-quark produced in this decay will undergo hadronization into a jet while the W boson may decay into a lepton (l) and a neutrino (ν_l), preferably an electron or a muon with their associated neutrinos ($e + \nu_e$ and $\mu + \nu_\mu$). The reason we do not prefer tau leptons is because taus are difficult to detect. The taus, due to their short lifetime, will tend to decay into charged particles before they reach the detector. This means that looking for a tau involves identifying a jet with certain characteristics which is more difficult than finding the clean signal of the electrons and the muons. The decay of the b-quark will produce a jet from a vertex that is displaced from the main interaction vertex. The W boson may also decay into a q-$\bar{q}$ pair, but this will not provide a good search signature since the two quarks will hadronize into jets. This will mean that we are looking for a minimum of 4 jets, with 1 or 2 as b-quark jets and certainly not as easy to differentiate from other backgrounds as an event with a high energy lepton.

Now that we have described the decay modes of the t-quark, we can look at the individual channels of production. In the t-channel (Figure 1.3a), a q'-quark and a t-quark is produced as the leading order production, with a similar process with the b-quark provided by a gluon (Figure 1.3b). In the s-channel (Figure 1.4a), a t-quark and a $\bar{b}$ quark are produced. Since the single top is a free quark that decays instead of undergoing hadronization, the spin states of its decay products are more directly determined by the spin state of the t-quark [14]. This can be used to test the left handedness of weak interactions at high centre of mass ($\sqrt{s}$). As well, the s and t-channels are sensitive to different new physics decays such as the flavour

changing neutral current (FCNC) decays of the top quark. These FCNC decays, such as $t \rightarrow q\gamma$, are suppressed in the SM and are not observable in the current particle colliders. The observation of these decays would be an indication of new physics [16].

Chapter 2

The DØ Detector

2.1 An Overview of the Detector

The DØ Detector collected data from 1992-1996, in a period known as Run I, using proton anti-proton collisions at a centre of mass energy of 1.8 TeV [18]. This led to the discovery of the top quark and refined further measurements of Standard Model parameters. The Tevatron was then upgraded and began running again in 2001 where this later period is known as Run II. During Run I, the peak luminosity provided by the Tevatron was typically 1.6×10^{31} $cm^{-2}s^{-1}$ [19]. This was produced by six bunches of protons and anti-protons, in the machine, with a 3.5 μs gap between bunch crossings. During this first run, the DØ detector recorded 140 pb^{-1} of integrated luminosity [19]. After the Tevatron was upgraded with a new Main Injector, the Tevatron operated with 36 bunches of protons and anti-protons with only a 396 ns gap between bunch crossings, and with a centre of mass energy of 1.96 TeV [18].

The DØ Detector was upgraded in order to handle the higher luminosity from the upgraded Tevatron, along with the read-out electronics to handle the data from the increased collision rate. The following is an introduction and broad overview of the detector which will be explored in detail in the later sections of this chapter. The tracking, calorimetry and muon systems will be discussed which will be followed by a discussion of the triggering system. The upgraded DØ detector consists of three detector subsystems surrounding the beam pipe in which the proton anti-proton collisions occur, where the scale of the components can be seen in figure 2.1. The

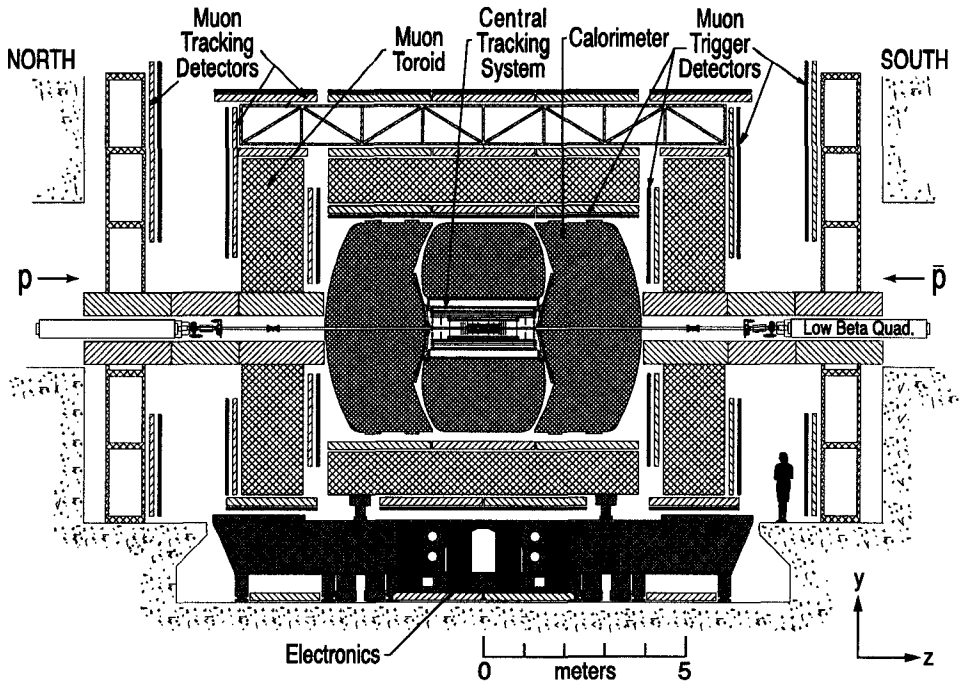

Figure 2.1: The beam pipe, the tracking system, the calorimeters and the muon system [20].

central tracking detectors are closest radially to the beam pipe, consisting of the Silicon Microstrip Tracker (SMT), the Central Fibre Tracker (CFT), a 2 T solenoidal magnet and the preshower detectors. Moving further from the interaction point, the preshower detectors are the uranium/liquid-argon calorimeters which consists of a Central Calorimeter (CC), an End Calorimeter North (ECN), and an End Calorimeter South (ECS). The is then surrounded by the muon detection system, which consists of toroidal magnets, the Central Muon Detector, and the Forward Muon System.

The addition of new detector components for Run II, along with the increased luminosity and the reduction in the bunch spacing required an improvement of the data acquisition system. To this end, the read-out electronics of the detector components have been upgraded. This upgrade includes replacement of the front-end boards with newer electronics capable of a larger bandwidth. The trigger system, a decision making system which decides whether to keep or discard a detected collision event, has also been upgraded to include newer read-out electronics capable of

performing more complex algorithms than before. It is a hardware and software system which emphasizes speed and accuracy in order to handle the significant amount of data coming from the detector. Such a system is required since the 7 MHz rate of collisions would require writing out at a rate and storage capacity that are far beyond the capabilities of the system. The trigger system is still expected to reduce the data rate to 50 Hz before it it written to tape. The trigger consists of three trigger levels; a hardware level (Level 1 or L1), a combination of hardware and software level (Level 2 or L2) and software level (Level 3 or L3) which provides a fast reconstruction of the event and is the slowest of the three. Acceptance of an event at a given level requires acceptance from the lower level triggers. The three distinct levels allow for more complexity in the algorithms used to determine which events should be stored for further analysis and which are unimportant.

In the following subsections, a right handed coordinate system is used: the z-axis is along the proton direction, the y-axis is vertically upwards to the z-axis, the angle ϕ is the azimuthal angle about the z-axis, the angle θ is the polar angle to the z-axis which is represented by the pseudorapidity $\eta = -\ln\tan\theta/2$, and the r coordinate is the perpendicular distance from the z-axis. The pseudorapidity is used instead of θ, and is an approximation of the Lorentz invariant rapidity angle. This rapidity is a hyperbolic angle ($r = \tanh^{-1}\beta$, where $\beta = v/c$, v is the velocity, and c is the speed of light), which due to its Lorentz properties, is an additive quantity unlike velocity in special relativity. The rapidity is calculated using the energy of the particle, whereas the pseudorapidity only depends on the polar angle. This makes it a more suitable variable to use in an environment where energy determination in the forward regions of the detector is less accurate. The pseudorapidity is close to the rapidity in an environment where the particles are boosted close to the speed of light.

2.2 The Tracking System

The Central Fibre Tracker (CFT) and Silicon Microstrip Tracker (SMT) are the tracking detectors which are used to measure the tracks of particles, locate the primary vertex of the collision event from these tracks, and are used to match these tracks to objects in the calorimeter and muon systems. This is accomplished by linking hits in the detector together and projecting them back to the interaction point. The tracking detectors can locate the primary vertex to a resolution of 35 μm in the $r-\phi$ plane [18]. They also provide an accurate measurement of the lepton transverse momentum (p_T), the jet transverse energy (E_T), the missing transverse energy $\not\!\!E_T$, and can tag b-quark jets with an impact parameter resolution of 15 μm [18]. The solenoidal magnet is used to provide a way to measure the momenta of particles, optimize the momentum resolution $\delta p_T/p_T$, and tracking pattern recognition. This is accomplished by the creation of a nearly uniform (see figure 2.2) 2 T magnetic field within the tracking chamber. The trajectories of charged particles will bend in the magnetic field, and the radius of curvature of the track provides a determination of the momentum. The large strength of the magnetic field is required in order to create a noticeable bend in the tracks for an accurate momentum measurement, even at high p_T. The high magnetic field also serves to seperate tracks that would otherwise be resolved as a single track in a lower magnetic field. The fourth component of the tracking system is the preshower detector. The preshower detectors can provide energy sampling and also provide accurate position measurements. This enhances matching between tracks and calorimeter showers, which aid in electron identification during triggering and offline reconstruction. These systems and their physical relationship to the calorimeters are shown in figure 2.3.

The Silicon Microstrip Tracker (SMT), located radially near the beampipe, provides for high resolution vertex and track reconstruction, over nearly the full η range, $|\eta| < 3$. The detection of these charged particle tracks is accomplished by creating a depletion zone, a region without charge carriers, within the silicon. When a charged particle enters the silicon, it ionizes the silicon creating electron/hole pairs,

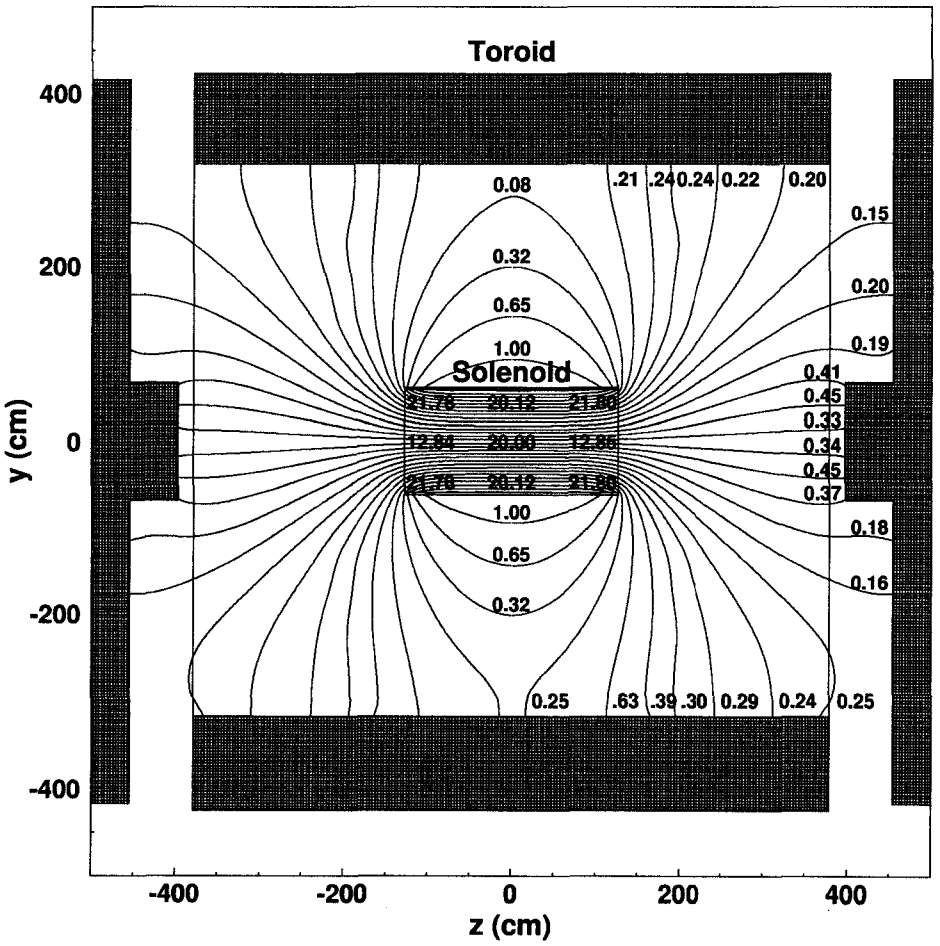

Figure 2.2: y-z view of the magnetic fields for the toroidal and solenoidal magnets in units of kG. The central toroid is approximately 1.8 T while the end toroids are about 1.9 T. The tracking system is only within the central box [20].

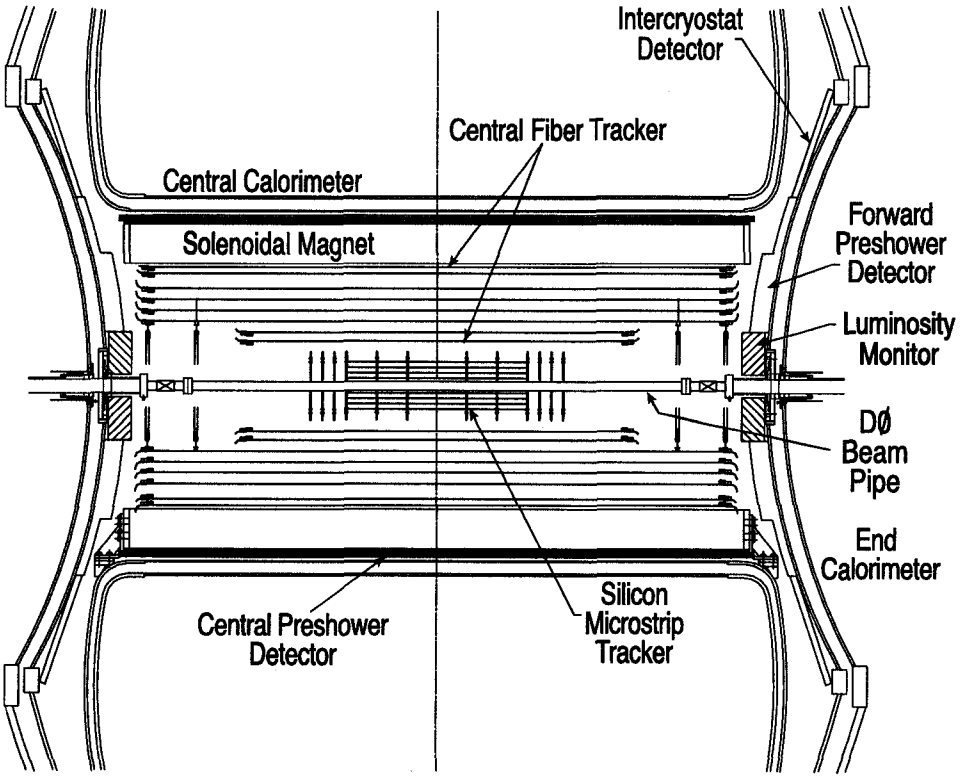

Figure 2.3: The tracking systems which include the Central Fibre Tracker, the Silicon Microstrip Tracker, the Preshower Detectors, and the Solenoidal Magnet [20].

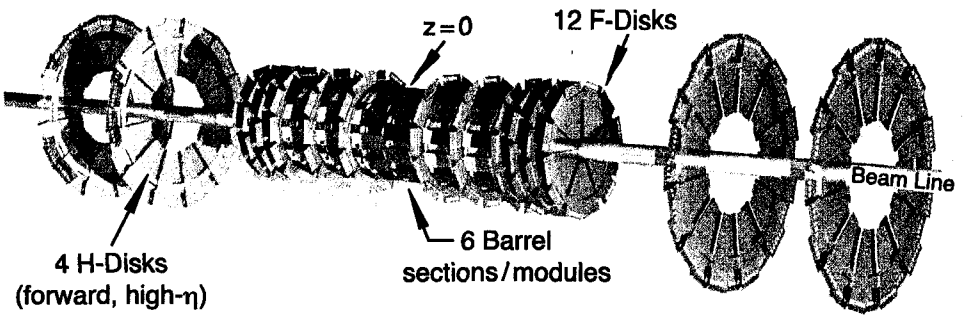

Figure 2.4: The barrel and disk detectors used for the Silicon Microstrip Tracker [20].

which produces a current to a connected electrode. This will provide one or two coordinates for single or double sided silicon wafers, respectively. To maximize the accuracy of this detection, the detector was designed to minimize the number of tracks that hit the detector surfaces at shallow angles for all of η; this required a combination of barrel and disk detectors. In the central region covering $|\eta| < 2$, 6 12 cm long barrels with 4 detector layers each, are used. These measure the $r - \phi$ coordinates. These are further layered by 12 disk detectors, which surround and cap each barrel called F-disks which measure the $r - z$ as well as $r - \phi$. Farther along the beampipe from the center, sit two larger disks on either side of the barrel detectors and F-disks (Figure 2.4). These larger disks are called H-disks and cover the remaining region of $2 < |\eta| < 3$ [18]. The placement of the disks minimize the number of tracks which will hit the surface of the detector at a shallow angle; barrel detectors for tracks of low η and disk assemblies for tracks of high η. The SMT sends the signals it recieves to the Level 2 and Level 3 triggers, so that the information can be used to trigger on displaced vertices from b-quark or other long lifetime decays.

It is required for the SMT to be high resolution, given its proximity to the beampipe, because the particle tracks will have less seperation closer to the interaction point. The CFT is situated radially outward from the SMT and thus farther from the beampipe. This extra distance reduces the need for the higher resolution materials of the SMT. The CFT is constructed of cheaper scintillating fibres, which

have a lower accuracy than the silicon microstrips of the SMT. When a passing charged particle encounters one of these fibres, they emit light with a frequency of 340 nm, which is absorbed by a wave-shifter and re-emitted at 530 nm. This wave-shifted wavelength of light is well transmitted in the polystyrene core of the fibres. This light then travels through clear fibre waveguides and is collected by Visible Light Photon Counters (VLPC). These are impurity-band silicon avalanche photodetectors that sit in a cryostat of liquid helium, and operate with a maximum efficiency at a temperature of 9 K [18]. The VLPCs can detect single photons and work well in high noise environments, sending the electrical signals to the preamplifiers that sit on Analogue Front End boards (AFEs). Since the particle tracks will diverge due to their directions of travel and the magnetic field imposed on them, the scintillating fibres do not need to be as fine grained as the silicon microstrips. The CFT consists of eight concentric support cylinders which hold these fibres. The fibres themselves are 835 μm in diameter and 1.66 or 2.52 m in length, which are formed into layers. Doublet layers are formed by aligning the fibre centers of one layer with the spaces between the fibres on a second layer. Each of the eight support cylinders houses a doublet layer of fibres aligned along the beam axis (axial layers) and at a stereo angle (stereo layers) of u ($+3°$) or v ($-3°$). From the VLPC converted electrical signals sent to the AFEs, the CFT is able to provide a fast and continuous read-out of discriminator signals to the Level 1 trigger system. If Level 1 accepts the event, it sends track information to Level 2 for triggering. Level 3 recieves a slower read-out of the digitized analog signals, in addition to Level 1 and Level 2 information.

Around the tracking detectors are the preshower detectors; the Central PreShower detector (CPS) covering the central region of $|\eta| < 1.3$ and the two Forward PreShower detectors (FPS) covering the end regions of $1.5 < |\eta| < 2.5$, on the faces of the end calorimeters. The preshower detectors provide fast energy and position measurements which can be used at L1 for triggering. In the CPS, these measurements occur before the particles shower. They work much like the CFT in that they use scintillating fibres and VLPCs to provide a read-out. While the CPS works much

like the CFT, the FPS is a little different. In the FPS, charged particles pass through 2 layers: the Minimum Ionizing Particle (MIP) layer and shower layers past the absorber. Charged particles will pass through the MIP layer and register minimum ionizing signals which provide a measure of the location of the track. Electrons will shower (a shower will be defined in the calorimeter section) in the absorber which will be detected in the shower layer and can be matched spatially with a MIP layer signal. Photons may not interact with the MIP layer but will tend to shower in the shower layers past the absorber, and heavier charged particles are less likely to shower at all, producing another MIP signal in the shower layer.

2.3 The Calorimeters

The calorimeters are used to measure the energy of the electrons, photons and jets with or without a magnetic field, as well as provide an indirect measurement of the transverse energy balance in events. They also assist in object identification of the electrons, photons, jets and muons, as well as providing a measurement of the transverse energy missing from the event from non-interacting particles such as neutrinos. The calorimeters remain unchanged from Run I, even with the addition of the 2 T solenoidal magnet. The calorimeters are uranium - liquid argon ionization detectors, which detect particle showers. An electromagnetic particle shower occurs when a particle interacts with a material through scattering, uranium in this case, which may create a photon that can decay through pair production. This process is known as Bremsstrahlung, and is one of a handful of ways that a charged particle may lose its energy passing through a material. Bremsstrahlung is the dominant process for charged particles with a low mass, becoming less important at higher masses. This is because the equation corresponding to the emitted radiation contains a mass term of $1/m^6$. The resultant secondary particles may further interact with material creating a cascading shower of particles. With further cascades, the energy will be low enough to be absorbed through ionization in the material. Muons, being more massive than electrons, will tend not to undergo Bremsstrahlung and will instead be dominated by ionization in the material.

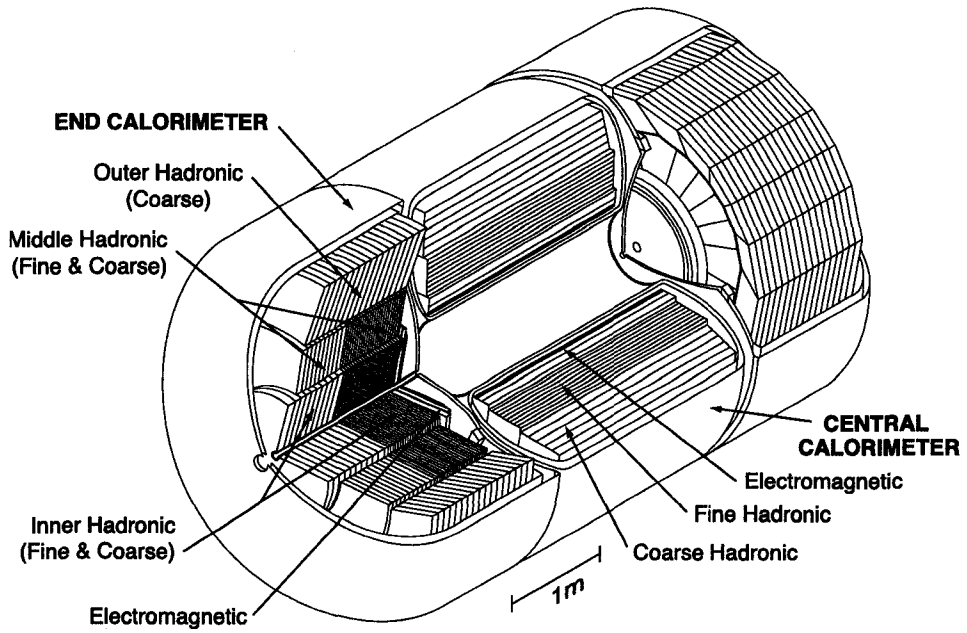

Figure 2.5: The segmented regions of the calorimeter: the outer, middle and inner hadronic regions, and the electromagnetic regions [20].

The calorimeter is split into three separate cryostats, which weigh 300 metric tons and contains 15,000 litres of liquid argon: a Central Calorimeter (CC, covering $|\eta| < 1$), and two End Calorimeters (EC, covering $1 < |\eta| < 4$) [18]. The use of three seperate cryostats provides for easy access to the CC, ECs, and the central detector when pulled apart for repairs or service work. Each cryostat is further segmented into three regions: an electromagnetic (EM), followed by a fine hadronic (FH) region, and a course hadronic (CH) region further out, which are shown in figure 2.5. The calorimeter is known as a compensating calorimeter which uses various methods in order to achieve an electron:hadron ratio of 1:1. This ratio is the difference in response signals of the calorimeter from EM and hadronic particles of the same incident energy and a ratio of 1:1 is required for a linear energy response during hadronic showers because hadronic showers contain an unknown electromagnetic component from π^0's as an example. This is done by varying the thickness of the absorber plates to change the amount of active shower layers that the particles can interact with, and also by using uranium absorber plates which can capture slow neutrons. A calorimeter optimized in such a way is able to achieve an energy

resolution which improves with increasing incident energy and is the goal of the calorimeters. Each region uses different absorbers: 3 mm (CC) or 4 mm (EC) depleted uranium plates in the EM section, 6 mm uranium-niobium plates in the fine hadronic section, and 46.5 mm copper (CC) or stainless steel (EC) plates in the coarse hadronic section. The materials used in the different regions were chosen to lower the cost while still achieving the 1:1 ratio. The use of three separate cryostats for the calorimeter, leads to gaps in the pseudorapidity covered ($0.8 < |\eta| < 1.4$). Within these gaps sits a layer of scintillator counters known as the Inter-Cryostat Detector (ICD), which covers a region of $1.1 < |\eta| < 1.4$. The ICD provides sampling in an otherwise unsampled area which would have degraded the energy resolution. Particles traversing the high density uranium can either cause an EM shower or in the case of hadrons, cause a hadronic shower through inelastic scattering. The shower of charged particles leaves the uranium and then ionizes the liquid argon. The liquid argon sits between two electrodes which provides an electric field to move the ionized charge. The negative charge drifts to signal boards 2.3 mm from the absorber plates with a charge collection time of 450 ns [18]. The absorber plates and signal boards all sit within a liquid argon cryostat and this configuration makes up the calorimeters.

The read-out cells for the calorimeter form pseudo-projective towers, named for the fact that the center of each cell lies on a ray that projects from the center of the interaction region (Figure 2.6). Each read-out cell has a transverse size comparable to that of the showers: 1-2 cm for EM showers, and farther out, 10 cm for hadronic showers which increase in size for larger values of η to avoid having very small cells. The read-out cells form a tower of $\Delta\eta \times \Delta\phi$, where $\Delta\eta = 0.2$ and $\Delta\phi = 0.2$. The energy within these 0.2×0.2 towers are used in the L1 and L2 calorimeter triggers. The signals from the detector are transferred to charge preamplifiers, which send the signal to be digitized in signal shapers and then they are sent to storage circuits. The signal is held for the Level 1 trigger decision for 4 μs in analogue storage devices (switched capacitor arrays), which are located below the cryostats. The signal is held further for the Level 2 trigger decision for an additional average time of 2 ms,

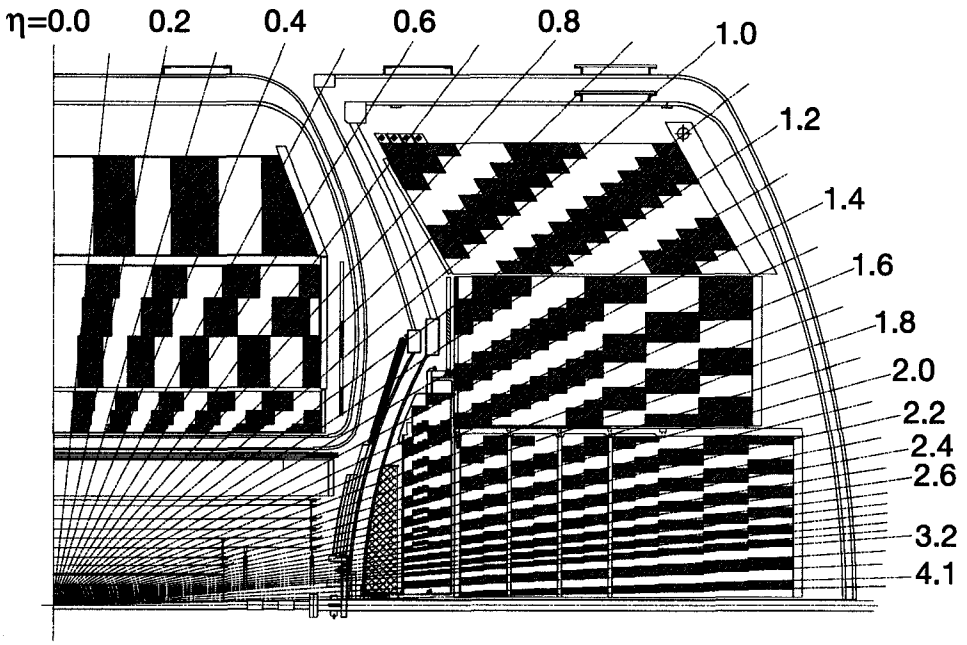

Figure 2.6: The pseudo-projective towers which form the cells that together constitute a signal read-out [20].

with a maximum time of 25 ms. Precision signals from the storage device is then read-out by the data acquisition system and used to form an L3 trigger decision.

2.4 The Muon System

Muons are much like electrons in that they have the same charge but are around 200 times more massive than an electron. This means that they lose less energy than an electron, through Bremsstrahlung, when passing through matter. This means that muons pass through the calorimeters and the pre-shower detectors easily, only losing a few GeV of energy. It is for this reason that the muon detection system is the farthest out radially from the collision event and it is designed with the intention of detecting muons which travel through the rest of the detector. The muon system is split into a central muon system, covering $|\eta| \leq 1.0$, and a forward muon system, which covers $1.0 \leq |\eta| \leq 2.0$ [18], for the same reasons as the electromagnetic calorimeter; to provide easy access to the components it surrounds. The central and forward muon systems use drift tubes, which are cylinders of gas that are ionized

when a muon passes through it, and are surrounded by a central high voltage wire. This provides an electric field which drags the charged particles to the wire for detection of the signal.

The central muon system uses Proportional Drift Tube (PDT) chambers, a toroidal magnet, the cosmic cap, and scintillation counters for triggering on muon events. The toroidal magnet gives a way to measure the low p_T muons, as well as providing a measurement of the p_T which is independent of the calorimeter system. This is also used to set a low p_T cut-off for the level 1 muon trigger. The PDT system itself registers hits which record the electron drift time, and the charge deposition. The drift time is the difference Δt, in the arrival time of the signal pulse and the read-out of the signal, which has a maximum of 450 ns. The cosmic cap provides a fast timing signal which can be used to associate a muon hit in the PDT with the appropriate bunch crossing. Since the cosmic cap covers the top and bottom of the detector, it can also detect hits which pass through the top and bottom to reject them as hits from the cosmic ray background. The PDT system is also supported by sets of scintillation counters on the top, upper sides, lower sides, and bottom of the central muon drift tubes. These provide for an association between a muon in the PDT with the bunch crossing from whence it came, which provides additional background rejection.

The forward muon system uses three layers of Mini Drift Tubes (MDT), end toroidal magnets, three layers of scintillation counters and shielding around the beam pipe for the muon system. The MDTs are similar to the PDTs, but have a shorter electron drift time below 132 ns [18]. The toroidal magnets work in the same way as with the central muon system, and allow for the measurement of the muon momentum. The system itself is not as good as the central tracker but provides for low resolution tracking and identification of muons.

2.5 The Trigger

Due to the high rate of particle interactions at the Tevatron, from high luminosities, a three tiered trigger system was implemented. The three levels of the trigger system were chosen due to the speed of the read-outs of the different detector components, specifically the tracking read-outs and the calorimeter read-outs. The goal of the trigger system was to filter the incoming data by selecting events to decrease the number of events into a more manageable size for data storage. At Level 1 (L1), the detector subsystems have only a short period of time to make available the information necessary to determine an accept for the event (35 μs or less). The rate of data accepted at L1 provides the Level 2 (L2) trigger system with a reduction in the rate of events leading to a greater amount of time available to make a decision. The amount of time available at L2 is around 100 μs or less, although in practice the time spent at L2 is around 50-60 μs in order to reduce the deadtime of the triggers. This additional time is used by the detector subsystems to send a more complete read-out of the data to L2 where more complex algorithms can be run than at the fast L1 trigger. Both L1 and L2 will buffer the data for Level 3 (L3), at which time the trigger system will have access to the full read-out of the detector subsystems.

The three distinct levels form a trigger system which accepts events at a lower rate at every level, but with a greater allowed complexity for the determination of an accepted event at the higher trigger levels. The approximate rate of trigger accepts at L1, L2 and L3 are about 2 kHz, 1 kHz, and 50 Hz respectively [18]. The trigger framework (TFW) interacts with L1 and L2 which determines the events that are passed to L3, shown schematically in figure 2.7. The first level (L1) is a hardware trigger that filters over bits set by the subdetectors. The system can take an "or" or an "and" of the trigger bits within a subdetector to test, for example, whether N calorimeter towers are above a threshold of X GeV. The second level (L2) is a combination of hardware and software which obtains a greater read-out from the detector subsystems and can use this read-out along with the information from L1 to make a decision. The software basis, the extra time available, and having

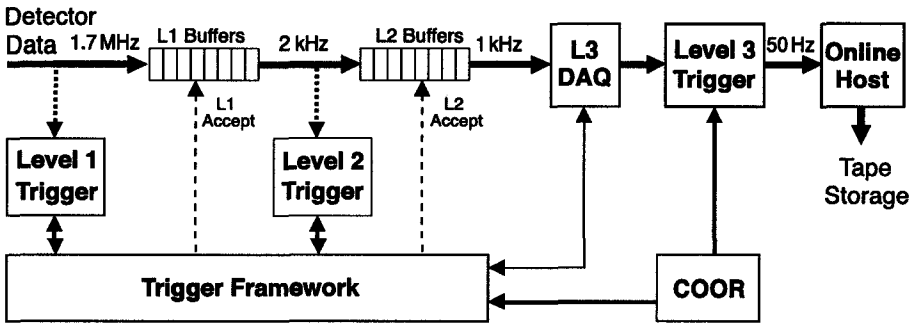

Figure 2.7: The Trigger Framework and its relation to Level 1, Level 2, Level 3, and the data acquisition system [20].

read-outs from multiple subdetectors allows for trigger decisions to be made based on individual objects such as electrons, muons, and jets, as well as correlations between the objects. The third level (L3) is sent candidates that have passed the L1 and L2 triggers, along with the full read-out of each detector subsystem. At L3, where the full detector read-out is available, physics objects and relations between the objects are generated by software algorithms called filter tools. The event is crudely reconstructed by these filter tools, and accepted events at this level are written to tape for offline reconstruction.

2.5.1 Level 1 trigger

The L1 trigger is a hardware trigger which examines every event, where an event is a collision or bunch crossing within the detector, and determines an interesting event from 4 subsystems: L1CAL, L1CTT, L1MUO and L1FPD. Within TFW for L1, 128 specific triggers can be programmed using up to 256 "AND-OR" terms which determines whether a given bunch crossing meets the conditions required to pass the trigger. Elements of the L1 trigger are allowed to be AND'd and OR'd together to form pseudo-terms. These will increase the efficiency of the triggers which may reduce backgrounds or the rate from low-p_T triggers. The L1CAL subsystem consists of the EM and hadronic energies which are formed into trigger towers from sums, in depth, and in transverse coordinates ($\Delta\eta \times \Delta\phi = 0.2 \times 0.2$) which were described earlier for the calorimeter. The EM transverse energies and

the total transverse energies (EM and hadronic) are used as variables for the trigger, which were converted from the tower energies. The E_T from the ICD towers are also used in the trigger calculations. The upgraded L1CAL subsystem had a set of trigger thresholds: 4 for the EM tower energy, and 4 for the total energy (EM + hadronic). Requirements, such as requiring 2 towers over a certain energy, are used in the trigger calculations. Future implentations at L1 will use a clustering algorithm to determine the proximity of one tower with an energy deposit to another. The L1CTT subsystem uses the discriminator data provided by the CFT, the CPS and the FPS detectors to perform simple hardware tuned reconstruction of the tracks of charged particles, which also triggers on the STT subsystem from the STT/SMT. The discriminator data provided are logic bits that are generated from wire signals from the subdetectors. L1CTT triggers on the tracks reconstructed in firmware which can be matched with EM cluster energy from the CPS detectors, while the FPS detector triggers on EM clusters on the FPS. Firmware is a hybrid of software and hardware, enabling the user to reprogram hardware gates as if they were software. The L1MUO subsystem uses the muon wire chambers, the muon scintillation counters and the tracks provided by L1CTT to look for muons within the event. Finally, the L1FPD subsystem can trigger on events using a combination of the nine FPD spectrometers, but it is currently not used in online triggers. As an example, the trigger MUW_W_L2M3_TRK10 has an L1 condition requiring a wide region, tight scintillator trigger, with a loose wire requirement for the muon.

2.5.2 Level 2 trigger

The L2 trigger is a combination hardware and software trigger which analyzes the inputs from events that have passed L1. The hardware read-outs to L2 constrained the system to report trigger decisions in the order that the events arrived. This meant that a farm of computers could not be used to process the events, and instead, Virtual Machine Environment (VME) crates were used. These crates hold custom input/output boards in a VME backplane (customized for the L2 trigger system) which reads out data to L3, and serial processors which subdivide the processing

tasks for L2.

The events are selected by a processor known as L2Global, which uses the 128 specific trigger bits set at L1. As a starting point, inputs from the calorimeter, CFT, CPS, FPS, SMT and muon subsystems are put through preprocessors which reconstruct the objects. These are then sent to the L2Global processor, which builds the physics objects, to decide whether an event has passed the trigger. There are L2 preprocessors for each of the detector subsystems along with the L2Global processor: L2Cal, L2Muon, L2PS, L2STT, and L2CTT. The L2Cal preprocessor identifies jets, electrons, photons and is planned to also calculate the transverse energy (E_T) in the calorimeter. The L2Muon preprocessor refines the muon candidates from L1 and contains the track p_T, η coordinates, ϕ coordinates, and quality and timing information. The L2PS preprocessor provides information on early shower development, and allows for a comparison with the calorimeter clusters or tracks that are found. The FPS detector also functions as a source of forward tracking, which is the only available source before L3. The L2STT preprocessor reconstructs charged particle tracks found in the CFT at L1 by using data from the SMT, which allows it to tag the decays of long-lived particles. The hits required in the SMT help reject the false track patterns found in the CFT and provide a more precise measure of the tracks and impact parameter of the tracks. Finally, the L2CTT preprocessor takes the input from L2STT as well as L1CTT and provides a p_T and impact parameter sorted list of tracks to the L2Global processor for triggering.

The L2Global processor examines correlations across all of the listed detector subsystems from the preprocessors listed earlier. It does this by creating global physics objects, from these subsystem preprocessor objects, on which trigger decisions can be made. The trigger conditions are specified by a configuration file to which changes can be made for inclusion in the next run, of which a run is simply a period of time with stable beam and no change in the trigger conditions. This file can be downloaded to L2Global at the start of every run, and processes each event based on which trigger bits fired at L1. These trigger bits are associated, by

the trigger list, to scripts at L2 which contain the trigger conditions that specifies whether a L2 trigger fired for that particular L1 bit. If any of the L2 scripts associated with a fired L1 bit accepts an event, the event is accepted by L2 and is sent to L3. As with the example for L1, MUW_W_L2M3_TRK10, at L2 we require 1 "medium" muon with a $p_T > 3$ GeV. If these conditions are satisfied, the event passes L2 and is sent to L3 for additional rejection of events.

2.5.3 Level 3 trigger

The data from L2 is sent to the L3 framework which runs the trigger software on a distributed set of farm nodes. These farm nodes typically have dual processor 1 GHz CPU equivalents with close to 100 nodes dedicated to processing the L3 trigger events. Data comes from the Read Out Crates (ROC) at L2 which have Single Board Computers (SBC) in each crate. The distribution to the farm nodes is controlled by a routing master, which communicates with the ROCs and the farm nodes to determine which nodes are free. The farm nodes run a package called ScriptRunner, which interfaces the L3 framework to the physics object tools. Each of these physics object tools has a reference set and a set of filter scripts: L3 jets and electrons, L3 muons, L3 missing transverse energy and L3 tracking. The reference sets define the physics objects and are input into the filter tools through the trigger list. These filter tools generate the physics objects and the relationships between them such as reconstructing leptons, vertices, $\not\!\!E_T$, and more. Through the trigger list and through these filters, conditions can be applied to the objects for the event to be accepted. The conditions, and order of the objects to be examined, are specified through the trigger list which will apply the L3 trigger for each L2 trigger bit that has been set; an event passes L3 if it passes all the filters for the given L2 trigger. After an event passes L3, it is then written to tape for storage.

The L3 jets and electrons tool has the full calorimeter and primary vertex position read-outs for its reconstruction algorithms. It applies a simple jet cone of $\sqrt{(\Delta\eta)^2 + (\Delta\phi)^2} = 0.25$, with a requirement on the transverse energy, an electromagnetic fraction > 0.9 and the transverse shower shape. The L3 muons use wire

and scintillator hits to reconstruct the muon tracks, and matches the tracks to those in the central tracker. At this point, the cosmic ray top and bottom caps are used to recognize muon hits that have a timing which indicates that it is not from the collision event. The L3 $\not\!\!E_T$ tool calculates the $\not\!\!E_T$ by summing the calorimeter energy geometrically with sums of rings in pseudorapidity. It provides the ability to trigger on $\not\!\!E_T$, the ϕ angle of $\not\!\!E_T$, the total scalar E_T and the $\not\!\!E_T$ resolution in the event (called the $\not\!\!E_T$ significance). Lastly, the L3 tracking tool uses clustering algorithms on the hits in the CFT to form track candidates which exceed a minimum trigger p_T, and a modified method similar to the CFT is used for the tracks in the SMT. This tool provides a primary vertex for triggering, and together with the track information, it provides the overall L3 trigger system with the ability to have an increased efficiency for low E_T triggers. Continuing the example trigger of MUW_W_L2M3_TRK10, at L3, we require a track with $p_T > 10$ GeV/c.

Chapter 3

Caf Trigger

3.1 Purpose

Physics analyses use data that is accepted by the DØ trigger system by triggers created to best increase the signal significance of the particular analysis. The triggers used to obtain the final data sample contribute to the overall error in the final calculations from the data. The triggers are used to define and determine which events may contain the relevant physics. It is important to know how to build a trigger which does not reject any of the relevant physics because events that are rejected are lost forever. The triggers, by definition, will obviously bias the accepted events so it is important to understand how the events are biased. The efficiency of a given trigger can be calculated as a function of the efficiency of triggering on the individual physics objects, and used to determine the probability of that trigger firing for a given event.

The *caf_trigger* package is based on the *top_trigger* [21] package used by the top quark analysis group at DØ, with the intention of providing a flexible and extendable trigger efficiency tool for other physics groups. Towards this end, it was designed from the ground up for use with DØ's new Common Analysis Format (CAF) environment, which itself uses the high energy physics analysis suite ROOT [22].

The trigger efficiency is determined by using Monte Carlo simulated (MC) events to determine whether a trigger would have accepted an event (fired). This can be

done in two ways. The first method uses Monte Carlo simulated events which are created first with an event generator such as PYTHIA [28] and then have had the detector response to the event simulated in GEANT [29] version 3. The trigger requirements can now be simulated using a simulated detector response which would, by definition of the simulated trigger, account for correlations and overlaps between the triggers. This type of direct simulation of the trigger requirements from Monte-Carlo is not suitable for precision measurements since it requires an accurate modeling of the trigger objects and other trigger quantities. The second method is based on using the probability, gathered from non-simulated data, that a single physics object would have passed a particular trigger requirements. These single object triggers can then be combined and folded into Monte-Carlo events (used with MC events) to give the probability of an event passing the trigger requirements. These probabilities can then be used to form a trigger weight within $[0, 1]$ for each event by folding them into Monte Carlo events for a single trigger object. The total event probability can be calculated as follows

$$P(L1, L2, L3) = P(L1) \times P(L2|L1) \times P(L3|L1, L2), \tag{3.1}$$

where $P(L2|L1)$ is the conditional probability for an event to fire the L2 trigger, given that it has fired the L1 trigger, and $\times$ is defined as multiplication of scalars. Similarly $P(L3|L1, L2)$ is the probability of an event firing the L3 trigger, given that it has fired the L1 and L2 triggers. This gives flexibility in the combination of the trigger conditions at the three trigger levels. The user can be given a total event probability for all the trigger levels or with individual probabilities for each trigger level. These probabilities are obtained assuming that the probability for a single object to satisfy a trigger condition is independent of the presence of other objects in the event. This is usually a safe assumption although it varies depending on the definition of the single object triggers. In situations where the single objects lack a correlation to other objects in the event, the probabilities can be reduced to a product of the probabilities for each object as in

$$P(obj_1, obj_2) = P(obj_1) \times P(obj_2), \tag{3.2}$$

where $P(obj_1, obj_2)$ is the probability of the first and second objects passing the trigger condition, which is not separable as shown if the objects probabilities are correlated. The methods of measuring the single object efficiencies that are used by *caf_trigger*, vary depending on whether the object is an electron, a muon or a jet. To calculate the efficiencies, these three types of objects share the need for unbiased real data samples. These data samples are then put through one of three packages which calculate the fraction of the offline reconstructed objects that satisfy the trigger conditions: *em_cert*, *muo_cert* and *trigeff_cafe* for electrons, muons and jets respectively.

3.2 Design and Implementation

To understand the advantages of a package as a CAF processor, it is useful to understand the advantages of a CAF based analysis over a traditional ROOT based analysis. CAF uses C++ classes which it calls processors. These processors are given a set of classes which interfaces with the root files: reconstructed objects, trigger information, object identification and detector data. Along with these objects, CAF provides a framework which automates event loops, and calls the processors for initialization, and termination of each event. There are three other useful features, of the many, provided within CAF: the ability to link processors together, the ability to store information in the event loop for another processor called afterwards, and the use of a user written configuration file to specify what CAF will run and what specified values the processors will use. The value of this common framework comes from its flexibility and simplification in the implementation of an analysis; a set of code may be reconfigured and used for different tasks, and the linked processors can be reordered for different conditions (see Figure 3.1). This allows for a trigger efficiency measurement, topological cuts, b-quark tagging, and many other studies which may use information provided by other packages through CAF.

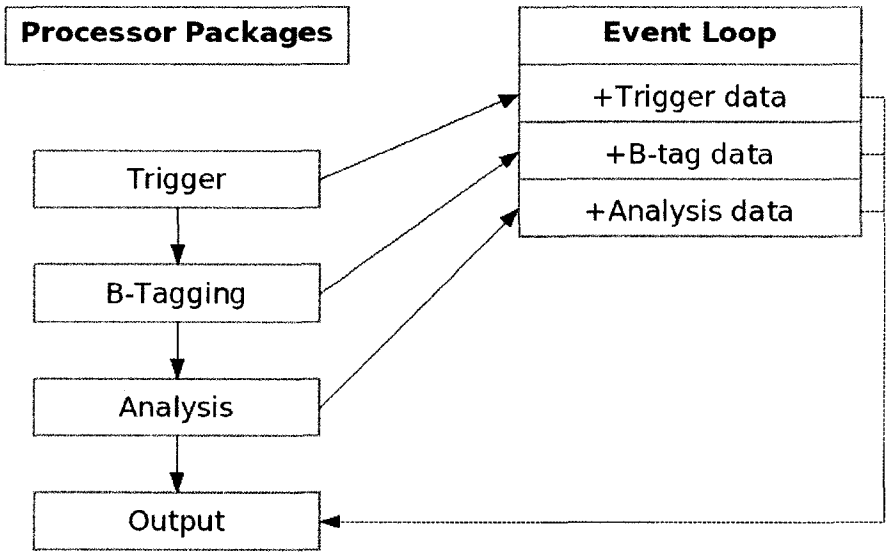

Figure 3.1: A graphical representation of the flexibility of the CAF processor model. Through each event loop, a CAF processor can add information, and use the information calculated by the previous processor in the chain. This information can then be extracted from the event loop for output, for example, to histograms.

The top level design of the package uses the concept of a chain of processors: the initialization processor, the probability processors and the final output processor. The probability processor will calculate the probability that a given trigger condition will pass an event. It contains the necessary combinatorics to apply the trigger condition to objects in the event. Any number of probability processors can be placed between the initialization and output processors, and their individual trigger weights can be combined as the user sees fit (see Figure 3.2).

In the first processor, cafTriggerEfficiency, an event is first searched for the physics objects that may be used in the probability calculations: electrons, muons, jets and $\not\!\!E_T$, as well as the number of each of these objects. The trigger lists and their associated luminosities are also retrieved from the user specified configuration files at this time. These objects are then temporarily stored in the event being processed for the next processor in the chain, the probability processors.

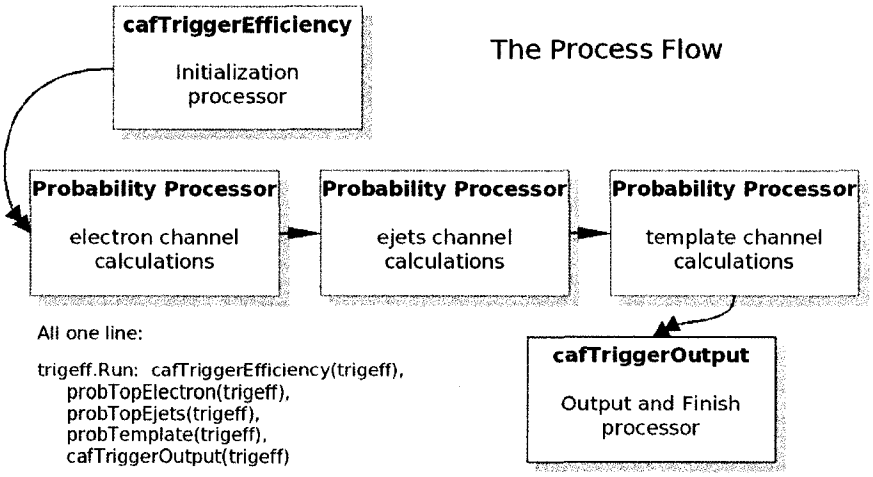

Figure 3.2: A hypothetical chain of caf_trigger processors which would produce a trigger weight for each of the three probability processors: probTopElectron, probTopEjets, and probTemplate.

3.2.1 Probability Processor

The probability processors inherit from a C++ base class which provides the writer of the processor with an interface to the turn-on curves and to the physics objects. Additionally, the base probability processor will place these objects back into the event with a specified name for further processors to use. The turn-on curves are text files which have been converted from the formats of *em_cert*, *muo_cert* and *trigeff_cafe*. *em_cert*, *muo_cert*, and *trigeff_cafe* are three packages used by the DØ collaboration to calculate turn-on curves for single object triggers (electrons, muons and jets respectively). The packages run on collected data, identify the physics objects particular to the packages, and test whether an object passes or fails a given trigger. A histogram of the passed objects, with respect to variables such as η, ϕ and p_T, is divided by a histogram of all of the particular physics object to produce a turn-on curve. These turn-on curves are output as a standardized text file for use in *caf_trigger*. *caf_trigger* can makes use of these text files through user specification in configuration files or the files can be hard coded into the probability processors. The efficiencies are accessed through methods which return the values of the bins, the efficiency specified by index variable, for a given object and variable.

The main method available to the processor is one which takes as its arguments the physics object and returns the probability that the physics object has passed the trigger. This uses the text-file stored turn-on curves to return a trigger efficiency, as well as uncertainties for each bin, in terms of variables such as η, ϕ and p_T. The simplest use of the returned probabilities is to calculate the probability that a group of physics objects fires the trigger. As an example, if there are n muons in the event, then one could calculate the probability of that event to fire a given muon trigger by looping over the n muons in the event to obtain the probabilities for each of the n muons. One minus the total probability of none of the muons passing the trigger condition would give the overall probability for the event to fire the given trigger,

$$P(\mu) = 1 - \prod_{i=1}^{n} [1 - P(\mu_i)] \,. \tag{3.3}$$

This processor will also calculate the uncertainty in the probability, returning an upper and lower value of the uncertainty with respect to the returned probability. The final turn-on curve produced from this calculation uses the uncertainty by creating a 1 standard deviation curve above and below the actual turn-on curve. This acts as a conservative estimate for the systematic uncertainty, where we say it is conservative due to overestimating the error in shifting the curve by 1 sigma from its mean. It is an overestimate because the uncertainties used in the calculation were originally correlated statistical uncertainties, which would lower the error below our estimate. If the probability is calculated by being split into the 3 trigger levels, the errors of the 3 levels are calculated independently and the uncertainties are added in quadrature.

There are also 4 other methods provided for each object that calculate the probability for the event to satisfy the trigger condition that X objects (where $X = 1, 2, 3, 4$) of N in the event meet a threshold requirement. These methods assume that the probability of a single object to satisfy a trigger condition is independent of other objects in the event. These are only for utility purposes since they do not calculate the correlations between the objects, and most triggers must have

their own combinatorics to account for the correlations. The calculations in these methods are shown in the following equations:

$$P(X\ of\ N) = 1 - \sum_{k=1}^{X}[1 - P(only\ obj_k\ of\ N)] \text{ and} \tag{3.4}$$

$$1 - P(only\ obj_k\ of\ N) = (1 - P(obj_k)) \times \prod_{l=1}^{k-1} P(obj_l), \tag{3.5}$$

where $P(X\ of\ N)$ is the probability for X of N total objects to pass the trigger conditions, $P(only\ obj_k\ of\ N)$ is the probability that only object k of N total objects has passed the trigger condition, and $P(obj_k)$ is the probability that object k of N has passed the trigger condition. The last definition for $P(obj_k)$ is irrespective of requirements on any of the other N-1 objects. The advantage of being able to create a chain of these processors is to allow for combinatorics that would otherwise be prohibitively difficult in a single processor. It is also possible to use the several single object trigger processors with a processor at the end of the chain to combine the probability results from each processor while accounting for correlations between the triggers. Each of the processors are specified with a name denoted as a "channel" which is used as an identifier by processors that come after. This gives each processor a unique identifier for event weights that it puts into the event. The event weight and the uncertainties are then mapped to the specified channel name and passed to the next processor in the chain, which may be another probability processor or the final output processor. At the end of every event, the event weights are sorted by their channel name and by the trigger list version that had been used to calculate the weights. Each of the triggers in a trigger list are associated with a luminosity block which is used to calculate an average event weight of the used trigger lists based on their luminosities. This is only valid for non-prescaled triggers, as prescaled triggers must be handled on an individual basis and a general method to account for the constantly changing prescales is prohibitively difficult.

3.2.2 The Output Processor

The final processor in the chain is the output processor, cafTriggerOutput. This processor stores, event by event, the values of the probability calculations that have been passed to it from the probability processors. These event weights are summed with the weights from previous calculations to give a total summed event weight when all events have been processed. This total weight is then divided by the number of events that have been processed to give an averaged trigger efficiency for all the events. These probability averages are displayed to the user along with the 1 standard deviation error on the values. The event by event probabilities are also stored in histograms which aids in diagnostic of the combinatorics within a processor by showing a distribution of the event weights.

Additionally, the output processor will write the individual event weights back into the event which allows another package after *caf_trigger* to use these event weights. As an example of a simple use of this is to plot a histogram of an object and its variable before *caf_trigger* is run, and after, in order to note the changes to the original distributions. As an example, when studying an electron trigger, one may plot a histogram of the leading electron p_T. The event by event weights are then applied to a second histogram which is plotted after *caf_trigger* in a chain. Dividing the weighted histogram by the unweighted histogram will give a probability curve which is similar to a trigger efficiency turn-on curve. This shows how the turn-on curves will look when folded into events and so it can be used to provide a rough check of the prediction with data. It is difficult to accurately check *caf_trigger* with data because *caf_trigger* is calculating a probability for an event to pass the trigger. This is not the same as passing an event or failing an event so it will give different results when compared with a set of trigger weights where each event is passed or failed. The way to ensure that *caf_trigger* is giving sensible results is by comparison with simpler trigger efficiencies made with *caf_trigger* with combinatorics that are known to be correct, and to ensure that the turn-on curves provided by the *em_cert*, *muo_cert* and *trigeff_cafe* packages are correct. The

latter can be achieved accurately through comparisons with data since they are providing a pass or fail criteria for each event to produce the turn-on curves.

Chapter 4

Electron Trigger "OR'ing"

4.1 Triggers of interest and "OR'ing"

The single top t-channel and s-channel production have well defined signatures: a high energy lepton, $\not\!\!E_T$, either one or two b-quark jets, and possible jets from extra quarks in the event. The single top signal signature is overwhelmed by a multitude of backgrounds, the most important of which are the $t\bar{t}$ production and the $W + jets$ backgrounds. The $W + jets$ background, may include Wcj (a W, c-quark jet, and a jet from a light quark), Wjj (a W, and two light quark jets), $Wb\bar{b}$ (a W, and two b-quark jets) and others. In the case of the $Wb\bar{b}$ background, which is prevalent in samples with 2 b-tagged jets, it may also include a lepton and a neutrino. This background cannot be decreased by just looking at the identified particles since it has the same particles as single top event. A way of cutting out this background is to require an offline cut on the reconstructed top mass. This cut is successful since the $W + jets$ events will not have a high reconstructed top mass. The cut on the t-quark mass, as well as cuts on the angular distribution of the decay particles, the particle momenta and other variables, are used to form a discriminant to reduce this background. The $t\bar{t}$ background will have the signature of a t-quark. The strategy noted earlier of looking for a lepton, $\not\!\!E_T$, and a number of jets is still useful against this background. The $t\bar{t}$ events may produce two high energy leptons (dilepton events) instead of one, and thus it is possible to reject these events by requiring only one lepton which may be a high energy jet that has faked a lepton in the event. Such a rejection on additional "hard" jets or leptons can be

Table 4.1: e+Jets triggers for trigger lists v8-v13. A trigger is a combination of the E1, E2, E3, or E4 terms from L1, L2 and L3. An example trigger for v13 would be, for E3_SHT15_2J_J25: CEM(2, 3)CEM(1, 9)_ncu from L1, L2CALEM(15, x) from L2, and Ele(ELE_NLV_SHT, 1, 15.) _Jet(SC5JET_9_PV1, 2, 20.) _Jet(SC5JET_9_PV1, 1, 25.) from L3.

v8-v11	**EM15_2JT15**
L1 all terms	CEM(1, 10)CJT(2, 5)_ncu
L2 all terms	EM(0.85, 10)_2JET(10)
L3 all terms	Ele(ELE_LOOSE_SH_T, 1, 15) _Jet(SCJET_9, 2, 15)
v12	**Ex_SHT15_2J20 (x = 1, 2, 3)**
L1 E1 terms	CEM(1, 11)_ncu
L1 E2 terms	CEM(2, 6)_ncu
L1 E3 terms	CEM(2, 3)CEM(1, 9)_ncu
L2 all terms	unrestricted trigger
L3 all terms	Ele(ELE_NLV_SHT, 1, 15) _Jet(SC5JET_9_PV3, 2, 20)
v13	**Ex_SHT15_2J_J25 (x = 1, 2, 3, 4)**
L1 E1 terms	CEM(1, 11)_ncu
L1 E2 terms	CEM(2, 6)_ncu
L1 E3 terms	CEM(2, 3)CEM(1, 9)_ncu
L1 E4 terms	CEM(1, 11)_ncu
L2 E1, E2, E3 terms	L2CALEM(15, x)
L2 E4 terms	L2CALEM(x, 11, 0.2)
L3 all terms	Ele(ELE_NLV_SHT, 1, 15.) _Jet(SC5JET_9_PV1, 2, 20.) _Jet(SC5JET_9_PV1, 1, 25.)

loosely defined [23] as any jet or lepton with $E_T > 15-25$ GeV, and $|\eta| < 2.5-4$. If only one of the t-quarks decay leptonically, then a restriction on the number of jets can be made to further filter the sample. The samples which maximize the signal to background ratio are $W + 2jets$ and $W + 3jets$ events, where two of the jets are from a b-quark[1].

The signature of the single top event as described, clearly indicates that an optimal trigger to use for this type of event is one which looks for an electron or muon and some jets. The focus of this trigger study is on electron triggers,

[1]Although a jet may be from a b-quark, the ability to identify a b jet is based on the tracking efficiency, misreconstructed jets, the detection of jets and jets that have been incorrectly identified as jets or as other particles. These, among others, make the tagging of b jets a non-trivial exercise.

Table 4.2: e+Jets triggers for trigger lists v13.3-v14. A trigger is a combination of the E1, E2, E3, or E4 terms from L1, L2 and L3. An example trigger for v13.3 would be, for E3_SHT15_2J_J30: CEM(1, 11)_ncu from L1, L2CALEM(x, 11, 0.2) from L2, and Ele(ELE_NLV_SHT, 1, 15.) _Jet(SC5JET_9_PV1, 2, 20.) _Jet(SC5JET_9_PV1, 1, 30.) from L3.

v13.3	**Ex_SHT15_2J_J30 (x = 1, 2, 3, 4)**
L1 E1 terms	CEM(1, 11)_ncu
L1 E2 terms	CEM(2, 6)_ncu
L1 E3 terms	CEM(2, 3)CEM(1, 9)_ncu
L1 E4 terms	CEM(1, 11)_ncu
L2 E1, E2, E3 terms	L2CALEM(15, x)
L2 E4 terms	L2CALEM(x, 11, 0.2)
L3 all terms	Ele(ELE_NLV_SHT, 1, 15.) _Jet(SC5JET_9_PV1, 2, 20.) _Jet(SC5JET_9_PV1, 1, 30.)
v14	**Ex_SHT15_2J_J30 (x = 1, 3, 4)**
L1 E1 terms	CEM(1, 12)_ncu
L1 E3 terms	CEM(2, 3)CEM(1, 9)_ncu
L1 E4 terms	CEM(2, 6)_ncu
L2 all terms	L2CALEM(15, x)
L3 all terms	Ele(ELE_NLV_SHT, 1, 15.) _Jet(SC5JET_9_PV3, 2, 20.) _Jet(SC5JET_9_PV3, 1, 25.)

Table 4.3: Glossary of L1 and L2 terms.

Term	Definition
L1:	
CEM(x, n)	x Calorimeter EM energy trigger towers with $E_T > n\ GeV$
CJT(x, n)	x Calorimeter total energy trigger towers with $E_T > n\ GeV$
ncu	Not Calorimeter Unsuppressed readout
L2:	
EM(x, n)	EM candidate with an EM fraction $> x$ and with $E_T > n\ GeV$
L2CALEM(n, x)	requires a standard EM cluster with a threshold $\geq n\ GeV$
L2CALEM(x, n, l)	requires a single EM object with isolation $< l$ and $E_T > n\ GeV$
xJET(n)	x jet candidates with $E_T > n$

the electron and jets trigger (e+Jets) and improvements that can be made to this trigger. The current trigger used is the set of e+Jets triggers, shown in Tables (4.1) and (4.2), that identifies a signal-like event based on criteria imposed on the electron and the jets in the event. The goal is to look at the improvements to the signal acceptance by first taking the OR of the e+Jets triggers with the single electron triggers for each trigger list. The reasoning behind this is that the single electron triggers have tighter constraints on the definition of an electron than the e+Jets triggers. The more stringent constraints are due to the single electron triggers only having a single object criteria for accepting events. This means that, to keep the trigger accept rates reasonable, the single electron triggers must reject events with a higher threshold than the e+Jets triggers. In most cases, the p_T threshold of the electron triggers are higher than those of the e+Jets triggers meaning that the OR of these triggers will accept signals of the e+Jets type or electron events without the jet requirement. First, the e+Jets and single electron triggers will be defined, followed by the results of performing an OR of the triggers.

The generic definitions for the trigger terms such as $CEM(x, n)$ and $L2CALEM(n, x)$ are shown in Tables (4.3) and (4.4), which also hold a glossary of terms used

Table 4.4: Glossary of L3 terms.

Term	**Definition**
L3:	
Ele(ELE_LOOSE, x, n, 0., l)	x LOOSE electrons, $\|\eta\| < l$, with $E_T > n$ *GeV*
Ele(ELE_VLOOSE, x, n, 0., l)	x VLOOSE electrons, $\|\eta\| < l$, with transverse shower shape (_T), and $E_T > n$ *GeV*
Ele(ELE_LOOSE_SH_T, x, n, 0., l)	x LOOSE electrons, $\|\eta\| < l$, with transverse shower shape (_T), and $E_T > n$ *GeV*
Ele(ELE_NLV, x, n, 0., l)	x LOOSE electrons, $\|\eta\| < l$, with non-linearity and vertex corrections used, with no shower shape requirements and $E_T > n$ *GeV*
Ele(ELE_NLV_VL, x, n, 0., l)	x VLOOSE electrons, $\|\eta\| < l$, with non-linearity and vertex corrections used, with no shower shape requirements and $E_T > n$ *GeV*
Ele(ELE_NLV_SH, x, n, 0., l)	x electrons, $\|\eta\| < l$, with non-linearity and vertex corrections used, with loose shower shape, and $E_T > n$ *GeV*
Ele(ELE_NLV_SHT, x, n, 0., l)	x electrons, $\|\eta\| < l$, with non-linearity and vertex corrections used, with tight shower shape requirements, and $E_T > n$ *GeV*
Ele(ELE_NLV_NC, x, n, 0., l)	x electrons, $\|\eta\| < l$, with non-linearity and vertex corrections used, and $E_T > n$ *GeV*
Jet(SCJET_b, x, n)	x jets are found with $E_T > n$ *GeV* using a simple cone algorithm on jets of b *GeV*
Jet(SCaJET_b_PVc, x, n)	x jets with $E_T > n$ *GeV* using simple cone algorithm with cone size 0.a on jets of b *GeV*, and using the primary vertex tool with tracks of c *GeV*

by the single electron triggers. The trigger list version is denoted with v8-v11, v12, v13, v13.3 and v14, denoting the version numbers where the triggers were changed. Within this table, the term "transverse shower shape (_T)" and "tight shower shape" are defined by the electromagnetic showering on each of the EM layers of the calorimeter. The EM layers are divided into 4 radial distances labelled EM1, EM2, EM3 and EM4, of which EM4 is the closest to the hadronic layers and farthest from the beam pipe. The transverse shower shape is defined as the width of the shower on the 3 EM layers, labelled EMxW, for each layer. The widths are calculated in the following equation:

$$\Delta r = \frac{\sum E_i \sqrt{(\phi_i - \phi)^2 + (\eta_i - \eta)^2}}{\sum E_i}, \tag{4.1}$$

where ϕ and η are the energy weighted positions of the cluster, and ϕ_i and η_i are particles in the shower. The transverse shower shape cut (_T) is defined as $EM1W < 0.09$, $EM2W < 0.08$ and $EM3W < 0.05$ in units of Δr. This is a tighter requirement than the "tight" shower shape requirement because it is an older definition preceeding the current definitions of tight and loose. The tight shower shape requirement is similarly defined for the CC ($EM1W < 1.8$, $EM2W < 1.4$ and $EM3W < 1.15$) and EC ($EM1W < 1.0$, $EM2W < 1.0$ and $EM3W < 1.2$) regions of the calorimeter. The loose shower shape requirement is defined for the CC ($EM1W < 2.3$, $EM2W < 1.7$ and $EM3W < 1.5$) and EC ($EM1W < 1.4$, $EM2W < 1.35$ and $EM3W < 1.4$) regions of the calorimeter. The terms LOOSE and VLOOSE electron are determined by the EM fraction, which is the faction of the total energy deposited in the EM layers of the calorimeter: EM fraction > 0.9 for LOOSE, and EM fraction > 0.8 for VLOOSE. The trigger terms with *ncu* refer to hot cells in the calorimeter that would provide an incorrect measurement of the energy deposition. The *ncu* trigger requires that the events accepted, use the suppressed hot cell readout.

The detailed break down of the e+Jets triggers for trigger lists v8-v14 are shown in Tables (4.1) and (4.2). Generally, the e+Jets trigger requires a low p_T electron

with 2 jets which may be defined with differing energies. Changes to the triggers were made over time to account for the increasing luminousities seen at the Tevatron. In addition, these changes improved the efficiency of the triggers with techniques such as isolation of the electron and track matching on the jets. The threshold for the electron p_T was raised at L1 as the trigger lists progressed (from EM15_2JT15 to E1_2J terms), as well as changes to the jet thresholds. This was to counter the rising luminosity and was not done to improve the trigger efficiencies.

Single electron triggers, which generally trigger on a higher energy threshold than with e+Jets, were also used for single top events. The break down of the single electron triggers for trigger lists v8-v14 are shown in Tables (4.5) and (4.6). The basic single electron triggers are more varied than the e+Jets triggers, which is a result of the need to keep the trigger accept rate reasonable while not rejecting the signal events. These triggers require additional cuts to keep the trigger rates low because there is less to cut on; there is no jet requirement. The marked difference is seen at L3, as the electron triggering is similar to that of the e+Jets triggers at L1, and L2. At L3, the electron requirements for the e+Jets trigger have a threshold at electron $p_T > 15$ GeV/c, whereas the single electron trigger varies from a 20 GeV/c threshold to one at 90 GeV/c. The difference is in the cuts applied to the shape of the EM shower and the EM fraction. The single electron triggers have a more efficient event acceptance for high energy electrons, although it may reject single top events. This is because the triggers have no requirements on the jets and a higher requirement on the electron. Single top events with the required jets but with a lower electron p_T than required may be rejected.

The single electron triggers are high p_T electron triggers which have a good efficiency for high p_T events like some of the single top events. The e+Jets triggers have a low p_T threshold, to accept the low p_T single top events, which includes a jet requirement. Since not all of the single top events will have both an electron and the required jets to pass the trigger, whereas most single top events will have a high p_T electron, the trigger efficiencies of the e+Jets triggers are lower than that

Table 4.5: Single electron triggers for trigger lists v8-v13. A trigger is a combination of the E1, E2, E3, or E4 terms from L1, L2 and L3. For single electron triggers, it may also be a combination of MX and HI terms. An example trigger for v8-11 would be, for EM_MX_EMFR8: CEM(1, 15)_ncu from L1, an unrestricted trigger from L2, and Ele(ELE_VLOOSE,1,40.,0.,3.) from L3.

v8-v11	**EM_MX, EM_MX_SH, EM_MX_EMFR8, EM_HI, EM_HI_SH, EM_HI_EMFR8**
L1 EM_MX terms	CEM(1, 15)_ncu
L1 EM_HI terms	CEM(1, 10)_ncu
L2 all terms	unrestricted trigger
L3 EM_(MX/HI)	Ele(ELE_LOOSE, 1, 30. ,0. , 3.)
L3 EM_(MX/HI)_SH	Ele(ELE_LOOSE_SH_T, 1, 20., 0., 3.)
L3 EM_(MX/HI)_EMFR8	Ele(ELE_VLOOSE,1,40.,0.,3.)
v12	**Ex_SHT20, Ex_SH30, E1_L50, E1_VL70 (x = 1, 2, 3)**
L1 E1 terms	CEM(1, 11)_ncu
L1 E2 terms	CEM(2, 6)_ncu
L1 E3 terms	CEM(2,3)CEM(1,9)_ncu
L2 all terms	unrestricted trigger
L3 Ex_SHT20 (x = 1, 2, 3)	Ele(ELE_NLV_SHT, 1, 20., 0., 3.6)
L3 Ex_SH30 (x = 1, 2, 3)	Ele(ELE_NLV_SH, 1, 30., 0., 3.6)
L3 E1_L50	Ele(ELE_NLV, 1, 50., 0., 3.6)
L3 E1_VL70	Ele(ELE_NLV_VL, 1, 70., 0., 3.6)
v13	**Ex_SHT20, Ex_SH30, E1_L50, E1_NC90 (x = 1, 2, 3, 4)**
L1 E1 terms	CEM(1, 11)_ncu
L1 E2 terms	CEM(2, 6)_ncu
L1 E3 terms	CEM(2, 3)CEM(1, 9)_ncu
L1 E4 terms	CEM(1, 11)_ncu
L2 E1, E2, E3 terms	L2CALEM(15, x)
L2 E4 terms	L2CALEM(x, 11, 0.2)
L3 Ex_SHT20 (x = 1, 2, 3, 4)	Ele(ELE_NLV_SHT, 1, 20., 0., 3.6)
L3 Ex_SH30 (x = 1, 2, 3, 4)	Ele(ELE_NLV_SH, 1, 30., 0., 3.6)
L3 E1_L50	Ele(ELE_NLV, 1, 50., 0., 3.6)
L3 E1_NC90	Ele(ELE_NLV_NC, 1, 90., 0., 3.6)

Table 4.6: Single electron triggers for trigger lists v13.2-v14. A trigger is a combination of the E1, E2, E3, or E4 terms from L1, L2 and L3. See Tables (4.1) and (4.2) for an example.

v13.2	**Ex_SHT22, Ex_SH30, E1_L70, E1_NC90 (x = 1, 2, 3, 4)**
L1 E1 terms	CEM(1, 11)_ncu
L1 E2 terms	CEM(2, 6)_ncu
L1 E3 terms	CEM(2, 3)CEM(1, 9)_ncu
L1 E4 terms	CEM(1, 11)_ncu
L2 E1, E2, E3 terms	L2CALEM(15, x)
L2 E4 terms	L2CALEM(x, 11, 0.2)
L3 Ex_SHT22 (x = 1, 2, 3, 4)	Ele(ELE_NLV_SHT, 1, 22., 0., 3.6)
L3 Ex_SH30 (x = 1, 2, 3, 4)	Ele(ELE_NLV_SH, 1, 30., 0., 3.6)
L3 E1_L50	Ele(ELE_NLV, 1, 50., 0., 3.6)
L3 E1_NC90	Ele(ELE_NLV_NC, 1, 90., 0., 3.6)
v14	**Ex_SHT25, Ex_SH35, E1_L70 (x = 1, 3, 4)**
L1 E1, E3 terms	CEM(1, 12)_ncu
L1 E4 terms	CEM(2, 6)_ncu
L2 E1, E4 terms	L2CALEM(15, x)
L2 E3 terms	L2CALEM(x, 11, 0.2)
L3 Ex_SHT25 (x = 1, 3, 4)	Ele(ELE_NLV_SHT, 1, 25., 0., 3.6)
L3 Ex_SH35 (x = 1, 3, 4)	Ele(ELE_NLV_SH, 1, 35., 0., 3.6)
L3 E1_L70	Ele(ELE_NLV, 1, 70., 0., 3.6)

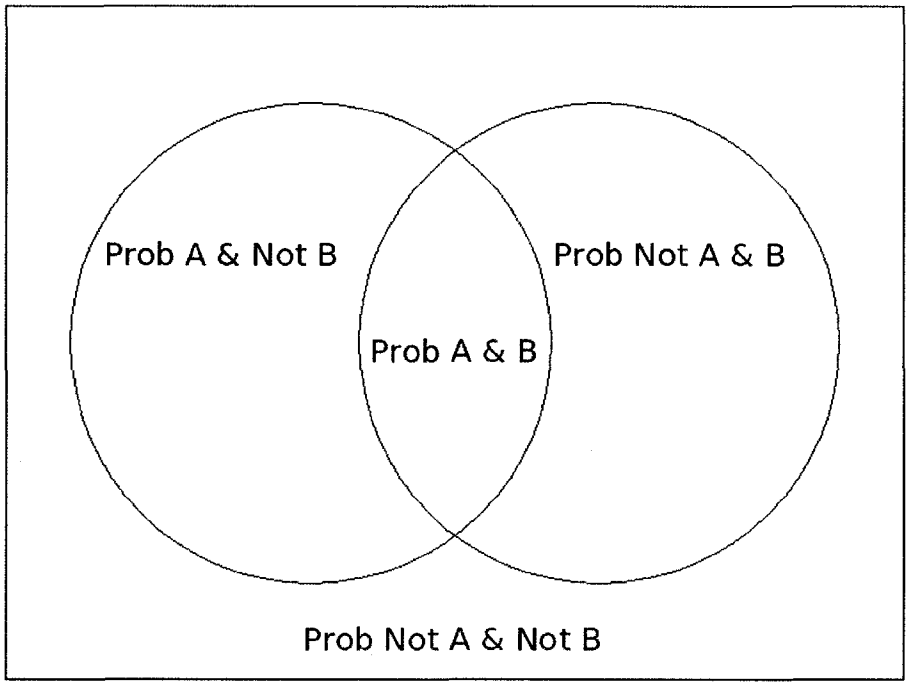

Figure 4.1: Given two triggers, A and B, the combination of firing can occur in four ways: A and B both fire, A fires but not B, B fires but not A, and neither A nor B fire.

of the single electron triggers. Taking the OR of one with the other should provide a higher acceptance for our signal. Given two triggers, T_A and T_B, the combination of firing can occur in four ways: T_A and T_B both fire, T_A fires but not T_B, T_B fires but not T_A, and neither T_A nor T_B fire. This shows, through a simple Venn diagram in Figure (4.1), the following probability equation

$$P(T_A \vee T_B) = P(T_A) + P(T_B) - P(T_A \wedge T_B), \tag{4.2}$$

where $P(T_A)$ is the probability of T_A firing, $(T_A \vee T_B)$ means (T_A or T_B), and $(T_A \wedge T_B)$ means (T_A and T_B). Table (4.1) and (4.2) show that the electron trigger criteria is varied while the jet criteria remain constant within each trigger list. So, for a given trigger list, the probability of the e+Jets trigger may be factored out into its component pieces. Let $P(T_{ES})$ be the probability of an event passing the single electron criteria, $P(T_{EJ})$ be the probability of an event passing the e+Jets trigger

criteria, $P(E_{EJ})$ be the electron criteria of the e+Jets trigger, and $P(J_{EJ})$ be the jets criteria of the e+Jets trigger. Then the probability of $T_{ES} \vee T_{EJ}$ is given by

$$P(T_{ES} \vee T_{EJ}) = P(T_{ES}) + P(E_{EJ}) \times P(J_{EJ}) - P(T_{ES} \wedge E_{EJ}) \times P(J_{EJ}). \quad (4.3)$$

The equation shows that $P(T_{ES} \vee T_{EJ})$ does not equate to the simple quantity $P(T_{ES} \vee E_{EJ}) \times P(J_{EJ})$, because there are correlations between the electron triggers that must be taken into account. Due to the abundance of the words "OR" and "AND", I will be using the notation ($A^{OR} = A^1 \vee A^2 \vee ...$), defined to be the OR of triggers (A^1, A^2, ...). Each of the quantities on the right hand side of Equation (4.3) can be calculated: the trigger turn-on curves will first be produced in the *em_cert* [24] package for the OR's of the single electron triggers ($T^{OR}_{ES} = T^1_{ES} \vee T^2_{ES} \vee ...$), the OR's of the electron portion of the e+Jets triggers ($E^{OR}_{EJ} = E^1_{EJ} \vee E^2_{EJ} \vee ...$), and the AND's of all these triggers ($T^{OR}_{ES} \wedge E^{OR}_{EJ}$). These will be combined with jet turn-on curves produced with the *trigeff_cafe* package [25].

The trigger efficiencies are not so easily handled when the triggers are prescaled. To prescale a trigger is to only select and accept a fraction of the number of trigger accepts to be stored. This is done with a simple condition such as "keep 1 in 300 accepts", and is performed at higher luminosities for loose trigger conditions to lower the acceptance rate to keep within the read-out bandwidth. This is considered a last resort, and is only performed if there are no other possible cuts that can be made to lower the rate. The triggers studied here were not prescaled, although the normalization when combining triggers is accounted for in the *em_cert* and *trigeff_cafe* packages since they apply the trigger conditions directly to the data. The processor created in *caf_trigger* to calculate the OR of the triggers was created with the ability to handle prescaled triggers with the method shown in reference [26]. It is not a trivial task to account for the prescales, as each individual trigger may have a different prescale at different luminousities. This feature of the processor was not used for the study discussed here.

4.2 The Turn-on Curves

The turn-on curves for the electron and jet portion of the triggers are created in two seperate packages: *em_cert* and *trigeff_cafe*. Ideally, one is interested in calculating the trigger efficiency and producing a turn-on curve by testing a desired object against a trigger as follows,

$$Efficiency = \frac{Signal\ events : Pass\ trigger}{Signal\ events : Total}. \tag{4.4}$$

All events that have been recorded during data taking must pass one or more triggers. If the efficiencies are then measured for these events, using triggers which are correlated with the ones in the online trigger, then the measurements will have a bias. As an example, recorded events that pass an electron trigger with the requirement $p_T > 20$ GeV/c are very likely to pass an electron requirement of $p_T > 10$ GeV/c, which would make any studies of the later trigger meaningless. Further, trigger conditions vary from requiring track matches to requiring an amount of energy in the calorimeter and may then bias other triggers with similar requirements.

The *em_cert* package uses a method to minimize the trigger bias known as tag and probe. This method uses the decays of the Z boson, into two fermions or two jets, in order to identify the objects, and test the triggers against these objects. The goal of the tag and probe method in *em_cert* is to identify events in which the electrons reconstruct to a Z boson, which has decayed via $Z \rightarrow ee$. The first step is to look at events with at least two good EM clusters that reconstruct into a Z which may be used as the tag and probe electrons. This is done by requiring that the invariant mass of the tag and probe EM clusters sits between 65 GeV/c^2 and 200 GeV/c^2. At least one of the two EM clusters are required to have a $E_T > 25$ GeV and matched to a track within the detector. This we shall call $em1$. The second EM cluster, $em2$, is required to be matched to an isolated track. $em1$ must now pass a few extra conditions before it is accepted as a tag: the first is a likelihood cut for the electron, and the second is a requirement that $em1$ passes at least one of the electron triggers. The likelihood cut is a cut on the probability that the identified object is

an electron, which is constructed with various requirements for the electron. As an example, a likelihood probability for an electron can be constructed by requiring that the electron has a matched track, that the track is isolated, and that the electron deposited the majority of its energy in the EM calorimeter. These requirements would then be combined, through weighting, into a likelihood probability that the object is an electron. If $em1$ passes the likelihood cut and at least one of the electron triggers, then $em2$ is taken as the probe (assumed to be a real electron from a $Z \rightarrow ee$ decay) and is tested against every electron trigger. Two histograms are filled: one for the probe electrons that have passed the trigger, and one with the probe electrons regardless of whether it has or has not passed the trigger. An efficiency is then calculated as follows,

$$Efficiency\ with\ valid\ tag\ electron = \frac{Probe\ electrons : Pass\ trigger}{Probe\ electrons : Total}, \quad (4.5)$$

where the histogram is filled if the event has a valid tag and the ratio is taken of the events with a probe passing the trigger to all events with a valid tag. After $em2$ has been tested, the roles of the two EM clusters switch. The process begins again with the requirement that the two good EM clusters reconstruct into a Z. $em2$ is now put through the same conditions to be a tag electron. For those events where $em2$ can be a tag, $em1$ becomes the probe and is tested against the electron triggers and those that pass are used to fill the same histogram. Depending on the methods used in the selection of the tag electron, there may arise correlations between the tag and probe objects. As an example, the efficiency could be dependent on the primary vertex position [24]. The selection of the tag electron could bias the vertex distribution which would bias the probe electron identification efficiency. These biases can be avoided with a careful understanding of the selection methods used for the tag and probe objects. There is no simple answer for how to handle the potential biases, as they may be different for each selection method. In this example, one could simply choose not to use a trigger which depends on the primary vertex position, but it may be detrimental to the goal of the analysis.

While the tag and probe method is applicable to jets, it is not the method that was used in *trigeff_cafe*. This is because the method would require a Z decaying into two quarks to produce the jets for the reconstruction. Due to the high background production of jets, it is not a clean signal of the Z as with leptons and so *trigeff_cafe* must rely on another method to ensure an unbiased sample. The trigger bias, in this case, is removed by a selection criteria on the data events. The events used to calculate the trigger efficiency are chosen by requiring that the events were accept with a trigger which does not use the calorimeter. This ensures that the jet triggers under study will not be biased by any calorimeter triggering. This is done by using muon triggers; specifically those that have not used any calorimeter information. The trigger efficiency is then calculated, after the selection of the required data, through a simple ratio

$$Efficiency = \frac{good\ jets\ and\ Jets : Pass\ jet\ trigger}{good\ jets\ and\ Jets : Total}, \tag{4.6}$$

where a good jet is defined by a set of quality cuts such as energy deposited in the calorimeter and electron vetos. There is one more set of turn-on curves that is relevant to the calculation, and that is the correlation of an electron object with a jet object. This arises through a calculation of the efficiency for an electron, which has passed the electron trigger conditions, to fire a jet trigger. This is referred to as the SCJET efficiency and is calculated through EM shaping of the jets at L3. The efficiency is calculated within *em_cert* by taking the events which have passed the electron trigger of interest, and seeing if these events pass a jet trigger condition. This is done at various thresholds of the jet p_T (15, 20, 25, 30, and 35 GeV/c) in the following equation:

$$Efficiency\ SCJET = \frac{Events\ pass(electron\ trigger\ AND\ jet\ threshold)}{Events\ pass(electron\ trigger)}, \tag{4.7}$$

where *Events pass(electron trigger)* are the events that pass the electron trigger criteria and *Events pass(electron trigger AND jet threshold)* are the events

that pass the jet criteria at a specified threshold. The SCJET turn-on curves are used in *caf_trigger* to produce a trigger efficiency for $P(E_{EJ}) \times P(J_{EJ})$ and for $P(T_{ES} \wedge E_{EJ}) \times P(J_{EJ})$. This is done by including in the calculation of $P(J_{EJ})$, the probability of all jet-like objects to pass the trigger conditions. This will include both the jets, and the electrons which fake a jet. A representative plot of these turn-on curves can be seen in Figure (4.2). The turn-on curves were only produced for $p_T = 20, 25, 30$ and 35 GeV/c and it has been assumed that for a threshold of $p_T = 15$ GeV/c, the electrons will always fire the jet triggers at that threshold. This assumption has been made because all electrons in the event will have a p_T greater than 15 GeV/c, and will satisfy the requirements for the 15 GeV/c jet trigger threshold. Since the v8-v11 trigger lists used an L3 trigger term of $Ele(ELE\_LOOSE\_SH\_T, 1, 15)\_Jet(SCJET\_9, 2, 15)$ (Table (4.1)), which has a p_T threshold of 15 GeV/c, the SCJET turn-on curves gave a strict probability of 1.0.

The *em_cert* package was run on data events which have either two electrons with $p_T > 12$ GeV/c, or two tracks which are associated with reconstructed electrons with track $p_T > 15$ GeV/c. The $trigeff\_cafe$ package was run on data events with a non-calorimeter muon trigger. In both cases the data used was reconstructed with the DØ reconstruction program, DØReco, version p17.09.03: *em_cert* on a subset of the data with 2 electrons with high p_T where high is defined as earlier (CSskim-2EMhighpt-PASS3-p17.09.03), and $trigeff\_cafe$ on a similar skim of the data with jets (CSskim-TOPJETTRIG-PASS3-p17.09.03) [27]. The turn-on curves output from *em_cert* are shown in Appendix A, while the turn-on curves output from $trigeff\_cafe$ were already included in the *caf_trigger* package by Thomas Gadfort[2], and so it was unnecessary to recreate them.

The turn-on curves are produced in the form of histograms of the efficiencies, defined in Equation (4.4), binned in variables of p_T, η, and others. Ideal turn-on curves of single trigger, single object efficiencies are step functions at the threshold that has been set. In practice, the resolution of the detector smears measurements

[2] A citation is unavailable as the production of these turn-on curves was not documented.

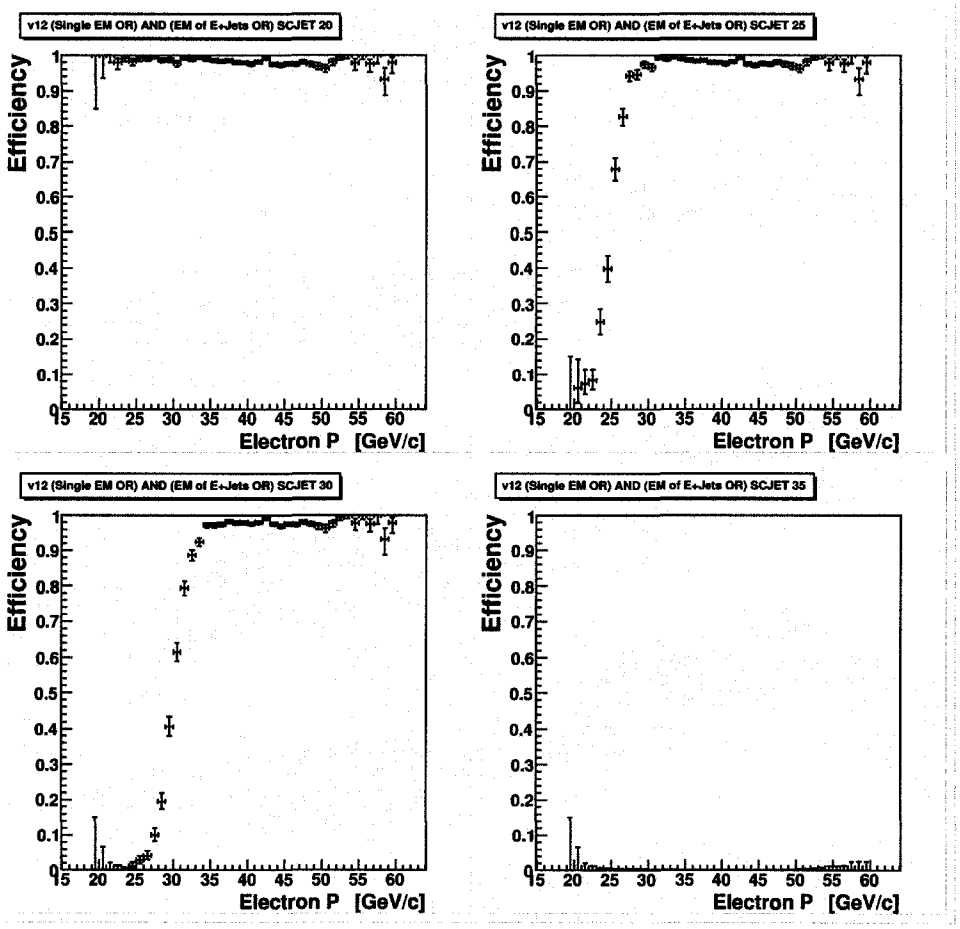

Figure 4.2: The turn-on curve for the v12 electron triggers firing a jet trigger, $(E1\_SHT20 \vee E2\_SHT20 \vee E3\_SHT20 \vee E1\_SH30 \vee E2\_SH30 \vee E3\_SH30 \vee E1\_L50 \vee E1\_VL70) \wedge E1\_SHT15 \wedge E2\_SHT15 \wedge E3\_SHT15 \wedge SCJET(y)$, where y = p_T threshold of 20, 25, 30 and 35 GeV/c. The errors are not constrained to be between 0 and 1, but *caf_trigger* will constrain these errors. The turn-on curves for the other trigger lists can be found in Appendix A.

of a value to a gaussian distribution. Since the trigger efficiency is a convolution of this gaussian distribution with the step function efficiency curve, the turn-on curves in p_T can be fitted to an error function of the form

$$f(p_T) = \frac{A_2}{2}\left(1 + \mathrm{Erf}\left(\frac{p_T - A_0}{\sqrt{2}A_1}\right)\right), \tag{4.8}$$

where Erf() is the error function, A_0 is the x-coordinate midpoint, A_1 is the slope at the midpoint and A_2 is the plateau of the turn-on curve. The use of OR'd triggers precludes the use of this fit as the turn-on curves are no longer those of a single trigger. This means that the turn-on curve will be a combination of more than one error function which cannot be fitted to a single error function. A clear example of this can be seen in Figure (4.3) which shows two plateaux after the "turn-on": one with $26 < p_T < 32$ GeV/c and the other with $p_T > 32$ GeV/c. Although the single triggers can be fitted to an error function, they were not fitted for consistency with the OR'd triggers. The turn-on curves for the other trigger lists are in Appendix A.

4.3 Trigger Efficiencies in caf_trigger

4.3.1 The Single Electron and e+Jets Triggers

Probability processors with the combinatorics to calculate the single electron, e+Jets, and single electron $\wedge$ e+Jets efficiencies are used in *caf_trigger* to calculate the efficiency for single electron $\vee$ e+Jets. This is done with 4 processors: the single electron processor using the E_{ES} (equivalent notation to T_{ES}) turn-on curves, the e+Jets processor using the E_{EJ} and J_{EJ} turn-on curves, the e+Jets processor using the $E_{ES} \wedge E_{EJ}$ and J_{EJ} turn-on curves, and a final combination processor (Figure 4.4).

The combinatorics of the single electron trigger use the combined L1, L2, and L3 turn-on curves produced in *em_cert*. The combinatorics involved were discussed in chapter 3, giving a probability for the event to fire an electron trigger with the assumption that the electrons in the event are independent. The probability of each electron, with a given p_T, not to fire the given trigger is calculated. These are then

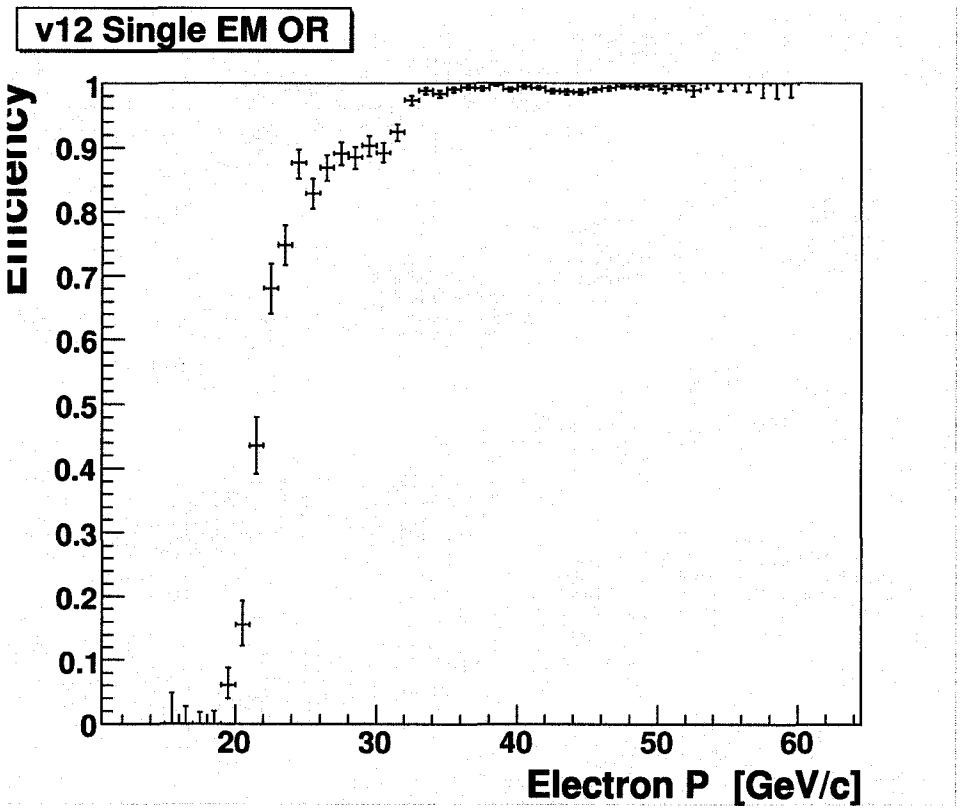

Figure 4.3: The turn-on curve for the v12 single electron triggers, $E1\_SHT20 \vee E2\_SHT20 \vee E3\_SHT20 \vee E1\_SH30 \vee E2\_SH30 \vee E3\_SH30 \vee E1\_L50 \vee E1\_VL70$ (Table (4.5)). This example shows a step at around 30 GeV which comes from OR'ing of turn-on curves with multiple thresholds.

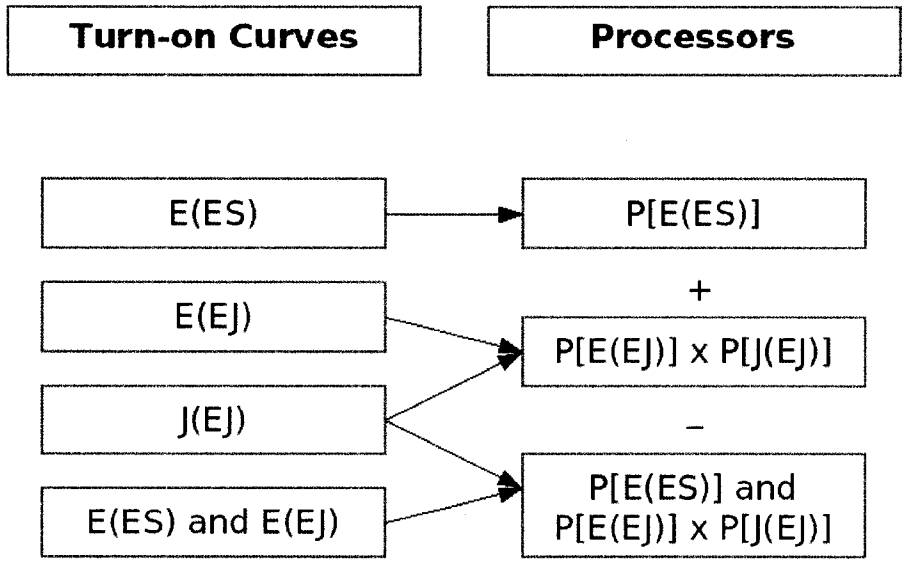

Figure 4.4: A graphical representation of the processors. The turn-on curves feed into 3 processors, which are combined in a final processor as $P(E_{ES}) + P(E_{EJ}) \times P(J_{EJ}) - [P(E_{ES} \wedge P(E_{EJ})] \times P(J_{EJ})$.

multiplied together to obtain the the probability of all of the electrons not to fire the trigger, which is subtracted from 1 to give the probability of the electrons firing the trigger

$$P(T_{ES}) = 1 - \prod_{i=1}^{n} [1 - P(e_i)] . \tag{4.9}$$

The combinatorics of the e+Jets trigger is factored into two pieces: the electron probability and the jet probability. The electron probability and the jet probability are calculated separately as $P(E_{EJ})$ and $P(J_{EJ})$. These are then multiplied together to get the total e+Jets trigger efficiency.

The electron probability is calculated in the same method as the single electron probability but with the e+Jets combined L1, L2, and L3 turn-on curves for the electron (Replace T_{ES} with E_{EJ} in Equation (4.9)). The jet probability is calculated using individual L1, L2, and L3 turn-on curves for trigger lists v8-v11, and a single combined (L1, L2 and L3) turn-on curve for trigger lists v12-v14. This was split in such a way to allow for the combined L3 turn-on curves provided by *em_cert* to

be used with similar turn-on curves provided by $trigeff\_cafe$. The probabilities are first split by trigger list and then by the p_T trigger thresholds: 15, 20, 25, and 30 GeV/c. This is done in order to include the probabilities for an electron to fake a jet at the various thresholds that are used by the e+Jets trigger. The p_T threshold at 35 GeV/c is not used since it is not in any of the current e+Jets triggers (up to p_T = 30 GeV/c in trigger list v13.3). Of the listed thresholds, up to 3 of them will be used for an e+Jets trigger condition, but the remaining threshold is available for future use. The probabilities for jet objects to fire jet trigger conditions are calculated with the added probabilities from electrons faking jets in the event. These are then split into the same p_T thresholds as for the electron and treated as probabilities for the jet to fire the jet trigger.

This can be seen more clearly with a look at the procedure of a probability calculation. The v12-v14 trigger lists have two jet criteria set at one threshold X and Y, where $X = Y$ (v12) or two different thresholds X and Y, where $X > Y$ (v13-v14). This sets a criteria for at least one of the "jets" to have $E_T > X$ GeV and at least one more jet with $E_T > Y$ GeV, where "jets" refer to objects that have satisfied the jet criteria but may be another particle like an electron. Two calculations are made: $P_1(L3)$ is a calculation that none of the "jets" have $E_T > X$ GeV,

$$P_1(L3) = \prod_{i=1}^{n} \left[1 - P_X^{L3}(jet_i)\right], \tag{4.10}$$

and $P_2(L3)$ is a calculation that at most one of the "jets" has $E_T > X$ GeV and there are no other "jets" with $E_T > Y$ GeV, where $X > Y$,

$$P_2(L3) = \sum_{i=1}^{n} \left[P_X^{L3}(jet_i) \prod_{j=1, i\neq j}^{n} \left(1 - P_Y^{L3}(jet_j)\right) \right]. \tag{4.11}$$

$P_X^{L3}(jet_i)$ and $P_Y^{L3}(jet_j)$ are the probabilities for a jet at level 3 to have satisfied the trigger threshold of $E_T > X$ or $> Y$ GeV, n = the number of true jets + the number of electrons, and jet_i is the i^{th} jet-like object (jet-like objects may include electrons). The probability to fire the trigger is

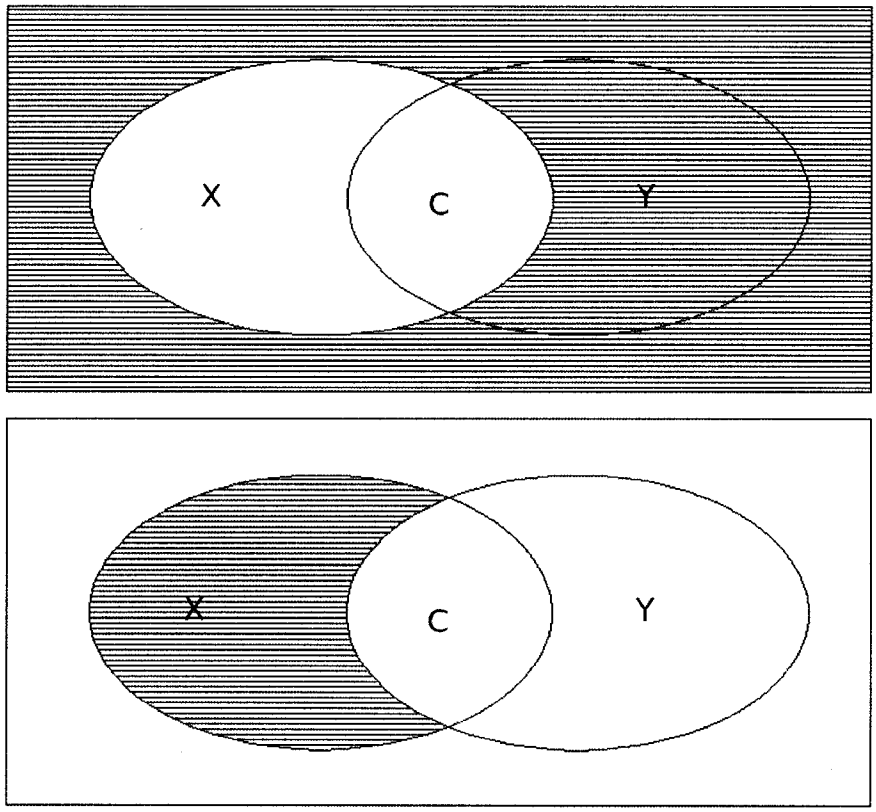

Figure 4.5: The top diagram shows the calculation of $P_1(L3)$, while the bottom diagram shows the calculation of $P_2(L3)$. The X, and Y circles represent their respective trigger thresholds. From Equation (4.12), $1 - P_1(L3) - P_2(L3)$ can easily be seen as the central overlap of the two circles, denoted as C.

$$P(J_{EJ}) = 1 - P_1(L3) - P_2(L3), \tag{4.12}$$

which calculates the probability for at least one of the "jets" to be above X GeV, added to the probability of at most one "jet" to be below X GeV while at least one "jet" is above Y GeV. The calculations that lead up to Equation (4.12) are most easily seen in a Venn diagram, shown in Figure (4.5).

The calculation method requires a slight modification for use with the v8-v11 trigger lists, since these trigger lists used seperate L1, L2, and L3 trigger turn-on curves. This was done for historical reasons, as at the time of this study, the decision had not been formalized as to whether a single combined turn-on curve would be

use instead of 3 seperate turn-on curves for each level. As with the v12 trigger list, the trigger criteria require 2 jets above a set threshold, i.e. $X = Y$ in Equation (4.11). Equation (4.10) is also modified to the following,

$$P_1(L1) = \prod_{i=1}^{n} \left[1 - P_X^{L1}(jet_i)\right], \text{ and } P_1(L2) = \prod_{i=1}^{n} \left[1 - P_X^{L2}(jet_i)\right], \tag{4.13}$$

where $P_1(L1)$ is the probability that none of the "jets" fire the level 1 and $P_1(L2)$ is the probability that none of the "jets" fire the level 2 trigger having fired the level 1 trigger. The probability to fire the trigger for v8-v11 trigger lists is calculated using

$$P(J_{EJ}) = (1 - P_1(L1)) \times (1 - P_1(L2)) \times [1 - P_1(L3) - P_2(L3))]. \tag{4.14}$$

The jet calculations together with $P(E_{EJ})$ produce the quantity $P(E_{EJ}) \times P(J_{EJ})$, required for the final trigger OR'ing. The final calculation uses the e+Jets probability processor with the OR'd triggers, $E_S \wedge E_{EJ}$, for the electron portion and the regular jet turn-on curves for the jet portion. This produces the final value of the single electron AND e+Jets probabilities ($P(E_{ES} \wedge E_{EJ}) \times P(J_{EJ})$), needed to produce the final single electron OR e+Jets probabilities ($P(T_{ES} \vee T_{EJ})$).

Once the three processors ($P(E_{ES})$, $P(E_{EJ}) \times P(J_{EJ})$, and $P(E_{ES} \wedge E_{EJ}) \times P(J_{EJ})$) have completed their calculations in the event, these event weighting probability values are sent to a combination processor. The combination processor calculates the probability that the event fired the trigger $T_{ES} \vee T_{EJ}$ by using Equation (4.3).

4.3.2 "OR'ing" and Results

The e+Jets triggers, used by the top analysis group for their existing physics analysis, are EM15_2JT15 for v8-v11, E1_SHT15_2J20 for the v12, E1_SHT15_2J_J25 for v13, and E1_SHT15_2J_J30 for the v13.3-v14 trigger lists and shall be referred to as the "main e+Jets triggers". The turn-on curves available for single top trigger studies, were created by the top group and fitted to an error function (Equation

(4.8)). The OR'd turn-on curves produced for our analysis could not be fitted to a single error function, due to differing thresholds in the different triggers. This lead to unphysical results, where the combination A OR B would at times be lower than either A or B alone. This meant that a direct comparison could not be made to the error function fitted turn-on curves, so new unfitted turn-on curves were produced to have a reference to gauge any differences due to the OR'ing. The unfitted main e+Jets turn-on curves were used in a chain of *caf_trigger* processors: the 3 processors required for the OR'ing, the combination processor, and the unfitted main e+Jets calculation.

caf_trigger runs at the end of a chain of processes that are used during analysis to ensure good quality data. Only a few of these processes will remove a significant, tens of percents, of the total number of events. These are defined in the *top_cafe* [33] package, and full details can be found therein. Here is a brief summary of the main selection criteria:

Event Quality An event can be tagged as one which is not of good data quality based on many different criteria, a few of which are: the proton/anti-proton beam is noisy (the beam has a halo of particles which has not been removed), detector miscalibration, hot cells in the calorimeter which register false hits, and others. The selection of good quality data is performed by defining luminousity bins of good runs and bad runs.

Duplicate Event Finder Self explanatory. This looks for duplicate events and rejects them.

Electron Selection The cuts on good electrons are defined by the energy deposition in the calorimeter and how well an electron matches to a track. This study uses top_tightCC, defined in *top_cafe*, which requires an electron $p_T > 15$ GeV/c, an EM fraction of 0.9, an isolation of 0.2, to be within the CC with $|\eta| < 1.1$, among others.

Jet Selection The jet selection algorithm defines a jet cone ($\Delta r < 0.5$) to en-

sure that the object is a jet and not a misidentified particle, ensure that it matches to a track, and other criteria. This study uses a GoodJCCB, defined in *top_cafe*, which requires 2-4 jets within a detector $|\eta|$ of 3.4, and a jet $p_T > 15$ GeV/c. This is then used for single top by requiring a maximum of 2 bad jets (not a good jet), the leading jet $p_T > 25$ GeV/c with $|\eta| < 2.5$, and the second leading jet $p_T > 20$ GeV/c.

Missing Transverse Energy This cut is designed to ensure that the events have enough $\not\!\!E_T$ to account for the missing energy in a single top decay. First, matching is performed between the electrons and the $\not\!\!E_T$, and jets and the $\not\!\!E_T$ as a first check on whether the electrons and jets were misreconstructed as $\not\!\!E_T$. Then a cut is imposed on the missing energy of $15 < \not\!\!E_T < 200$ GeV.

Triangle Cut The triangle cut is a topological cut used to ensure that the $\not\!\!E_T$ calculated in the event has not resulted from misreconstructed electrons or jets. This creates false energy in the parallel or anti-parallel to the misreconstructed object. These misreconstructed events can be removed by imposing cuts on $\not\!\!E_T - \Delta\phi(\text{electrons}, \not\!\!E_T)$ and $\not\!\!E_T - \Delta\phi(\text{jets}, \not\!\!E_T)$, the two of which define planes where the objects lie with respect to the missing transverse energy.

These processes remove events before *caf_trigger* or any analysis is performed, and have been included in order to produce the trigger efficiencies for the events that are used for the final analysis. The two sets of Monte-Carlo examined are *tb-evbb* (electron, neutrino and 2 *b*-quarks) and *tqb-evbqb* (electron, neutrino, 2 *b*-quarks and another light quark) single top events that were produced in a custom implementation of CompHEP [30] known as SingleTop [31]. This creates parton-level events which are then processed in PYTHIA [28] and EVTGEN [32]. These events are then processed with a full GEANT [29] version 3 simulation of the DØ detector. The *tb* and *tqb* MC sets contain 92,620 (MC cross section of 0.067 pb) and 130,068 (MC cross section of 0.309 pb) events respectively. These are reduced to 41,233 (*tb*) and 52,715 (*tqb*) by the electron and jet selections, and further reduced to 35,346 (*tb*) and 46,058 (*tqb*) events by the topological cuts shown earlier.

Table 4.7: Trigger lists and associated luminosities.

Trigger List	v8	v9	v10	v11	v12	v13.0	v13.3	v14
Luminosity (pb^{-1})	4.21	21.42	8.48	54.32	195.29	46.77	263.98	211.19

Table 4.8: Luminosity weighted $T_{ES} \vee T_{EJ}$ versus original e+Jets trigger efficiencies, for the leading electron, of the *tb-evbb* and *tqb-evbqb* MC with trigger lists v8-v14.

tb $E_S \vee EJ$	$89.9 \pm^{1.0}_{0.7}$ % *syst* $\pm$ 0.2% *stat*
tb e+Jets original	$83.6 \pm^{0.6}_{0.5}$ % *syst* $\pm$ 0.2% *stat*
tqb $E_S \vee EJ$	$89.5 \pm^{1.0}_{0.9}$ % *syst* $\pm$ 0.2% *stat*
tqb e+Jets original	$82.2 \pm^{0.6}_{0.6}$ % *syst* $\pm$ 0.2% *stat*

The luminosity numbers used for each trigger list, shown in Table (4.7), are from data skims which are defined with a number of cuts: one jet with $E_T > 15$ GeV and detector $|\eta| < 2.5$, one loose EM object with $p_T > 15$ GeV/c, $\not\!\!E_T > 15$ GeV, good data quality, and finally the e+Jets trigger. These come from the luminosity block, which is the fundamental unit of time for the luminosity measurement. These blocks are indexed by a luminosity block number which is incremented during the run. The luminosity is then calculated independently for each block [34]. These numbers are used to weight the trigger lists within *caf_trigger* in order to produce the correct luminosity averaged trigger efficiency.

The single electron OR'd triggers have higher electron thresholds which give significantly different turn-on curves compared to the e+Jets OR'd triggers. The acceptance probability distributions in p_T of the leading electron for $P(E_{ES})$, $P(E_{EJ}) \times P(J_{EJ})$, and $P(E_{ES} \wedge E_{EJ}) \times P(J_{EJ})$ are shown in Figure (4.6) for the *tb* and *tqb* MC. These are combined on an event by event basis to form the final $P(E_{ES} \vee E_{EJ}) \times P(J_{EJ})$ seen in Figure (4.7).

Although the single electron trigger has a visually higher efficiency in the graphs, the e+Jets trigger has the actual advantage numerically: $84.1 \pm^{0.6}_{0.5}$% *tb* MC and $82.7 \pm^{0.6}_{0.6}$% *tqb* MC for the OR'd e+Jets triggers and $81.7 \pm^{0.4}_{0.2}$% *tb* MC and $81.1 \pm^{0.4}_{0.2}$% *tqb* MC for the OR'd single electron triggers. The luminosity averaged trigger effi-

ciencies, for trigger lists v8-v14, are shown in Table (4.8). There is a general trend for the trigger efficiencies to fall with new trigger lists due to the changes made to account for the higher event rates, with the exception of the rise in efficiencies from v12-v13. This rise corresponded with the introduction of two different thresholds for the jet requirements, rather than a single threshold for both jets.

So far, we've discussed how *caf_trigger* calculates the systematic uncertainties, but we have not discussed the statistical uncertainties in the efficiencies shown in Table (4.8). The event weight distribution is a bimodal distribution, with the two modes centred on 0 and the plateau value of the turn-on curve. We can achieve a conservative estimate of the statistical uncertainties by considering a purely boolean, bimodal distribution with event weights at either 0 or h, where $h \leq 1$. In practice, the distribution will never be a purely boolean, bimodal distribution, but will contain points between our two extreme event weights. This will serve to lower the standard deviation, leading to a smaller statistical uncertainty. The standard deviation is then calculated as

$$\sigma = \sqrt{(1-h)(h)^2 + (h)(1-h)^2}. \tag{4.15}$$

We then use Equation (4.15), with the values in Table (4.8), and the number of events (35,346 (tb) and 46,058 (tqb)) to estimate the statistical uncertainties. This was done by taking $\sigma/\sqrt{N}$, where N is the number of events, and was shown as the *stat* uncertainty in Table (4.8).

From the values of the efficiencies, we can calculate the increase in efficiency from the original e+Jets triggers to the new OR'd triggers. The $T_{ES} \vee T_{EJ}$ trigger shows an overall gain of $6.3 \pm^{1.2}_{0.9}$ % *syst* for the tb MC, and $7.3 \pm^{1.2}_{1.1}$ % *syst* for the tqb MC. The statistical error has not been quoted for the differences because the calculations with the old triggers and the new OR'd triggers used the same MC sample. This meant that the errors were correlated, which lowers the overall error from the already small 0.2% to a number which is not significant when compared with the systematic uncertainties.

Table 4.9: $T_{ES} \vee T_{EJ}$ versus original e+Jets trigger efficiencies, for the leading electron, of the *tb-eνbb* and *tqb-eνbqb* MC versus trigger list. Trigger lists v8-v11 have been combined since there are no changes to the triggers during that period.

Trigger List	v8-v11	v12	v13.0	v13.3	v14
tb $T_{ES} \vee T_{EJ}$	91.1%	89.9%	90.6%	90.3%	88.7%
tb e+Jets original	89.9%	82.8%	83.5%	82.8%	82.6%
tqb $T_{ES} \vee T_{EJ}$	90.9%	89.6%	90.2%	89.8%	88.4%
tqb e+Jets original	89.4%	81.3%	82.0%	81.0%	81.1%

It is informative to look at the trigger efficiencies for the individual trigger lists which are shown in Table (4.9) for the *tb* and *tqb* MC. The production of uncertainties for the individual trigger lists would be computationally consuming as 3 calculations must be run, to obtain the individual efficiencies, on each trigger list: one for the mean value, and two more for the upper and lower turn-on curves to produce the systematic errors. Furthermore, the calculation of these errors would not provide any further information as they are of the same order of magnitude as for the full set of trigger lists. The gains for trigger lists v8-v11 are minimal compared with the later trigger lists but the efficiencies of the e+Jets triggers before calculating the OR'd results are already near 90% efficiency.

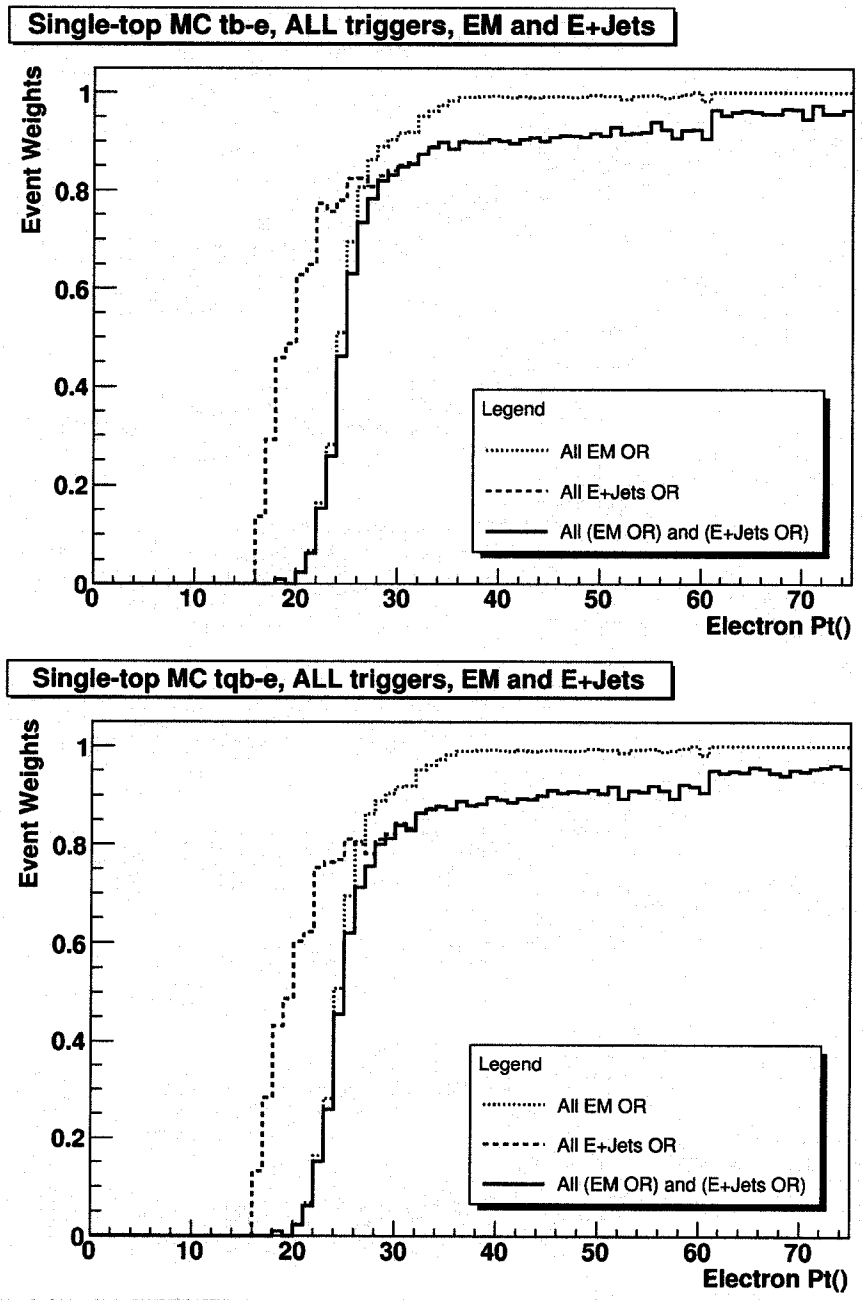

Figure 4.6: $P(E_{ES})$, $P(E_{EJ}) \times P(J_{EJ})$, and $P(E_{ES} \wedge E_{EJ}) \times P(J_{EJ})$ trigger probability distribution in p_T for the leading electron. The "All (EM OR) and (E+Jets OR)" curve is the AND term used to calculate the final efficiency.

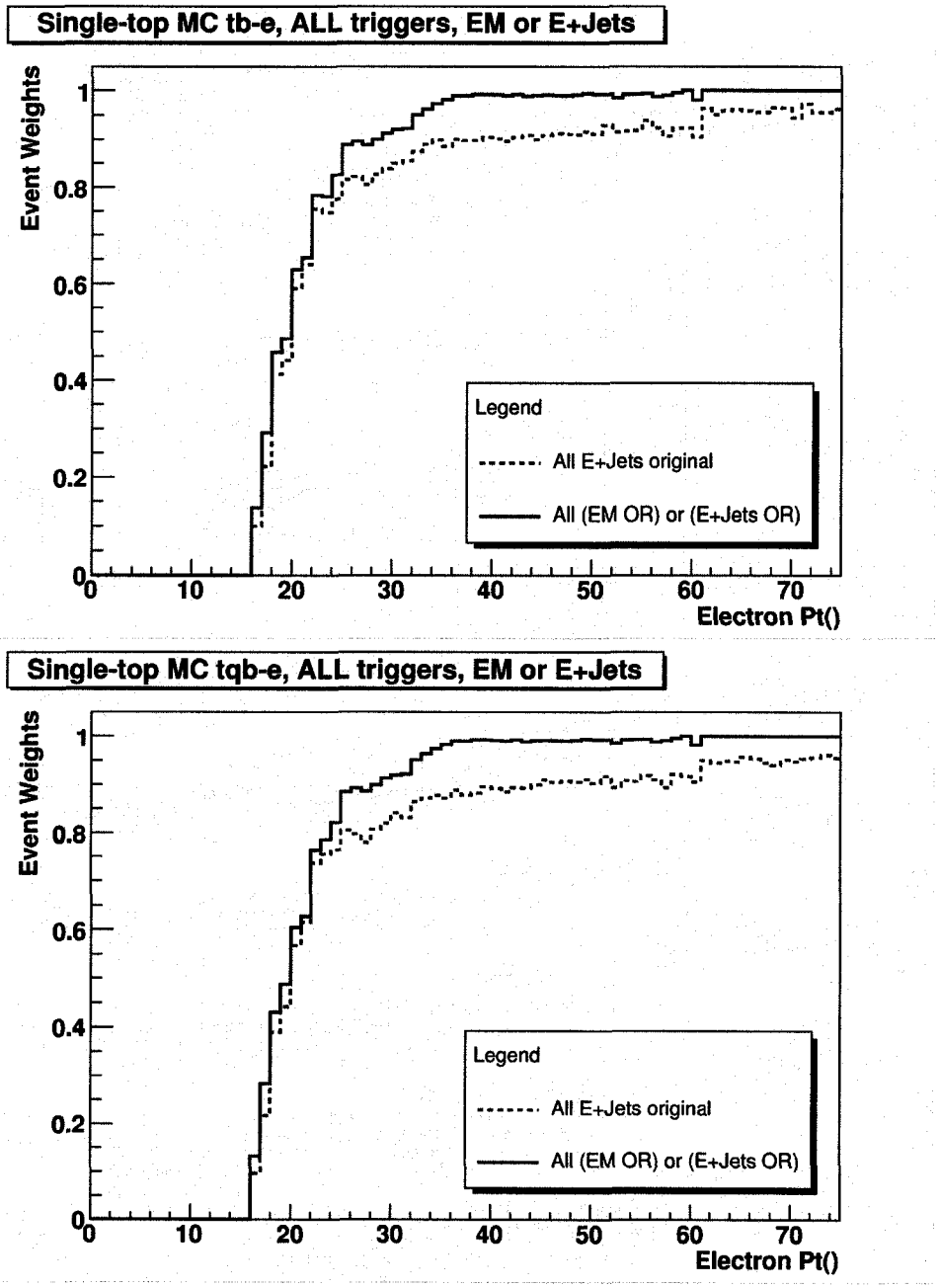

Figure 4.7: $T_{ES} \vee T_{EJ}$ versus original e+Jets trigger probability distribution in p_T for the leading electron. The $T_{ES} \vee T_{EJ}$ triggers show an overall gain of $6.3\pm^{1.2}_{0.9}\%$ for the *tb* MC (top figure) and $7.3\pm^{1.2}_{1.1}\%$ for the *tqb* MC (bottom figure).

Chapter 5

Discussion

The goal of this study was to look at increasing the efficiency of the triggers used in the analysis of the single top event signal. The *caf_trigger* package was created for the purpose of folding trigger efficiencies derived from unbiased data to Monte-Carlo simulated events in order to produce a probability for the signal events to pass the given triggers. *caf_trigger* is now used by the DØ collaboration for trigger efficiency studies in many different analyses and was recently used for the single top analysis in 2007. Trigger turn-on curves were created in the *em_cert* package of a logical OR of the single electron triggers, a logical OR of the e+Jets triggers, and the AND of these two trigger groups, which were to be used in *caf_trigger*. The goal was to deduce whether this trigger OR'ing would have a noticeable effect on the efficiency of triggering on single top events.

The results of this study were shown in Chapter 4. It has been determined that there is an increase in the efficiency of the triggers from performing the single electron OR'ing and the e+Jets OR'ing. A brief analysis of the consequences of these results will be covered in this chapter, followed by future work that could proceed from this point. First, we will look at the c+Jets OR'ing and its benefit over the original e+Jets trigger. Next, we will look at what the increase in the trigger efficiency means when looking for the single top signal events.

Throughout the remainder of this chapter, we will want to discuss the effect of these triggers on background events to the single top signal. The two main backgrounds are the W+Jets background and the $t\bar{t}$ background. The $t\bar{t}$ will have an

event signature that contains two top quarks and the resulting decays. We consider the $t\bar{t}$ background in which one of the W bosons decays leptonically and the other decays to two light quarks. The W+Jets background, while it may contain a similar looking signature, is not a reliable indicator of the trigger efficiencies. This is due to the analysis framework that has been executed before the trigger efficiency processors. The selections will have already significantly lowered the W+Jets background, and this is skewed further by the requirement of the single electron trigger (single high p_T electron) in our OR'ing. For these reasons, we shall proceed with the $t\bar{t}$ background and the W+Jets background will not be discussed.

Since the OR of the e+Jets triggers already contains the original e+Jets trigger that was used in the comparison of the results, it would be interesting to determine whether this OR shows an improvement alone, without the single electron trigger ORs. *caf_trigger* was written in a form which allows for the compartmentalization of the different triggers that were used to create the combined OR'd triggers. This enables us to determine the benefit of the e+Jets OR'd triggers over the original e+Jets triggers without the single electron triggers added in. The individual trigger lists were performed with v12-v14 since there was only a single e+Jets trigger term for v8-v11, and the full set of trigger lists and luminosities were used for the luminosity averaged efficiency (see Table (4.7)). It is interesting to note that an OR of the e+Jets trigger brings at least 2 additional terms to the main e+Jets trigger: a CEM(2, 6) L1 term (defined in Table 4.3), and a CEM(2, 3)CEM(1, 9) L1 term, where additional terms result in a change in the L2 condition (see Tables (4.1) and (4.2)). The luminosity averaged trigger efficiencies, were calculated for the v8-v14 trigger lists: $83.6\pm^{0.6}_{0.5}\%$ for *tb* MC and $82.2\pm^{0.6}_{0.6}\%$ for *tqb* MC for the original e+Jets trigger and $84.1\pm^{0.6}_{0.5}\%$ *tb* MC and $82.7\pm^{0.6}_{0.6}\%$ *tqb* MC for the OR'd e+Jets triggers (statistical uncertainties are $\pm 0.2\%$, as calculated with Equation (4.15) in Chapter 4). The uncertainties were produced through the systematic uncertainty calculations available in *caf_trigger* for the averaged efficiencies of the v8-v14 trigger lists. The probability distribution for all the trigger lists is shown in Figure (5.2), and the efficiencies for the individual trigger list for the *tb* and *tqb* MC are shown in

Table (5.1). A representative example can be seen between the v12 and v14 e+Jets triggers. Both of these triggers add only the two L1 terms listed above and they both show a negligible gain in the overall efficiency of the triggers. The gains in efficiency, omitting the uncertainties for the time being for the *tqb* MC events, are from 81.3% to 81.5% for v12, and from 81.1% to 81.8% for v14 or an overall gain of 0.2% and 0.7% respectively (Figure (5.1)).

The increase in the efficiency is consistent with zero, and is not unexpected as the only changes in the trigger are made at L1 and only to the number and energy of the electrons. The gain in efficiency is less than the systematic uncertainty in the trigger efficiencies which indicates that the OR of the various e+Jets does not contribute to a useful improvement in the efficiency. As before, the statistical uncertainties were calculated to be ±0.2%. As in Chapter 4, the statistical uncertainties will be decreased due to the correlations of the triggers, and the subtraction of the efficiencies used to determine the increase.

As a comparison, the gain of the acceptance of the *tb*-like, and *tqb*-like $t\bar{t}$ backgrounds was calculated. Two $t\bar{t}$ Monte-Carlo samples are used for the *tb* and *tqb* channels: a *tb*-like background $t\bar{t} \rightarrow l + \nu + 2b$ with 283,463 events (MC cross section of 1.27 pb), and a *tqb*-like background $t\bar{t} + q \rightarrow l + \nu + 2b + q$ with 98,425 events (MC cross section of 0.554 pb), which were reduced from the pre-selection cuts to 42,481 and 14,501 events respectively. This was done to see if the e+Jets OR'd triggers accepted more background events than the original e+Jets triggers. The luminosity averaged trigger efficiencies of the backgrounds for the v8-v14 trigger lists are: $90.1 \pm^{0.9}_{14.3}$% *tb*-like and $90.6 \pm^{0.9}_{13.2}$% *tqb*-like for the original e+Jets triggers, and $90.8 \pm^{0.9}_{14.3}$% *tb*-like and $91.3 \pm^{0.9}_{13.2}$% *tqb*-like for the e+Jets OR'd triggers.

The gain in the acceptance of the background events is consistent with zero, which is the same result as was found for the signal events. This means that the use of the e+Jets OR'd triggers does not accrue any negative contribution from the background events. The e+Jets OR'd triggers do not contribute negatively to the study, they show no positive contribution over the original e+Jets triggers. The

Table 5.1: e+Jets ORs vs original e+Jets trigger efficiencies, for the leading electron, of the *tb*-eνbb and *tqb*-eνbqb MC vs trigger list. Trigger lists v8-v11 have been combined since there are no changes to the triggers during that period.

Trigger List	v8-v11	v12	v13.0	v13.3	v14
tb e+Jets ORs	89.9%	83.1%	84.2%	83.5%	83.3%
tb e+Jets original	89.9%	82.8%	83.5%	82.8%	82.6%
tqb e+Jets ORs	89.4%	81.5%	82.6%	81.6%	81.8%
tqb e+Jets original	89.4%	81.3%	82.0%	81.0%	81.1%

e+Jets OR'd triggers should not be used in the future as they do not contribute to the increase in the signal significance while adding appreciable overhead to the calculation.

Our next step will be to calculate the gain in the significance of the single top signal by considering the $t\bar{t}$ background. Although we have calculated an increase in the efficiency for the single top events, there is still a concern that the acceptance for background events will overshadow this gain. A proper detailed calculation of the gain in the signal significance would require a full run of the analysis chain, which had not been completed by the collaboration at this time. We can still make a rough estimate of the gain in the significance by considering a Gaussian uncertainty on the background. We start with the sigma deviation, $\sigma = N_S/\sqrt{N_B}$, where N_S and N_B are the number of signal events and background events respectively. This quantity σ defines roughly the significance of a signal with respect to the background events. From this, we can define a gain g, in the number of events N as gN. For instance, an increase in the number of accepted events of 3% would be a gain of 1.03. With this definition, we define g_σ as the gain in the signal significance σ, g_S as the gain in the signal, and g_B as the gain in the background. We multiply the gains into the equations to obtain the new signal significance as

$$g_\sigma \sigma = \frac{g_S N_S}{\sqrt{g_B N_B}}. \tag{5.1}$$

Since we are only interested in the gain in the significance g_σ in Equation (5.1), we can cancel out the σ, N_S and N_B terms to ensure that the equation is not

dependant on the number of events. The equation for the gain in significance is then given by

$$g_\sigma = \frac{g_S}{\sqrt{g_B}}. \tag{5.2}$$

We will be using Equation (5.2) as an approximation since we will not include in the gain the possibility that the background analysis will not improve to reject the increased background acceptance from the OR'd triggers. This may not be true assumption for adaptive analysis techniques such as boosted decision trees or neural network analyses since better training of the trees or neural network will improve their background rejection. The two $t\bar{t}$ backgrounds used in the comparisons of the e+Jets OR'd triggers with the original e+Jets triggers were used for the significance calculations. The *tb*-like and *tqb*-like background trigger efficiencies were, for the combined v8-v14 trigger lists, 90.1% (*tb*-like) and 90.6% (*tqb*-like) for the original e+Jets triggers, and 93.2% (*tb*-like) and 93.6% (*tqb*-like) for the $E_S \vee EJ$ triggers. This is a gain of 3.1% for the *tb*-like and 3.0% for the *tqb*-like, $t\bar{t}$ events.

The estimated signal significance, for the *tb* and *tqb* channels, is calculated using Equation (5.2) and the increase in efficiencies for the signal events given in Chapter 4 as 6.3% for the *tb* MC, and 7.3%. Our very roughly calculated g_σ is equal to 1.040 (*tb*) and 1.057 (*tqb*) over the $t\bar{t}$ background considered. A more accurate estimate of the signal significance would require the entire analysis chain to be run, which had not been completed by the collaboration at this time. This must be done in order for the adaptive techniques of the boosted decision trees or neural networks used in the analyses to use the events from the increased acceptance of the signal and the background. The estimated overall gain in the signal significance would mean that a significance of 2.89 for *tb* and 2.84 for *tqb* single top events, would actually be a $\sigma = 3.0$ significance with the new triggers.

There are still several things that can be done to improve this study. The following are two issues: the first is with the way the turn-on curves were produced, and the second covers track triggers which could be used to further increase the

efficiency of the triggers.

The trigger turn-on curves produced in *em_cert* were not fitted to an error function which precludes the advantage of the fitted curve smoothing out any statistical fluctuations. This was due to the turn-on curves being an OR of many single turn-on curves which causes an error function fit to incorrectly represent the data points. The true turn-on curve would have several plateaus whereas an error function could only represent one plateau. This problem can be solved by performing an error function fit to the single object, single trigger turn-on curves before the OR of them is taken. This would serve to smooth out statistical fluctuations in the turn-on curves, while still providing an accurate representation of the final OR'd turn-on curves with multiple plateaus. This would not be an easy thing to accomplish, as it would require rewriting the *em_cert* package to build in the error function fits before the trigger OR'ing.

The triggers studied have L3 conditions that require an electron or jet to have a p_T greater than a specified threshold. An additional requirement can be added for a particle track to have a p_T threshold as well. The addition of a track requirement improves the chance that an object identified as an electron will have a matching track. The ability to trigger on tracks was not implemented in *em_cert* at the time of this study and so could not be tested, but is currently being implemented by the developers of *em_cert*.

The trigger OR'ing produced for the single top working group has shown an increase in the efficiency of the triggers. We obtained a very rough estimate of the gain in the significance of the signal. If we consider the case of tb single top events, this would roughly mean that at a cross section of 5 pb, to obtain 5000 events we would normally require 1 fb^{-1} of integrated luminosity. This would be lowered, by our rough estimate, to only requiring 0.96 fb^{-1} of data which may mean that the discovery would come a little earlier. Future single top searches should make use of some form of trigger OR'ing as the benefits are noticeable.

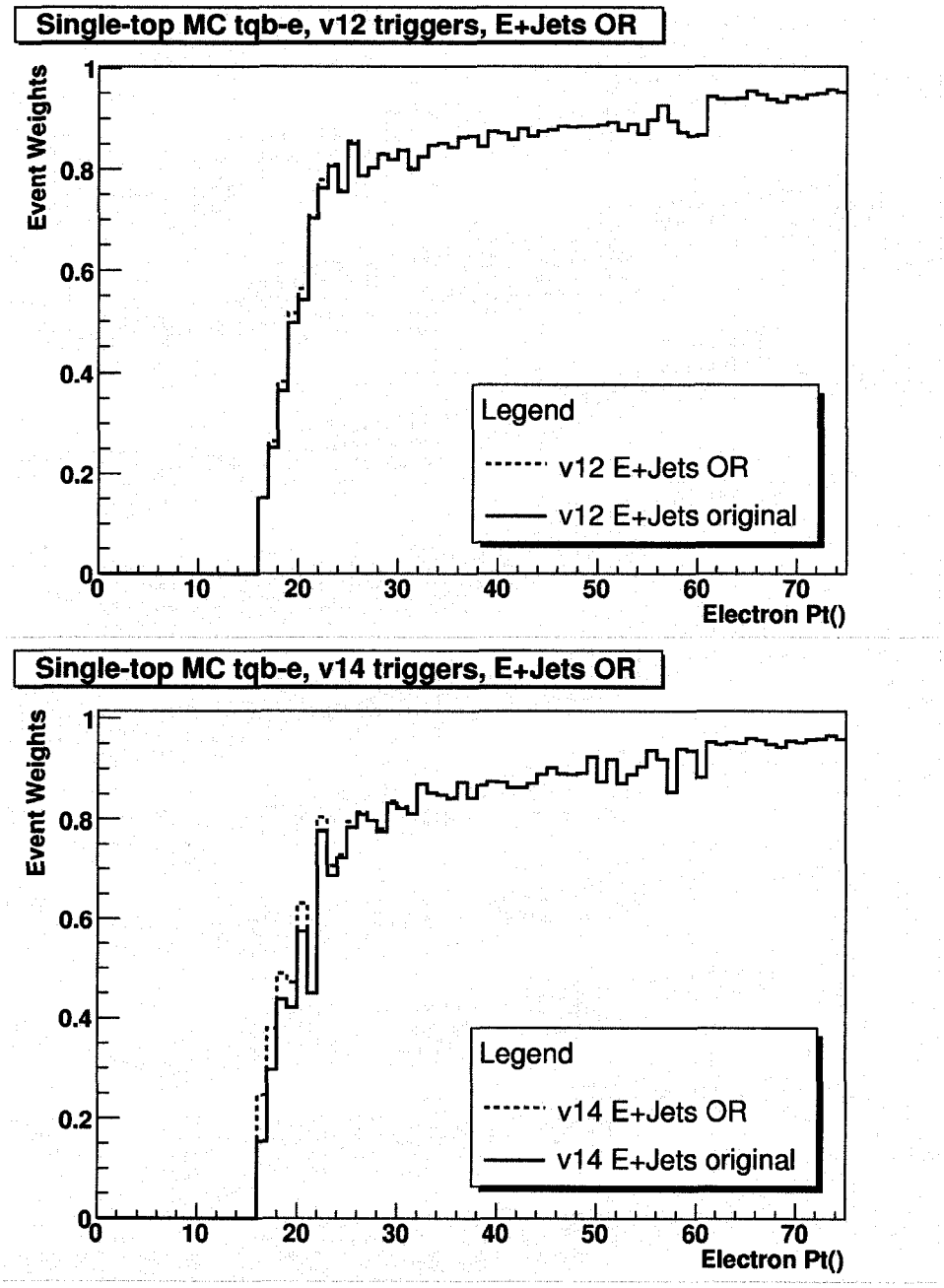

Figure 5.1: e+Jets ORs vs original e+Jets trigger probability distribution in p_T for the leading electron. Top: trigger list v12, tqb-eνbqb MC. Bottom: trigger list v14, tqb-eνbqb MC.

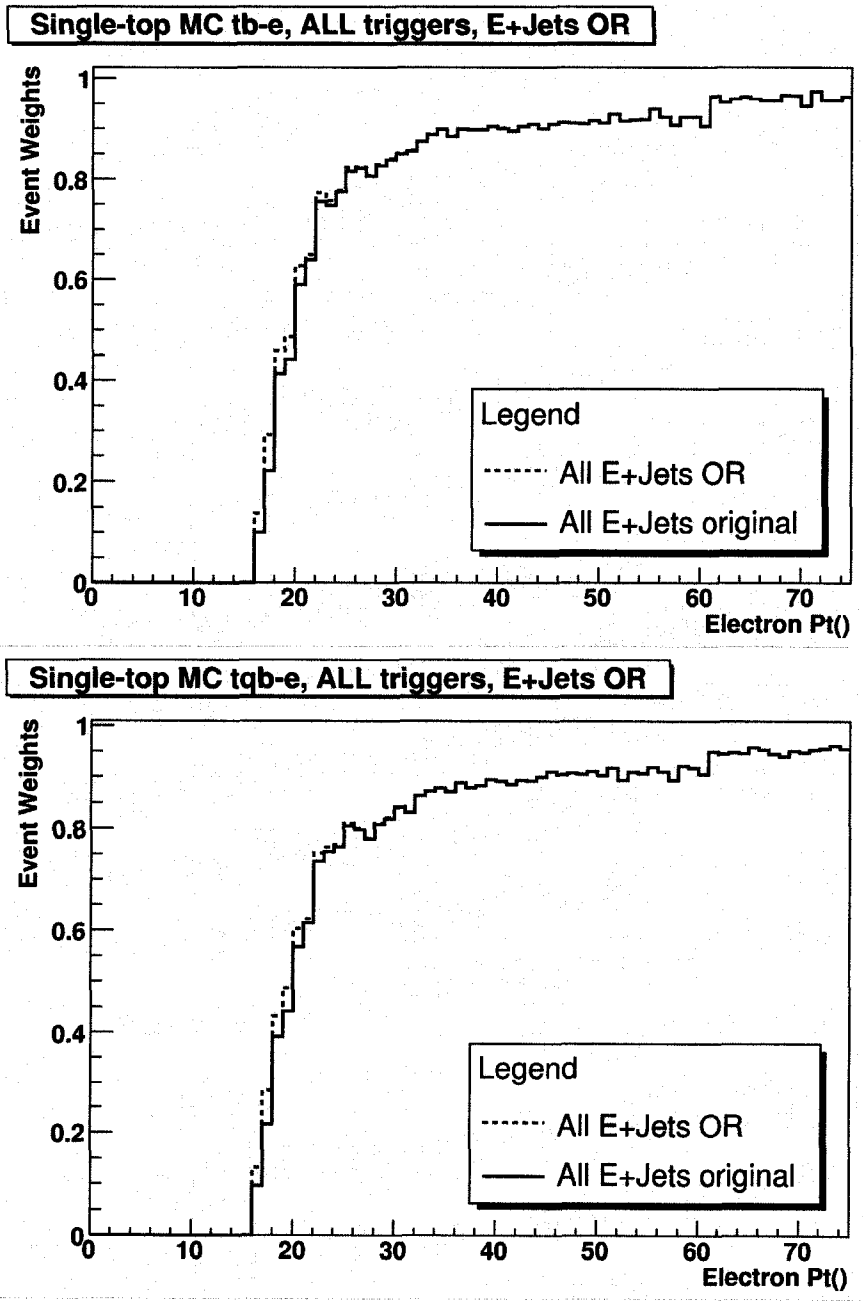

Figure 5.2: e+Jets ORs vs original e+Jets trigger probability distribution in p_T for the leading electron.

Bibliography

[1] T. LeCompte, H. T. Diehl, "The CDF and D0 Upgrades for Run II," *Annual Review of Nuclear and Particle Science*, Vol. 50, p71-177, December 2000.

[2] L. de Broglie, "Ondes et Quanta/Waves and Quanta," *Comptes Rendus, 117, 507, 548, 630 (1923)*, 1984.

[3] M. Gell-Mann, "The Eightfold Way: A Theory of Strong Interaction Symmetry," *California Institute of Technology Report CTSL-20, 1961 unpublished*, reprinted in The Eightfold Way, 1964.

[4] P. W. Higgs, "Broken symmetries, massless particlees and gauge fields," *Physical Letters, Volume 12, Issue 2, p. 132-133*, September 1964.

[5] The SNO Collaboration, "Direct Evidence for Neutrino Flavor Tranformation from Neutral-Current Interactions in the Sudbury Neutrino Observatory," *Phys. Rev. Lett. Volume 89, No. 1, 011302 (2002)* .

[6] P. A. M. Dirac, "A Theory of Electrons and Protons," *Proc. Roy. Soc. A***126,** 360 (1930).

[7] M. Kobayashi, T. Maskawa, "CP-Violation in the Renormalizable Theory of Weak Interaction," *Progr. of Theor. Phys.* **49,** 652 (1973).

[8] CDF Collaboration, "Observation of the Top Quark," *Phys. Rev. Lett.* **74,** 2626 (1995).

[9] D0 Collaboration, "Observation of the Top Quark," *Phys. Rev. Lett.* **74,** 2632 (1995).

[10] Tevatron Electroweak Working Group (for the CDF and D0 Collaborations), "Combination of CDF and DO Results on the Mass of the Top Quark," *hep-ex/0608032, Aug 2006* .

[11] M. Cacciari, S. Frixione, M.L. Mangano, P. Nason, G. Ridolfi, "The t Anti-t Cross Section at 1.8-TeV and 1.96-TeV," *J. High Energy Phys.* **0404**, 068, 2004, hep-ph/0303085, March 2003.

[12] The BABAR Collaboration, "Observation of CP violation in the B^0 meson system," *SLAC-PUB-8904*, hep-ex/0107013, July 2001.

[13] I. Bigi, Y. Dokshitzer, V. Khoze, J. Kühn, and P. Zerwas, "Production and Decay Properties of Ultra-Heavy Quarks," *Phys. Lett. B***181**, 157 (1986).

[14] M. Jezabek, and J. Kühn, "V-A Tests Through Leptons from Polarized Top Quarks," *Phys. Lett. B***329**, 317 (1994).

[15] Francis Halzen, Alan D. Martin, "Quarks & Leptons: An Introductory Course in Modern Particle Physics," *John Wiley & Sons Inc.*, 1984.

[16] Particle Data Group, "Review of Particle Physics," *Journal of Physics G, Nuclear and Particle Physics*, Vol. 33, July 2006.

[17] T. Tait and C.-P. Yuan, "Single Top Quark Production as a Window to Physics Beyond the Standard Model," *Phys. Rev. D* **63,** 014018 (2001), hep-ph/0007298, 17 Oct 2000.

[18] D0 Collaboration, "The Upgraded D0 Detector," *Preprint submitted to Elsevier Preprint* 22, July 2005.

[19] Department of Energy Review Committee, "Report on the Technical, Cost, Schedule and Management Review of the TEVATRON Run II Luminosity Upgrades, February 2004," *Department of Energy.*

[20] D0 Experiment, "D0 Detector Pictures,"
URL: http://www-d0.fnal.gov/Run2Physics/WWW/drawings.htm.

[21] B. Vachon, et. al, "Top Trigger Efficiency Measurements and the top_trigger package," *D0 Note 4512*, July 2004.

[22] Rene Brun, Fons Rademakers, "ROOT - An Object Oriented Data Analysis Framework," *Nucl. Inst. & Meth. in Phys. Res. A 389 (1997)* **81-86**, Sep. 1996.

[23] Z. Sullivan, "Understanding Single-Top-Quark Production and Jets at Hadron Colliders," *Phys. Rev. D* **70,** 114012 (2004), hep-ph/0408049, 25 Oct 2004.

[24] J.Hays, J.Mitrevski, C.Schwanenberger, "The Program Package em_cert: Version p18-br-20," *D0 Note 5070*, March 2006.

[25] Camille Belanger-Champagne, "trigeff_cafe: Single Object Efficiency Calculation in the CAFe Environment," *D0 Note 5093*, May 2006.

[26] Axel Naumann and Frank Filthaut, "Combining Prescaled Triggers," *D0 Note 4844*, June 2005.

[27] Configuration Files, "Skim definitions for 2EMhighPT and TOP-JETTRIG," *http://www-d0.fnal.gov/Run2Physics/cs/skimming/ + skim_p17.07.01/np_tmb_stream/rcp/2EMhighpt_stream.rcp, http://www-d0.fnal.gov/Run2Physics/cs/skimming/ + skim_p17.07.01/np_tmb_stream/rcp/TOP_JET_TRIG_stream.rcp*, June 2005.

[28] Torbjörn Sjöstrand, Stephen Mrenna, and Peter Skands, "The complete PYTHIA 6.400 manual," *JHEP 05, 026 (2006)* LU TP 06-13, FERMILAB-PUB-06-052-CD-T, hep-ph/0603175, March 2006.

[29] R. Brun, *et al.*, "CERN Program Library Writeup W5013," *(1993).*

[30] A. Pukhov *et al.*, "Report INP-MSU 98-41/542," hep-ph/9908288; http://theory.sinp.msu.ru/comphep.

[31] E. Boos, L. Dudko, V. Savrin, and A. Sherstnev, "in preparation; E. Boos, L. Dudko, and V. Savrin," *CMS Note 2000/065.*

[32] D. J. Lange, "The Evtgen Particle Decay Simulation Package," *Nucl. Instrum. Meth. A* **462,** 152 (2001).

[33] "The top_cafe Package," *http://www-d0.fnal.gov/Run2Physics/top/d0_private/wg/top_cafe/doxydoc/html/*

[34] M. Begel *et al.*, "DØ Luminosity in Run 2: Delivered, Triggered and Recorded," *DØ Note 3970, 3971 and 3972.*

Appendix A: *em_cert* turn-on curves

These are the turn-on curves produced in *em_cert* for E_S, E_{EJ}, $E_S \wedge E_{EJ}$, $E_{EJ} \wedge SCJET$, and $E_S \wedge E_{EJ} \wedge SCJET$ for trigger lists v8-v14.

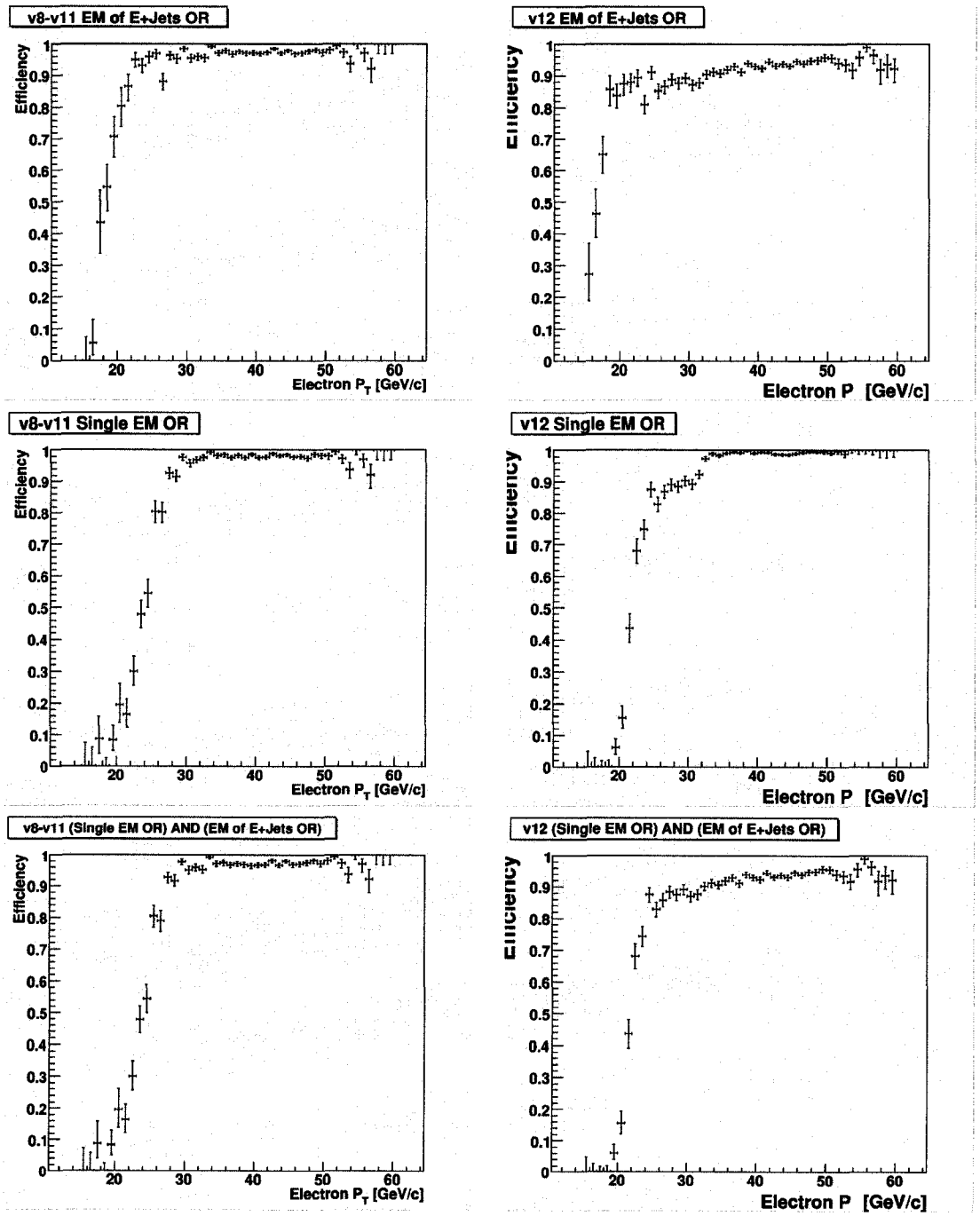

$v8 - v11$ $v12$

Figure 5.3: Turn-on curves for E_S, E_{EJ} and $E_S \wedge E_{EJ}$ for trigger lists v8-v12.

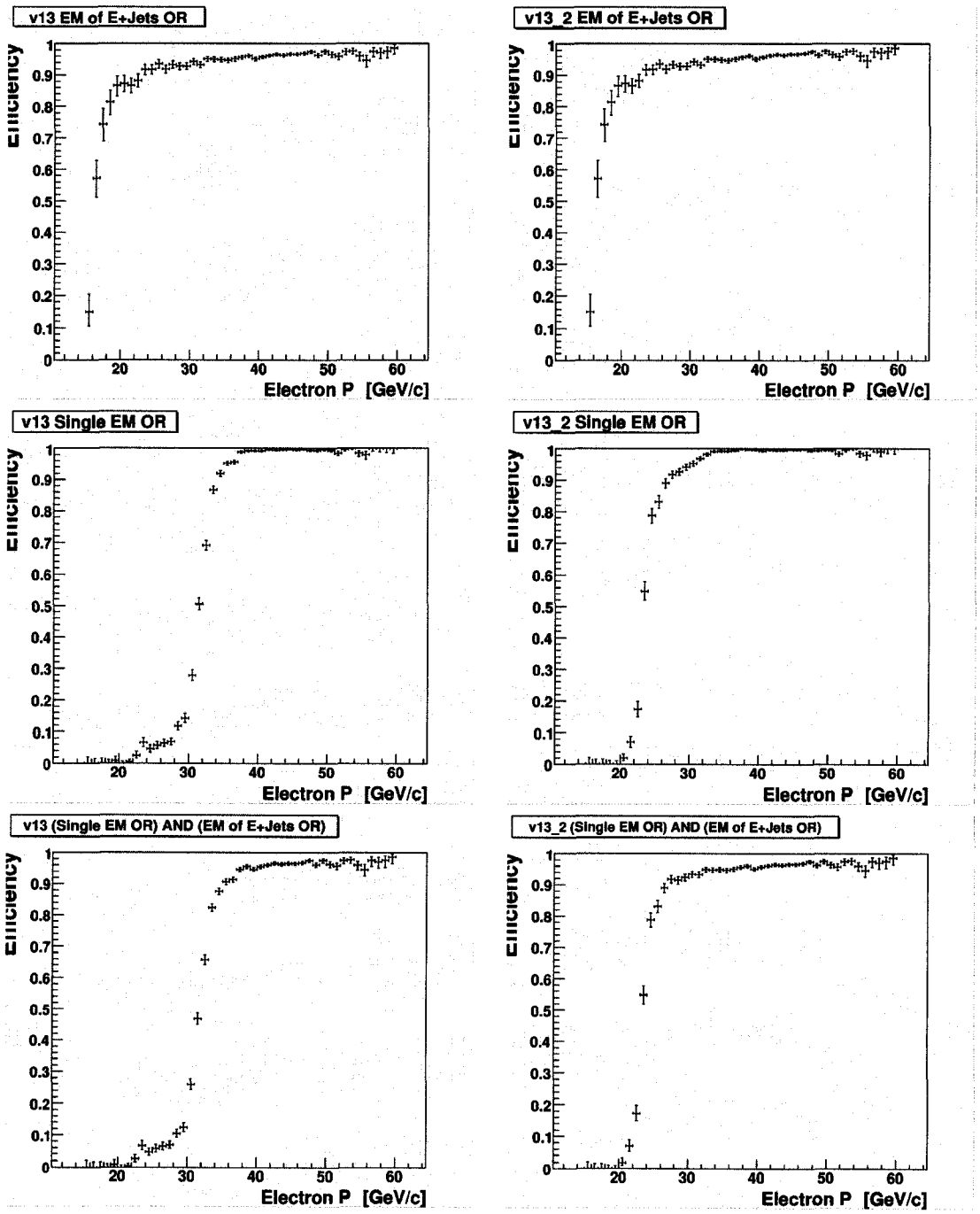

$v13$ $v13.2$

Figure 5.4: Turn-on curves for E_S, E_{EJ} and $E_S \wedge E_{EJ}$ for trigger lists v3-v13.2.

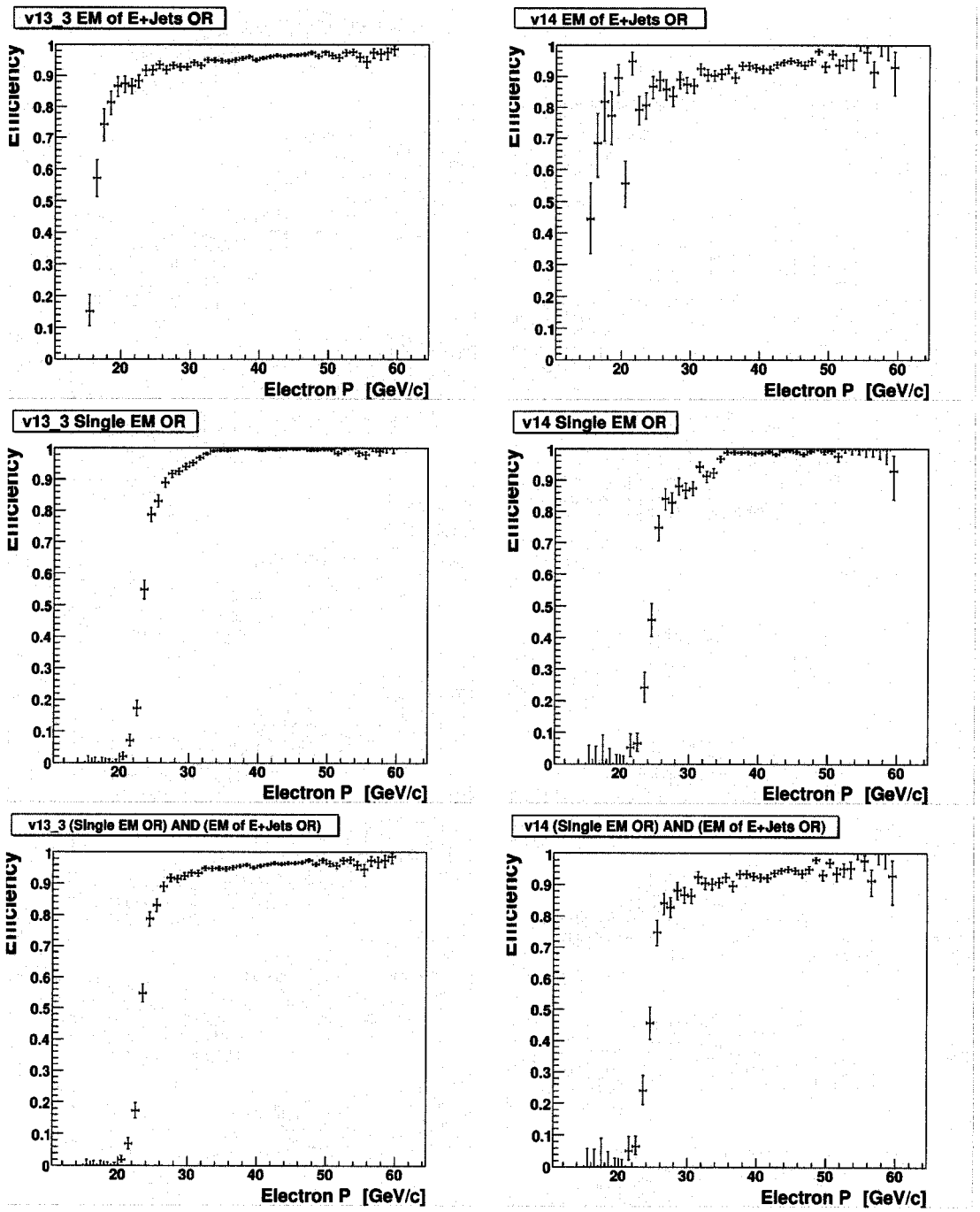

$v13.2$ $v14$

Figure 5.5: Turn-on curves for E_S, E_{EJ} and $E_S \wedge E_{EJ}$ for trigger lists v13.2-v14.

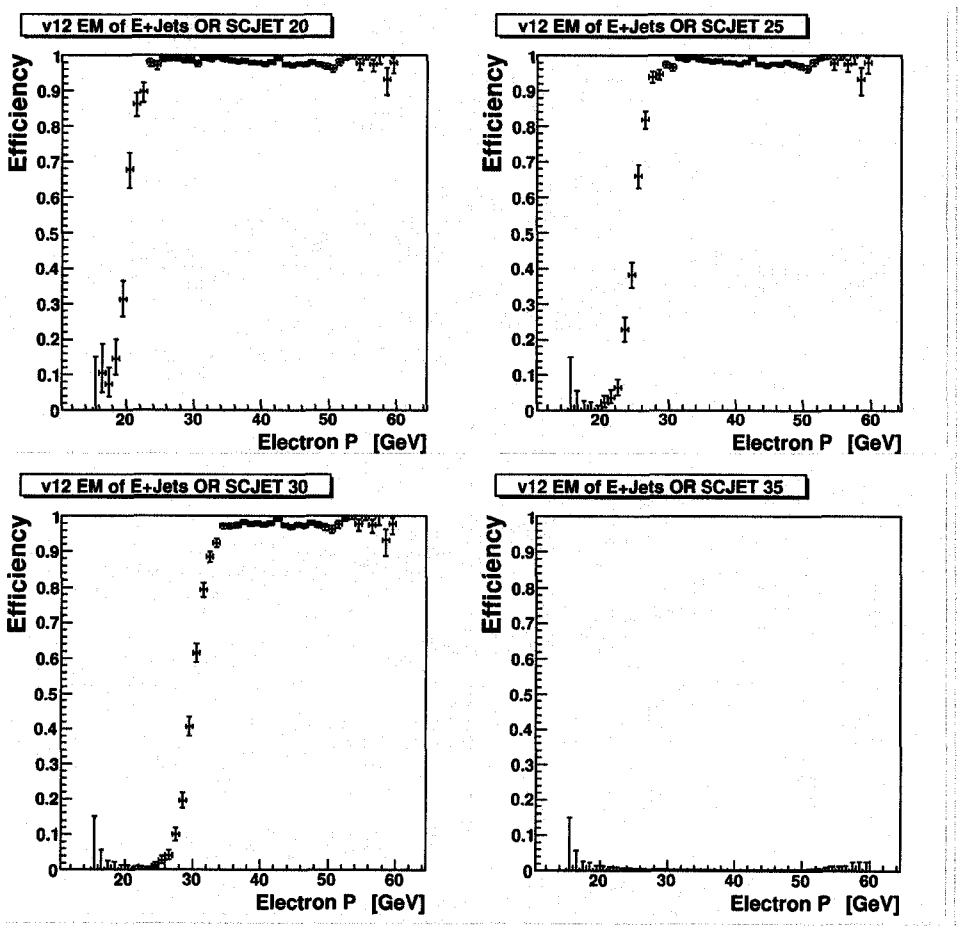

Figure 5.6: The turn-on curve for the v12 electron triggers firing a jet trigger: $Ex\_SHT15 \wedge SCJET(y)$, where x = 1, 2, 3 and y = p_T threshold of 20, 25, 30 and 35 GeV.

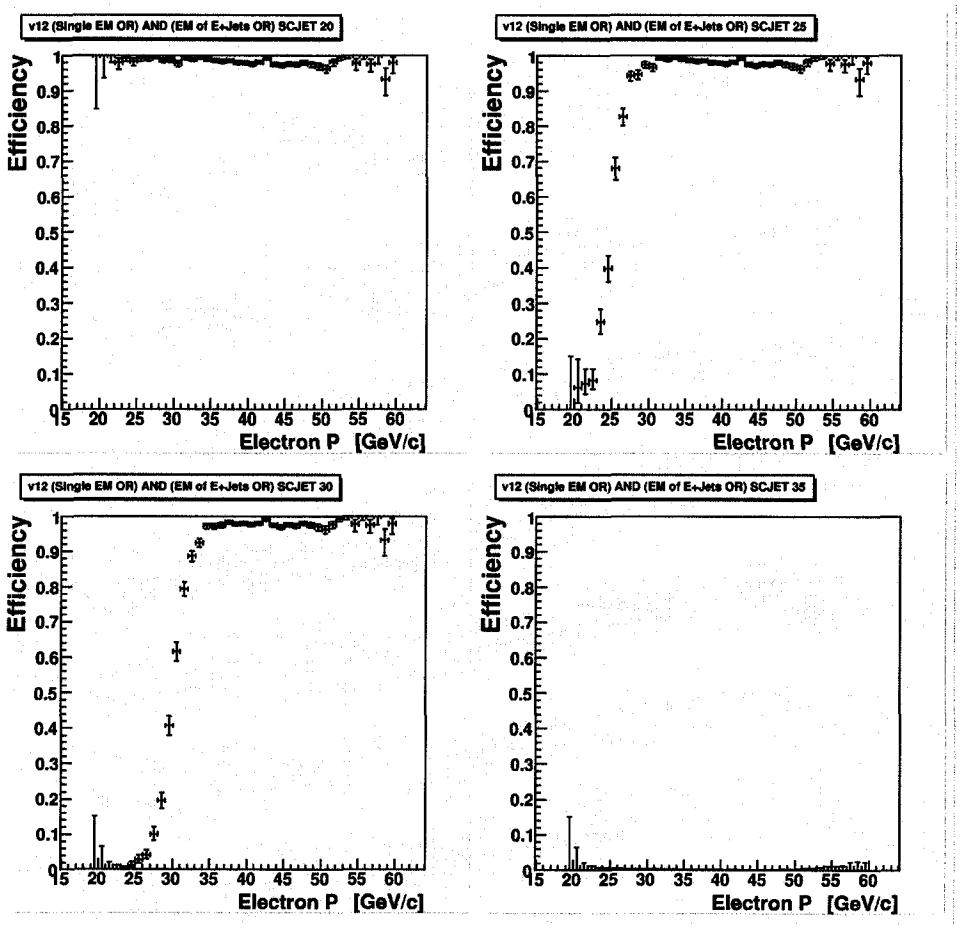

Figure 5.7: The turn-on curve for the v12 electron triggers firing a jet trigger: $(Ex\_SHT20 \vee Ex\_SH30 \vee E1\_L50 \vee E1\_VL70) \wedge Ex\_SHT15 \wedge SCJET(y)$, where x = 1, 2, 3 and y = p_T threshold of 20, 25, 30 and 35 GeV.

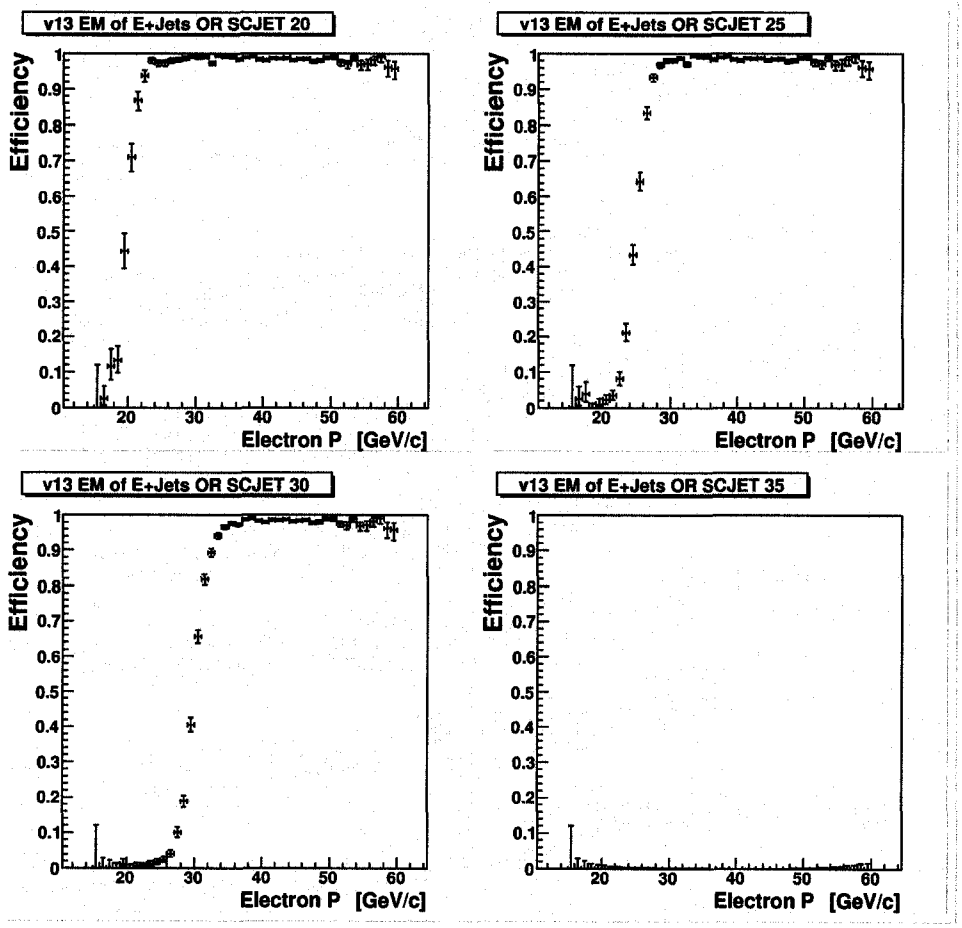

Figure 5.8: The turn-on curve for the v13 electron triggers firing a jet trigger: $Ex\_SHT15 \wedge SCJET(y)$, where x = 1, 2, 3, 4 and y = p_T threshold of 20, 25, 30 and 35 GeV.

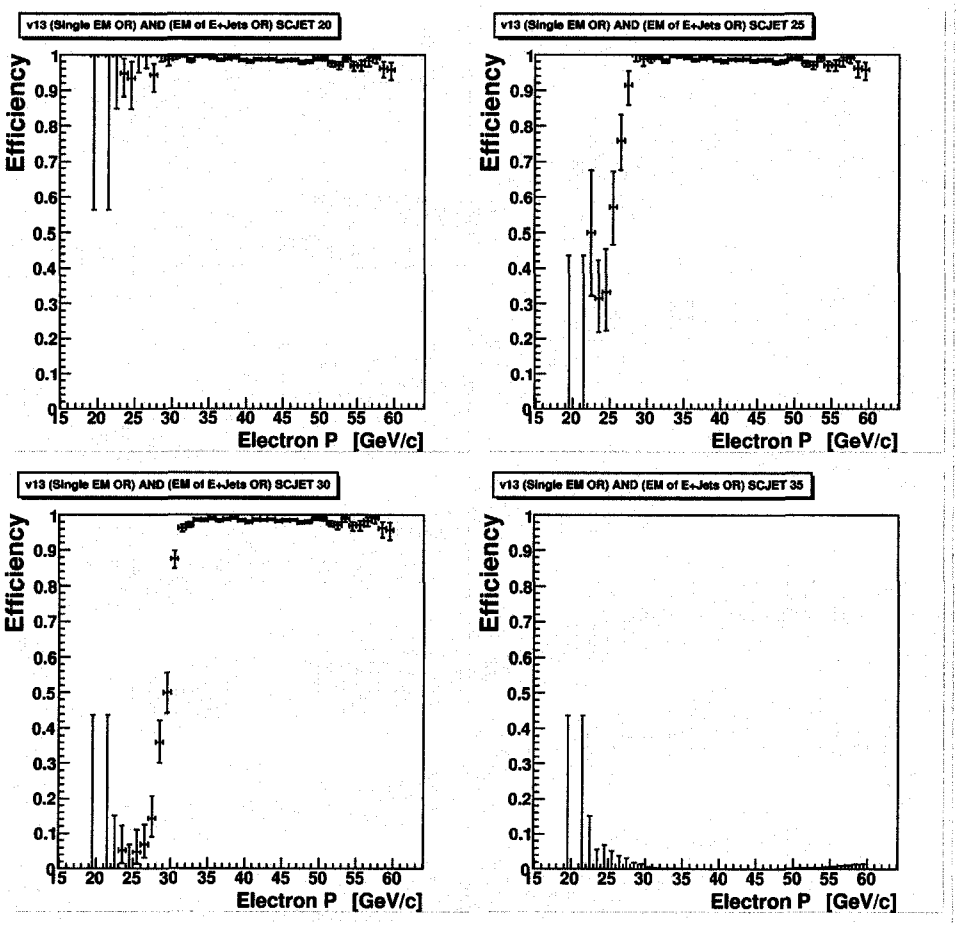

Figure 5.9: The turn-on curve for the v13 electron triggers firing a jet trigger: $(Ex\_SHT20 \vee Ex\_SH30 \vee E1\_L50 \vee E1\_NC90) \wedge Ex\_SHT15 \wedge SCJET(y)$, where x = 1, 2, 3, 4 and y = p_T threshold of 20, 25, 30 and 35 GeV.

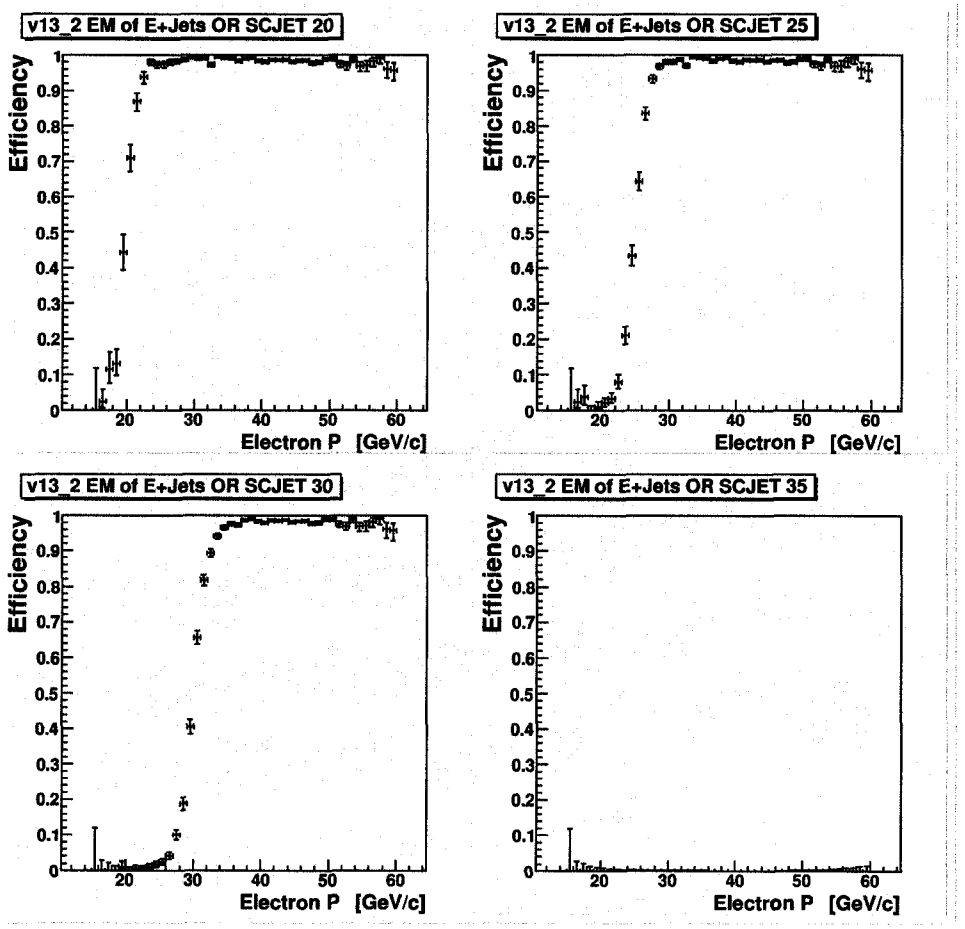

Figure 5.10: The turn-on curve for the v13.2 electron triggers firing a jet trigger: $Ex\_SHT15 \wedge SCJET(y)$, where x = 1, 2, 3, 4 and y = p_T threshold of 20, 25, 30 and 35 GeV.

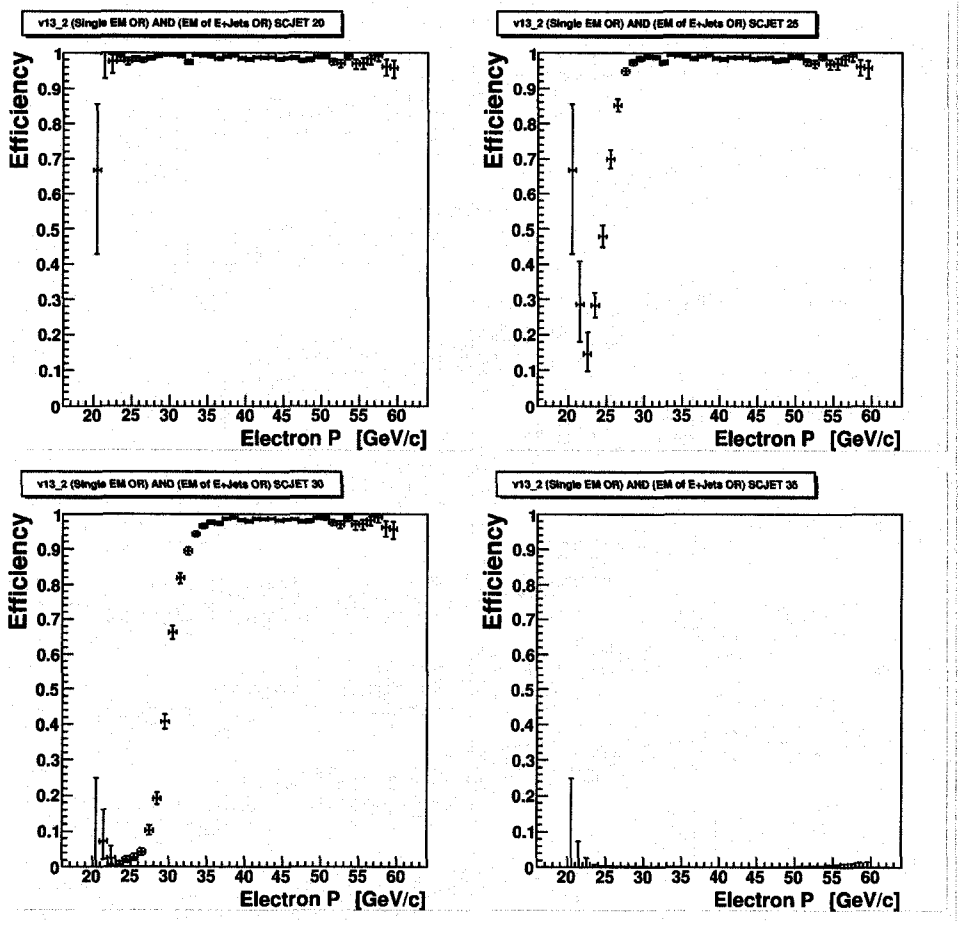

Figure 5.11: The turn-on curve for the v13.2 electron triggers firing a jet trigger: $(Ex\_SHT22 \vee Ex\_SH30 \vee E1\_L70 \vee E1\_NC90) \wedge Ex\_SHT15 \wedge SCJET(y)$, where x = 1, 2, 3, 4 and y = p_T threshold of 20, 25, 30 and 35 GeV.

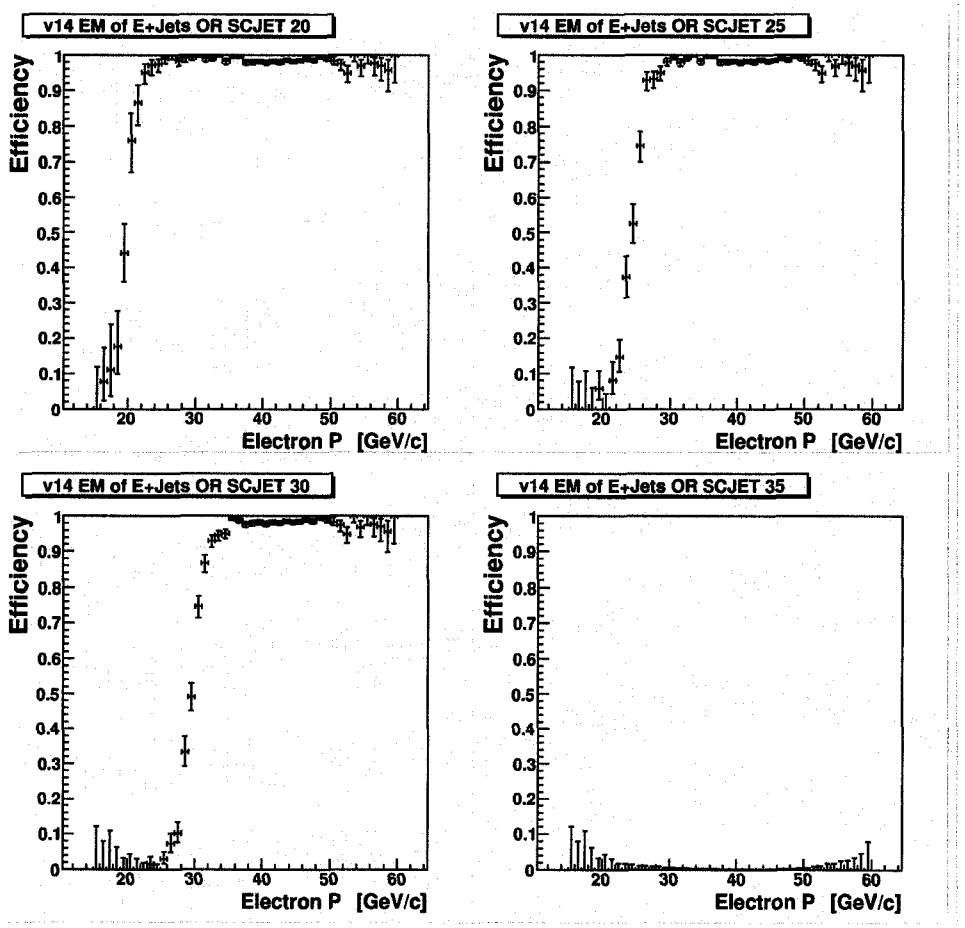

Figure 5.12: The turn-on curve for the v14 electron triggers firing a jet trigger: $Ex\_SHT15 \wedge SCJET(y)$, where x = 1, 3, 4 and y = p_T threshold of 20, 25, 30 and 35 GeV.

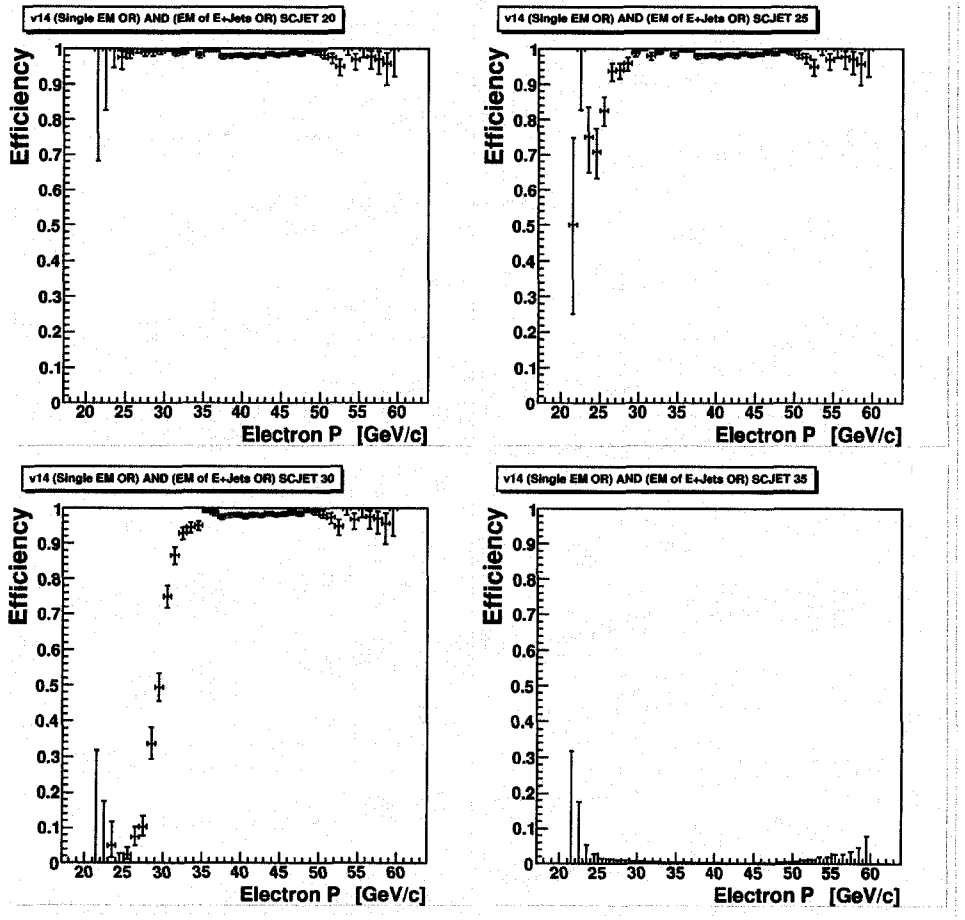

Figure 5.13: The turn-on curve for the v14 electron triggers firing a jet trigger: $(Ex\_SHT25 \vee Ex\_SH35 \vee E1\_L70) \wedge Ex\_SHT15 \wedge SCJET(y)$, where x = 1, 3, 4 and y = p_T threshold of 20, 25, 30 and 35 GeV.

Appendix B: *caf_trigger* trigger efficiency curves

These are the trigger efficiency curves produced in *caf_trigger*, from the turn-on curves produced in *em_cert*, for the original E+Jets triggers in comparison with the $E_S \vee EJ$ triggers for trigger lists v8-v14.

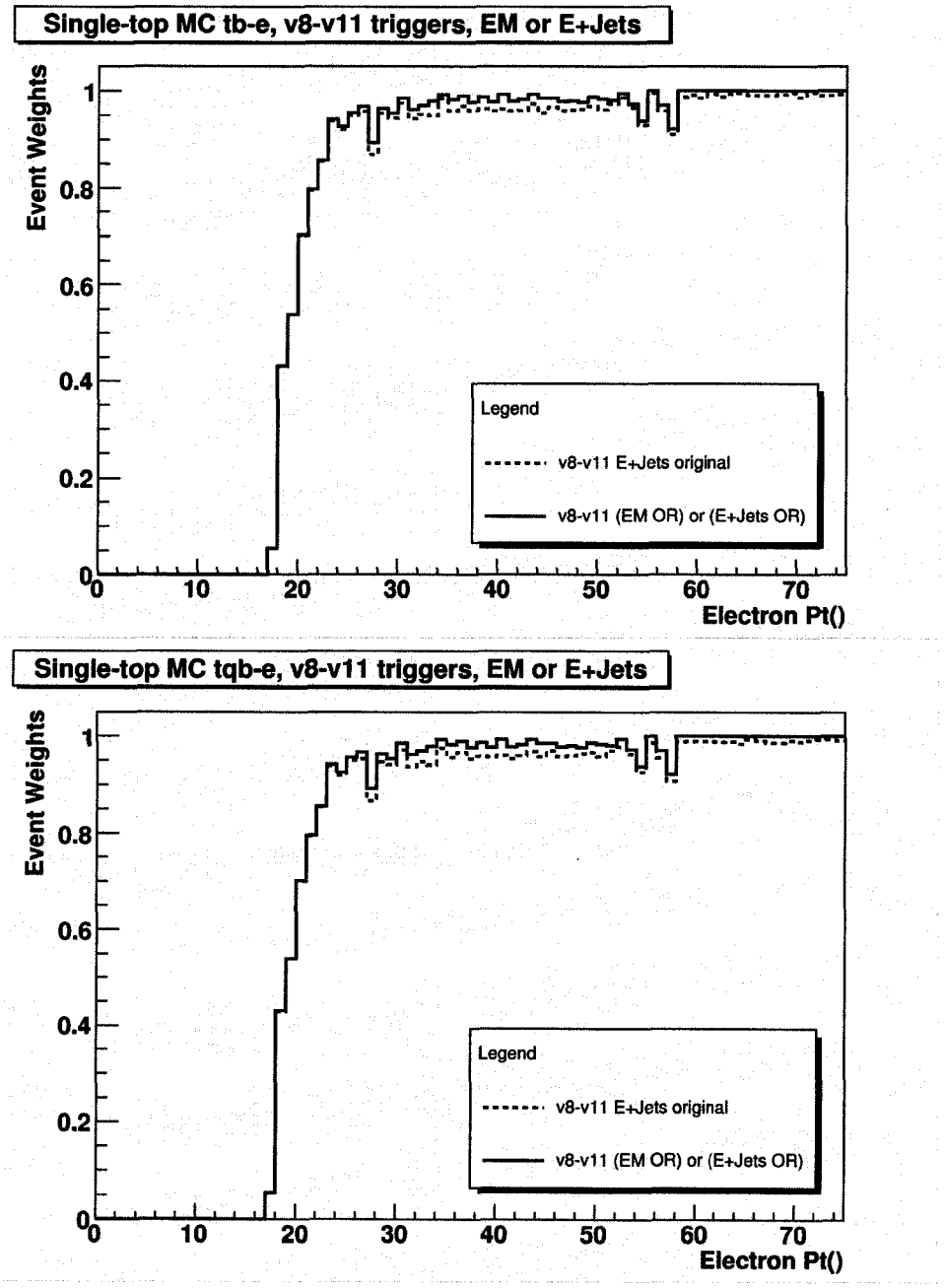

Figure 5.14: Trigger list v8-v11: $E_S \vee EJ$ vs original E+Jets trigger probability distribution in p_T for the leading electron.

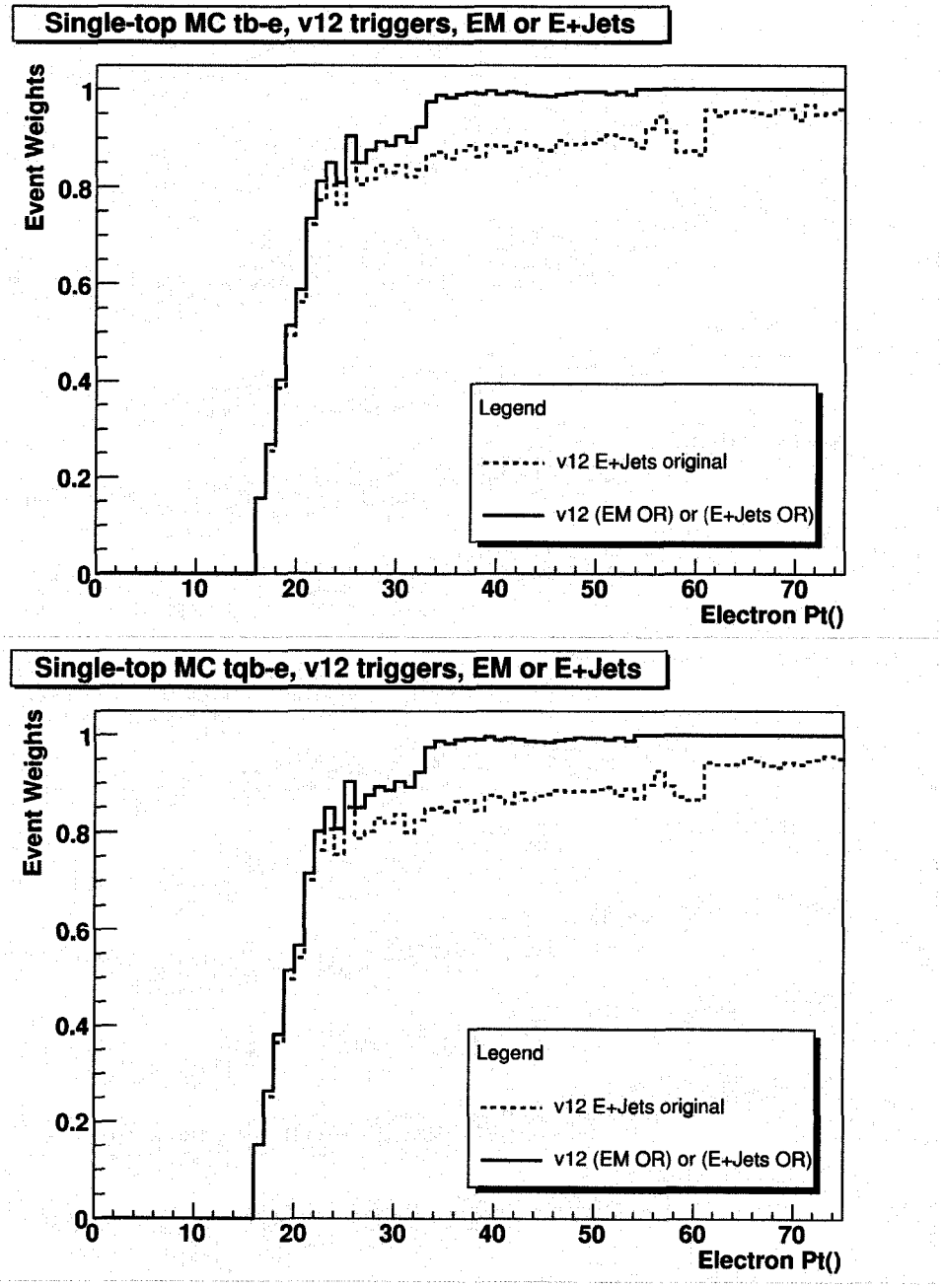

Figure 5.15: Trigger list v12: $E_S \vee EJ$ vs original E+Jets trigger probability distribution in p_T for the leading electron.

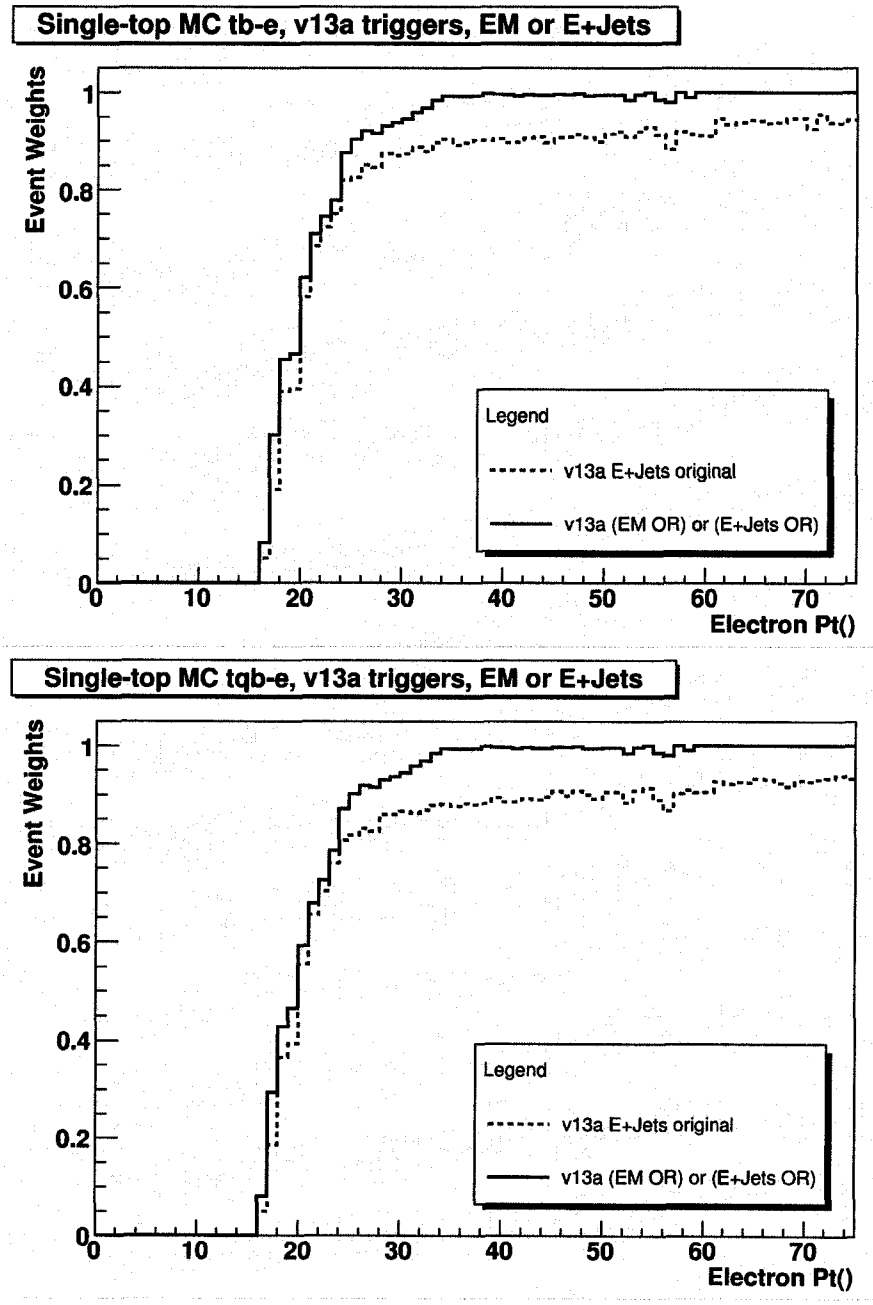

Figure 5.16: Trigger list v13a: $E_S \vee EJ$ vs original E+Jets trigger probability distribution in p_T for the leading electron.

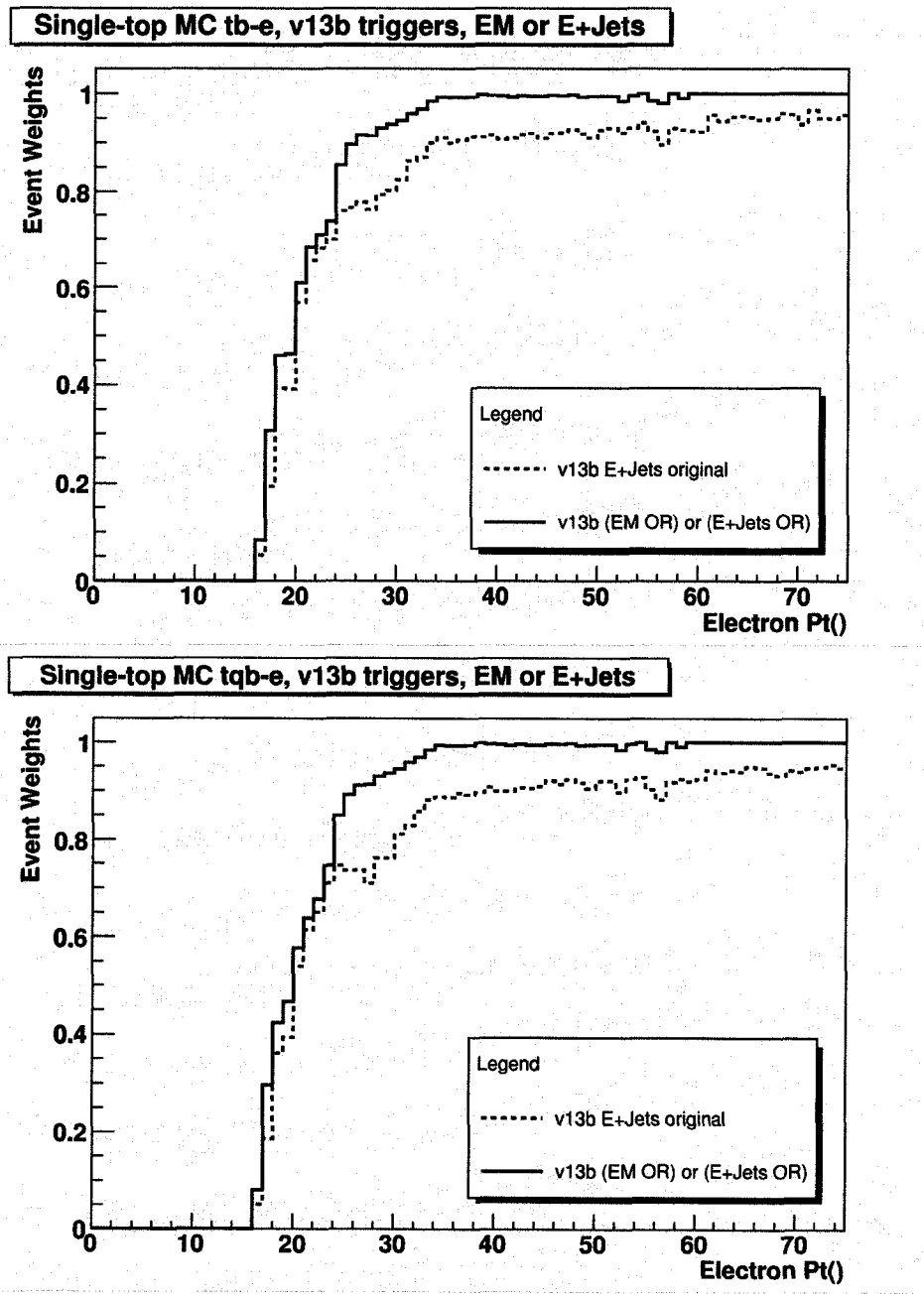

Figure 5.17: Trigger list v13b: $E_S \vee EJ$ vs original E+Jets trigger probability distribution in p_T for the leading electron.

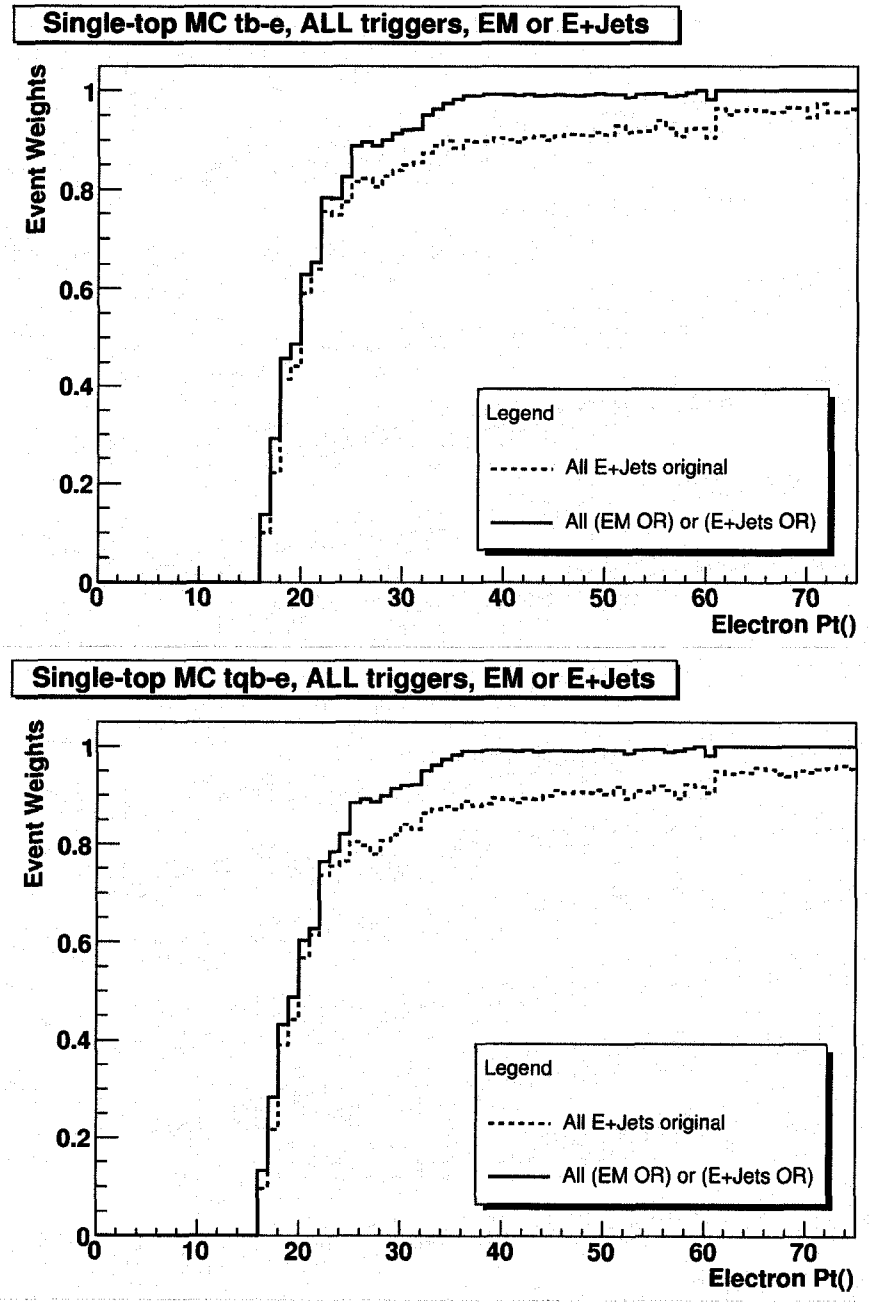

Figure 5.18: Trigger list v14: $E_S \vee EJ$ vs original E+Jets trigger probability distribution in p_T for the leading electron.